INVERSION OF BODY-WAVE SEISMOGRAMS FOR UPPER MANTLE STRUCTURE

Thesis by

JEFFREY WAYNE GIVEN

In Partial Fulfillment of the Requirements

for the Degree of

Doctor of Philosophy

California Institute of Technology

Pasadena, California U.S.A.

1984

(submitted July 12, 1983)

Acknowledgments

My stay at Seismological Laboratory has been a very pleasant experience, and I thank the faculty, students and staff for fostering a stimulating, creative, and, most of all, friendly environment in which to study geophysics. I am especially grateful to Prof. Don Helmberger for his support and encouragement throughout the work leading to this thesis. I have also been fortunate to have worked closely with Prof. Hiroo Kanamori and have learned much from his curiosity and perspective. Both of these gentlemen have given me more freedom to pursue my research than I probably deserved and I appreciate their patience. Special thanks are also due Professors Don Anderson and Dave Harkrider for ideas and guidance throughout my tenure as a graduate student.

The research presented here has been enhanced by my association with several past and present students at the Seismo Lab and I particularly thank Larry Burdick, George Mellman, Terry Wallace, Steve Grand, and Marianne Walck for useful ideas and discussions. Lazlo Lenches expertly prepared many of the figures. Dr. Hsui-Lin Liu critically read the manuscript and assisted with the final preparation when even the tiniest details appeared overwhelming.

This research has been sponsored by the National Science Foundation Grant EAR811-5986 and by the Advanced Research Projects Agency of the Department of Defense under Contract F49620-77-c-0022.

Abstract

We invert observed long- and short-period body-wave seismograms, travel times, and apparent velocity data to further constrain the compressional velocity structure in the upper mantle beneath northwestern Eurasia and the shear-wave velocity structure beneath western North America.

Long- and short-period WWSSN seismograms from nuclear explosions in the Union of Soviet Socialist Republics are incorporated with apparent velocity observations to derive an upper mantle model for northwestern Eurasia. The compressional waves from these explosions have several distinctive features that provide important new information about the character of the upper mantle in the region. The seismograms from 9° to 13° exhibit impulsive first arrivals, P_n, implying a smooth positive velocity gradient between depths of 60 and 150 km. There is a consistent pulse arriving about 2 s after P_n at the distances of 13° to 17°, and at larger ranges there are distinct reflections from two major discontinuities in the mantle. Synthetic seismograms displaying these features indicate a velocity model that correlates with other models from around the world, with a distinctive lid and low-velocity zone. The arrival following P_n is modeled by positioning the low-velocity zone between 150 and 200 km. The model is relatively smooth from a depth of 200 km down to 420 km, where a 5% jump in velocity produces a triplication in the travel time curve from 15° to 23°. The observations from 21° to 26° clearly show another discontinuity at a depth of 675 km with a 4% change in velocity. These results suggest that stable

continental regions may have a shadow zone that extends beyond 17°. Below 250 km there is no distinguishable difference between the model proposed for northwest Eurasia and models derived for the United States.

A systematic inversion technique is proposed to extract the maximum amount of information from these data. We use the WKBJ method to compute approximate synthetic seismograms in a radially heterogeneous earth. Where the WKBJ method breaks down, in low-velocity zones and near discontinuities, a generalized ray expansion is used in a layered model approximation to the velocity structure to isolate the energy that has reflected from these regions. Synthetic seismograms computed using these approximations compare very well to those computed by the more accurate method of summing primary reflections in a generalized ray sum yet require 1/20 the computation time. With this effeciency it is feasible to compute the differential seismograms necessary to pose an inverse problem.

With a fast means of computing synthetic seismograms, an inverse problem can be posed to relate the differences between observed and synthetic seismograms to perturbations in the velocity structure. The problem is nonlinear, especially at high frequencies, but at long periods an iterative technique based on a linearized relation between perturbations in the velocity structure and the seismograms is effective if a reasonable initial model is assumed. Some simple tests of the method indicate that convergence to a satisfactory final model is possible even when starting with a model that predicts substantially different seismograms than those observed.

We invert long-period SH waves recorded on WWSSN seismographs at distances from 15° to 31° in the western United States and East Pacific Rise to

determine the upper mantle shear velocity structure beneath these regions. A high velocity gradient near 400 km produces clear later arrivals from 15° to 17°. We interpret large later phases observed at distances from 23° to 27° as another large velocity gradient at between 600 and 720 km depth. Inversion of these seismograms suggests that the velocity gradient in the upper 200 km of the mantle is small; there is an increase in the velocity gradient around 250 km resulting in a 4% velocity increase by 360 km. The large velocity gradient near 400 km results in a velocity increase of around 8½% between 360 km and 420 km depth. The velocity gradient becomes smaller between 420 and 600 km with a cumulative increase of 5% over these depths. The total increase in velocity from 600 to 750 km is about 14%. Below 750 km the velocity gradient is assumed to be similar to those predicted by global studies of travel times.

There are differences in published travel time data and models that have been derived to fit the SS phases and SS-S differential times observed in this region. The discrepancies amount to about 5 s in the direct S-wave travel time at distances of 15° to 18°. The discrepancy appears to be on the order of 3 s from 19° to 23° and is not resolvable beyond. These disagreements are probably the manifestation of large velocity heterogeneities in the uppermost mantle; either assumption concerning absolute travel times can be fit by models that are virtually identical below 270 km. Absolute travel times can constrain absolute velocities and, thus, are necessary to constrain the depth to discontinuities. Waveform data can constrain the structural details better. A joint waveform and travel time inversion method is a very useful tool for interpreting seismograms for earth structure.

Table of Contents

Introduction

Body waves that have propagated in the upper mantle are wonderfully complex and contain a wealth of information about the physical processes in the earth. The radial elastic structure of the upper 1000 km of the earth produces a bewildering variety of complicated wave propagation phenomena including shadow zones, triplications, and caustics, and understanding these phenomena in terms of that structure is the topic of the following work.

In Chapter 1 we investigate the structure of the upper mantle beneath a stable continental region, northwestern Eurasia, by directly modelling the long- and short-period seismograms. We exploit a unique data set, seismograms of very large nuclear explosions in the U.S.S.R. These observations yield perhaps the clearest picture obtainable of the nature of the lithosphere beneath a stable continental region. We construct a velocity model of the upper 800 km of the mantle that accurately predicts the body-wave sesimograms and that is consistent with previous published studies of travel times and apparent velocity data. Our results strongly support the hypothesis of a thick lithosphere beneath stable continents and suggest the presence of a deep and limited low velocity zone below. We can also confirm the existence of two large increases in the velocity gradient, one at 400 km depth, the other at 670 km.

Our experience with modelling the P-wave seismograms in Chapter 1 was fruitful but frustrating. Trial and error modelling is crucial to understanding important wave propagation phenomena which are observable in seismograms.

However, long after we understand the essential physics behind the observations there remain the tasks of deriving the velocity model that best fits the data and of explaining to our colleagues why it is the best model and what there is about it that makes it so. In other words, how unique is the model that we have derived and how well resolved are its various features.

An extensive and sophisticated generalized inverse formalism has been developed in the geophysical literature that enables us to answer these questions. These techniques have not been widely applied to modeling seismic body waves because of the complexity involved in the computation of synthetic seismograms. Before we can formulate the inverse problem, we need methods to quickly, simply, and accurately model the seismograms. The development of approximations to the equations of elastodynamics is a subject of much current research and new results are forthcoming. Finding life at the leading edge of applied mathematics somewhat uncomfortable, in Chapter 2 we modify and combine some well known and well tested methods of seismogram synthesis. Our techniques are adequately accurate for the problems at hand and are fairly simple.

In Chapter 3 we formulate the inverse problem whereby given some a priori assumptions about the velocity structure, (i.e. an initial guess), we can find a nearby model that best fits the observed data including seismograms, travel times, and apparent velocities ($dT/d\Delta$). The method presented uses only some of the basic concepts of generalized inverse theory; we choose to postpone sophistication until we have more experience with real problems.

With a simple inversion method developed in Chapters 2 amd 3, we investigate the shear velocity structure of the upper mantle beneath part of western

North America and the East Pacific Rise in Chapter 4. Detailed S-wave velocity models are difficult to obtain yet are very important in determining the density structure and composition of the earth. Waveform studies are perhaps the only means of extracting this information from the seismograms. Our results indicate that an inversion method is a very useful tool for interpreting this type of data.

Chapter 1 Upper Mantle Structure of Northwestern Eurasia

1-1 Introduction

There is considerable interest in structure of the upper mantle with respect to the current problems in geodynamics. Although there seems to be broad agreement on the major structural features of the mantle, the various models proposed vary significantly in detail. Important questions yet to be resolved are: (1) how deep are the so-called "400" and "600" km discontinuities; (2) how large are the velocity jumps; (3) how deep in the mantle do velocity variations exist; and (4) how well do these variations correlate with other geophysical observations.

To answer these difficult seismological questions requires more model resolution than generally provided by the classical methods, namely travel time and a sparse set of $(dt/d\Delta)$ measurements (Wiggins, 1969). Some of the ambiguity of earth models determined by classical means can be eliminated by the use of short-period synthetic seismograms. Comparing the relative amplitudes of observed short-period multiple arrivals to synthetics allows a better determination of triplication points as discussed by Helmberger and Wiggins (1971). Several regionalized models for the western North American continent have been obtained using this approach (Wiggins and Helmberger, 1973; Dey-Sarkar and Wiggins, 1976). Unfortunately, short-period observations suffer from

waveform instability in that seismograms from neighboring stations in many situations do not correlate well. On the other hand, long-period body wave studies indicate that waveshapes recorded on the long-period World-Wide Standard Seismograph Network (WWSSN) are remarkably coherent (Burdick and Helmberger, 1978; Helmberger and Burdick, 1979). Thus, current techniques permit development of models that yield synthetics that agree with the observed travel times, the $dT/d\Delta$ measurements, the relative timing and amplitudes of short-period pulses, and the long-period waveshapes. Accurate determination of the upper mantle velocity structure from a variety of regions based on these current techniques would be very useful in quantitatively answering the questions posed above. To this end, a waveform data set compiled from Soviet explosions was used to obtain an upper mantle model for northwestern Eurasia that can be used as a reference model in comparisons with other regions.

Our data set consisted of the seismograms of large Russian nuclear explosions recorded in northwest Eurasia, Iceland and Greenland (Figure 1.1). These WWSSN seismograph stations were in an excellent position to record the complicated P-waveforms caused by the interaction of the simple explosion source and the heterogeneous velocity structure of the upper mantle. In addition, the NORSAR array is favorably located to measure the apparent velocity of the different phases in the P-wavetrain. Several recent investigators (King and Calcagnile, 1976; England et al., 1978) have used these measurements to study the upper mantle. We incorporated their apparent velocity information into our study by adopting KCA, the model proposed by King and Calcagnile (1976) as our starting model. The initial model was modified as required by the waveform data but the $dT/d\Delta$ curve was perturbed as little as possible.

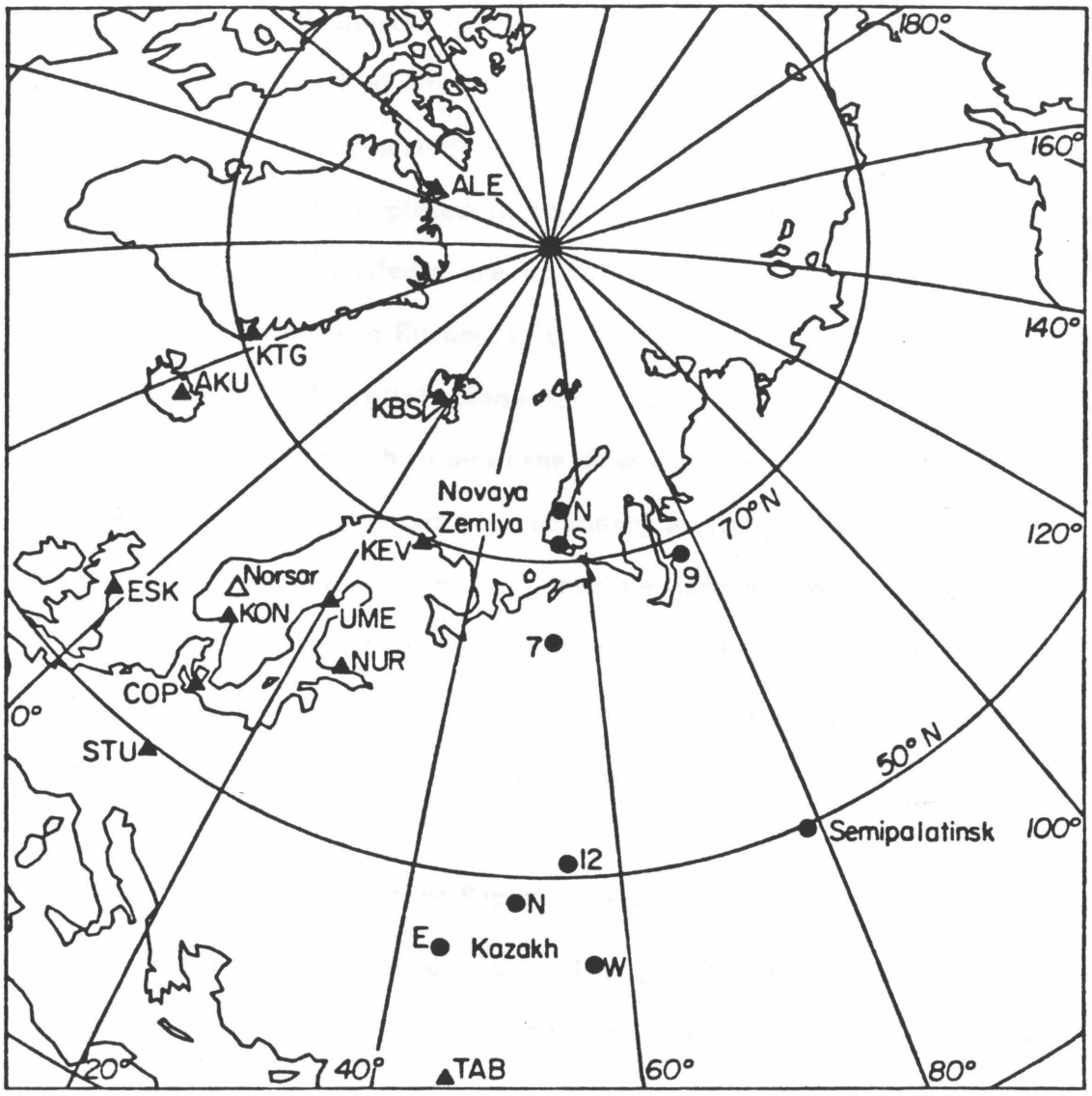

Figure 1.1 Map indicating the locations of source events and WWSSN seismographs used in this study. Information about the event numbers is given in Table 1.1.

The observed waveforms for ranges beyond 17° in NW Eurasia are quite similar to observations obtained at corresponding distances in the United States. However, at shorter distances the two data sets are discordant. The seismograms obtained at 9° from NTS (Nevada Test Site) indicate a severe shadow zone. The short-period amplitudes are very small and many of the long-period waveforms are depleted in short periods (Romney et al., 1972; Helmberger, 1973b). Such effects are not apparent in the seismograms obtained from Soviet explosions in Eurasia (Figure 1.2). Note the sharp P and S phases with little sign of differential attenuation. This feature is most easily explained by restricting the ray path to be in the lithosphere with no appreciable attenuation. At larger ranges one can see secondary arrivals that appear to be coming from below a low velocity zone and thus we have an excellent opportunity to determine the size and depth of this much debated portion of the earth. With this better resolved structure we can make a more accurate estimate of the absolute depths of the major discontinuities.

1-2 Synthetic Seismograms for Explosive Sources

The computational procedure used in generating synthetics is well established, namely one assumes that a synthetic can be represented by a series of linear operators:

$$y(t) = s(t)*m(t)*a(t)*r(t)*i(t)$$

s(t) represents the source; m(t) is the mantle response; a(t) is an attenuation operator; r(t) is the receiver structure; i(t) is the instrument; and * denotes convolution.

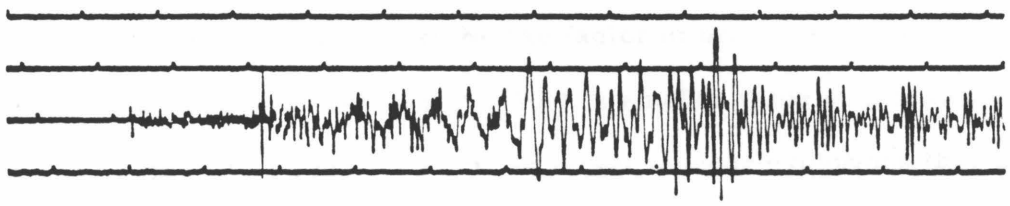

Figure 1.2 Long-period, vertical component seismogram, KEV from Novaya Zemlya (8/28/72) recorded at Δ=9.4°. The S-phase is much larger than the P-phase and has virtually the same frequency content.

We calculate the source time function by the procedure discussed in Burdick and Helmberger (1979). The time function parametrization is taken from von Seggern and Blandford (1972). The far-field time function is written

$$s(t) = \Psi_o \frac{d}{dt}\left\{1-e^{-kt}(1+kt-B(kt))^2\right\}H(t)*C(t)$$

where Ψ_o is an amplitude factor, C(t) is an operator representing the effects of the free surface, and B and k are adjustable parameters controling the shape of the time function.

The parameter B controls the tradeoff between an impulsive and step-like time function of the potential defined by the factor in brackets. A larger value of B means that the source is more step-like, a smaller value of B indicates a more impulsive near field time function. In larger nuclear explosions that produce the best long-period seismograms we found that B=6 was an appropriate value to adequately reproduce the teleseismic observatons. For smaller explosions and short-period seismograms a value of B=2 was found to be suitable. The parameter k is used to adjust pulse width and rise time. Larger explosions are modeled by assuming k=3, small explosions are modeled by taking k=5. A comparison of observed and calculated teleseismic seismograms of nuclear explosions can be found in Burdick and Helmberger (1979).

The parameters B and k trade off with the operator $C(t)$ that models the effects of the free surface. A shallow source depth causes the negative reflection from the free surface to filter out the low frequencies in the time function mimicking the effect of both B and k. As we calculate synthetics for different ranges, the take-off angle of P and pP changes. As a result the pP-P

delay and the free surface reflection coefficient vary with the distance to the receiver. We have found that the change in take-off angle has a small effect on the waveforms, not significant in view of the other uncertainties in the source operator. Using the results of Burdick and Helmberger (1979) as our guide, we took pP-P delay times of 0.9 sec for large events and 0.6 sec for small events. The reflection coefficient at the free surface was taken to be -0.8, independent of range.

The operator C(t) also includes the crustal response at the source. We could find no evidence in the long-period P-waves for any large distortion due to crustal structure so the source region was modeled as a half-space. In short-period seismograms source structure is probably important and distorts the signal in ways that are difficult to interpret. We concentrated on modeling accurately the long-period waveform data while trying to fit only the general features of the short period observations.

At ranges where the arrivals from the upper mantle are separated in time, the uncertainties due to the source function are generally unimportant. However, at ranges where the arrivals from the upper mantle interfere, the errors in the source function can strongly affect the synthetics. Of particular difficulty are secondary P-wave arrivals that interfere with the second upswing of the first arrival. We tested different sources to check the validity of our conclusions in these situations.

The effect of anelasticity was approximated by a Futterman attenuation operator (Futterman, 1962; Carpenter, 1966) with $T/Q=1$ for all ranges. Kennett (1975) has pointed out the errors introduced by this approximation when low Q zones are present in the upper mantle. The assumption was reevaluated by

Burdick and Helmberger (1978) and they concluded that the relative amplitudes (waveforms) were not affected significantly for the structures they were modeling. These authors point out the naivete of attempting to model the velocity and attenuation structure separately. However attenuation, although easily modeled, has been very difficult to observationally determine.

It will be obvious that the character of the upper 200 km of the mantle in northwest Eurasia is very different from the western U.S. as investigated by Burdick and Helmberger (1978). The ray paths we were trying to model are from both above and below a low velocity zone, possibly a region of very low Q. We would expect attenuation to have its most pronounced effect in these situations. Unfortunately, with a sparse data set we could not simultaneously invert for structure and Q. We therefore followed Burdick and Helmberger (1978) and assumed Q increases with depth so that $T/Q=1$ for all ranges. As our knowledge of the attenuation structure of the earth increases, our results may have to be modified to incorporate better constraints on anelasticity.

The receiver operator models the effect of locating the receiver on the free surface and the effect of crustal structure beneath the receiver. The reverberations and converted phases in the receiver crust are often small enough to be ignored on the long-period seismograms (Burdick and Langston, 1977). However, crustal structure is probably the most important factor contributing to the inconsistency observed in short-period body waves as can be surmised by examining the horizontal components of motion of complicated P-waveforms. The long-period seismograms used in this study were of generally good quality. A study of particle motion indicated that in almost all cases the seismograms were uncontaminated by SV energy.

The other operators have been fixed so that we may investigate the operator m(t), the upper mantle response. The earth was assumed to be laterally homogeneous and the radial velocity structure was approximated by layers of constant velocity. An earth flattening transformation is used to approximate the spherical earth by a plane layered medium. The Green's functions were calculated by summing a finite number of generalized rays; the individual ray reponse was computed using a Cagniard-de Hoop algorithm (Helmberger, 1973a). To minimize computations the ray sum was truncated after including all of the primaries arriving in a given time period. In ranges where diffraction is important in shadow zones and off the ends of triplications, multiple reflections were added to ensure the convergence of the ray sum. The accuracy and limitation of this technique is discussed by Burdick and Orcutt (1979).

In this investigation the phase PP was given some consideration. An anomalous later phase can be identified at several stations 12 to 15 sec after the first arrival that we tentatively identified as PP. Preliminary synthetic models of PP indicated that this phase could be large depending on the internal reflections at the surface near the halfway point. However, the inconsistency of observed PP from station to station makes this phase difficult to use as a model discriminant.

1-3 The Data Set

The source-reciver geometry is illustrated in the map in Figure 1.1. The numbers refer to sources tabulated in Table 1.1. Most of the long-period sources were nuclear explosions in Novaya Zemlya. The propagation paths to Spitsbergen, Fennoscandia and northern Europe are beneath the continental shelf and

Table 1.1 Nuclear Explosions

Event No.	Date	Hr	Min	Lat E	Lon N	Location (*)
1	08/28/72	5	59.57	73.70	55.1	Noz N
2	09/27/71	5	59.55	73.74	55.1	Noz N
3	11/02/74	4	59.57	70.80	53.91	Noz S
4	10/27/73	6	59.57	70.80	54.20	Noz S
5	09/12/73	6	59.54	73.30	55.20	Noz N
6	10/27/66	5	58.00	73.38	54.62	Noz S
7	07/10/71	17	00.00	64.2	54.77	Noz S
8	11/08/68	10	02.05	73.40	54.90	Noz N
9	08/14/74	14	59.58	68.91	75.90	Noz N
10	09/26/69	6	59.56	45.89	42.47	Kaz E
11	08/20/72	2	59.58	49.46	48.18	Kaz N
12	10/22/71	6	02.57	51.51	54.54	Noz N
13	09/27/73	6	59.58	70.76	53.87	Noz S
14	07/01/68	4	02.02	47.92	47.95	Kaz N
15	10/03/72	8	59.58	46.85	45.01	Kaz E
16	12/22/71	6	39.56	47.87	48.22	Kaz N
17	12/06/69	7	02.59	43.83	54.78	Kaz W
18	12/12/71	7	00.57	43.85	54.77	Kaz W
19	12/23/70	7	00.57	43.83	54.85	Kaz W
20	02/13/66	4	51.58	49.82	78.13	Sem
21	07/23/73	1	22.58	49.99	78.85	Sem
22	12/18/66	4	57.58	49.93	77.73	Sem
23	02/26/67	3	57.58	49.78	78.12	Sem

(*) see Figure 1.1
Noz-Novaya Zemlya
Kaz-Kazakh
Sem-Semipalatinsk

the Baltic shield. These travel paths may be characterized as being beneath a stable continental region. The short-period seismograms also included explosions in East and West Kazakh a observed in Europe and Fennoscandia. These P-waves have propagated beneath the Russian platform, again an apparently stable continental region. We will also include in our data set seismograms of explosions in Novaya Zemlya recorded at AKU (Iceland) and KTG (Greenland). In each of these cases, up to one third of the P-wave travel path was beneath a region of the North Atlantic Ocean. These seismograms, which include ranges beyond 23.5 degrees, appeared to be consistent with the other waveform data.

In the distance ranges from 9 to 18° we restricted the data set to sources in Novaya Zemlya and other smaller explosions in that vicinity. The short period observations start at 14.5°, the long-period data begin closer at 9°. Ideally, we would like to correlate the phases observed in the long period records with arrivals on the short-period data. Unfortunately, the gain settings of the WWSSN instruments were such that we were unable to obtain simultaneous recordings of long- and short-period seismograms for any one event. However, Novaya Zemlya was the site of numerous large and small nuclear explosions. Thus we were able to confirm our observations of the important features of the data.

For distances greater than 20 degrees we incorporated all available data from Novaya Zemlya and Kazakh. We also included data from events at the Semipalansk test site as recorded in Tabriz, Iran. Due to this fortuitous instrument setting near 26° we were able to obtain short- and long-period responses for the same explosions. The waveforms appear to be of excellent quality and are reproduced for many events. A careful examination of the short-period responses of this particular station indicates that it is relatively transparent as

judged from azimuthal and horizontal motion test (Helmberger and Wiggins, 1971). For this reason we have spent much effort in modeling these short- and long-period observations as closely as possible.

The NORSAR array is situated within 30° of three distinct regions of seismic activity. There have been several studies using apparent velocity measurements made at NORSAR to determine upper mantle structure from these different azimuths: King and Calcagnile (1976) studied western Russia; England, Worthington and King (1977) studied Europe; and England, Kennett and Worthington (1978) investigated the North Atlantic and Arctic oceans. The England et al. study (1978) summarized the differences in the models resulting from these studies. The European model appears to be the most different, the Western Russian model (KCA) and the North Atlantic-Arctic Ocean model (NAT) seem to be substantially the same below 300 km. Based on regional considerations, our data set is most compatible with KCA at ranges less than 23° and with both KCA and NAT at ranges greater than 23°. Therefore we adopted the $(dt/d\Delta)$ predictions of KCA as the apparent velocity constraints in our inversion.

The travel time data was from the ISC bulletin and included the large nuclear explosions at Novaya Zemlya from 1966 through 1974. Neither the origin time nor the location of these events was known a priori so the uncertainties in travel times is larger than in similar studies in the United States (e.g., Burdick and Helmberger, 1978; Wiggins and Helmberger, 1973). Travel times are of little aid in constraining the fine structure of the upper mantle because of a large amount of scatter due to heterogeneities in the crust and lithosphere. However travel times provide valuable integral constraints on the upper mantle structure.

1-4 Detailed Model Determination

We will begin this section by presenting our results, namely model K8, followed by a comparison of $(dt/d\Delta)$ measurements and travel times with the model predictions. Next, we will give a detailed comparison of the waveform data with synthetics generated from K8. The starting model KCA and model K8 are shown in Figure 1.3. There are two important differences between the models. One is the low velocity zone at 150 km depth in K8. The other is the steep positive velocity gradient between 300 and 400 km in K8 where KCA has a very small gradient.

The $dT/d\Delta$ and the travel time curves for the two models are given in Figures 1.4 and 1.5 ,respectively. The major differences between the models show up markedly in these figures. In Figure 1.4, K8 and KCA are very similar for $dT/d\Delta$ of less than about 12 sec/deg. It is the presence of the low velocity zone that causes much of the deviation of K8 from the KCA curve at larger values of p. Although not observable as an offset in the travel time curve, a shadow zone is evident from the waveform data as will be discussed later. The shadow zone produces diffracted arrivals out to at least 17.5 degrees and possibly to 20 degrees. It is possible that we interpreted a different phase than King and Calcagnile as having traveled above the 420-km discontinuity, which would explain some of the disparity between the two models.

The other obvious difference between the K8 and KCA is the 12 sec/deg branch that extends to about 31 degrees. This branch is from rays that bottom above and at the 420-km discontinuity and is prolonged by the low velocity gradient between 300 and 420 km. The phase corresponding to this branch is a very distinctive feature of the King and Calcagnile (1976) data. Some of our short-

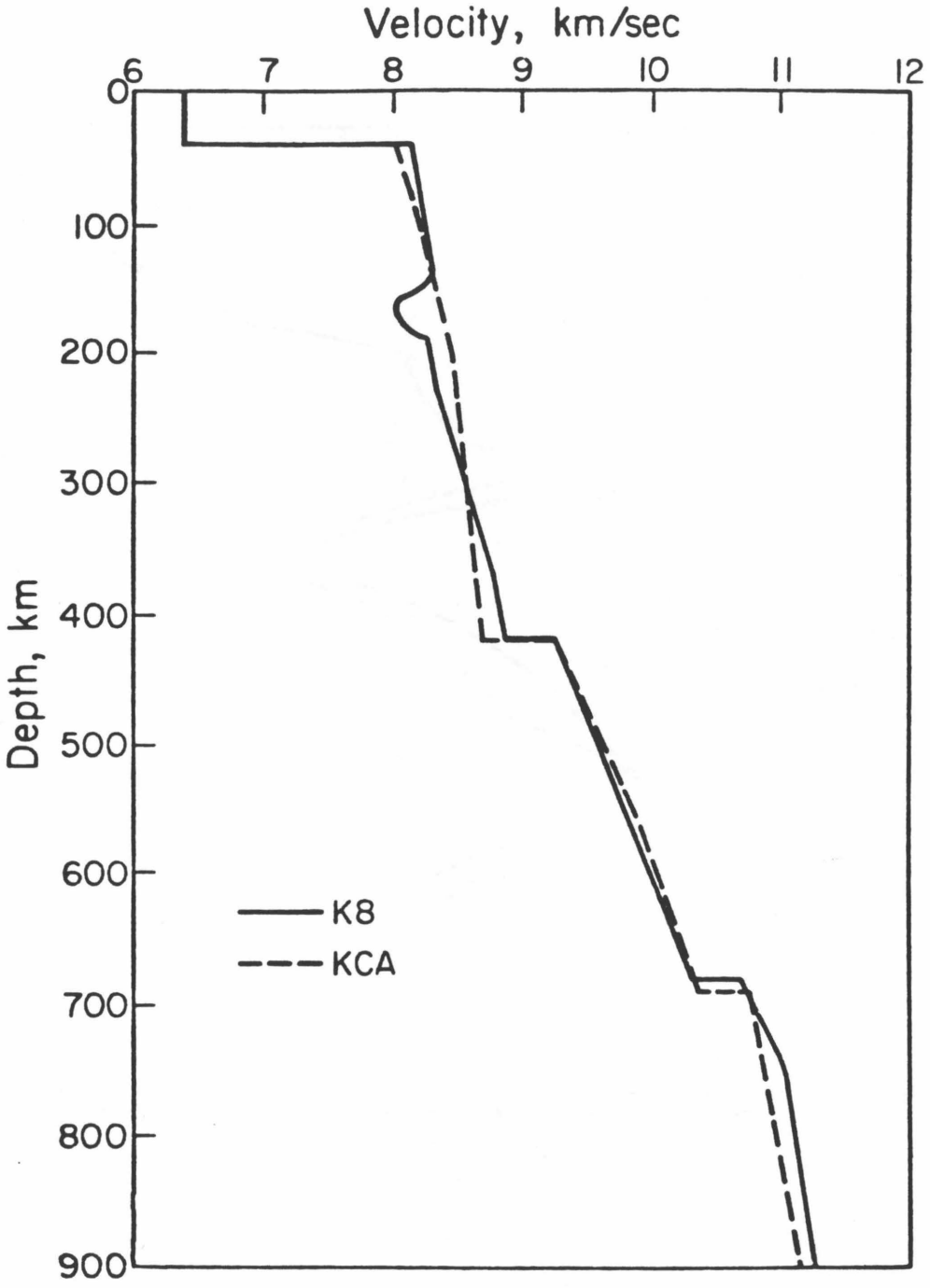

Figure 1.3 Model KCA (King and Calcagnile, 1976) and K8.

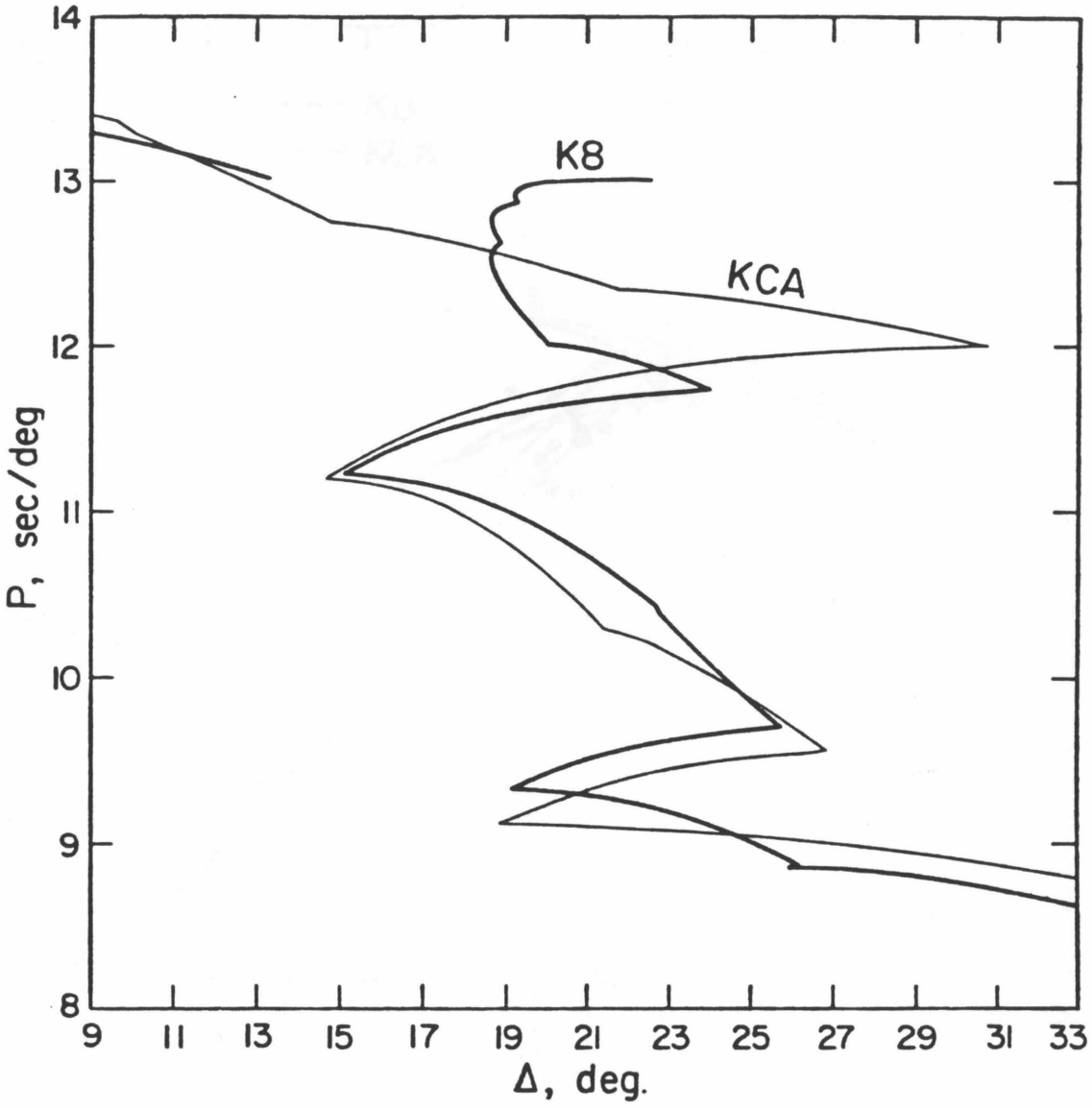

Figure 1.4 Comparison of the $(dT/d\Delta)$ values predicted by models KCA and K8.

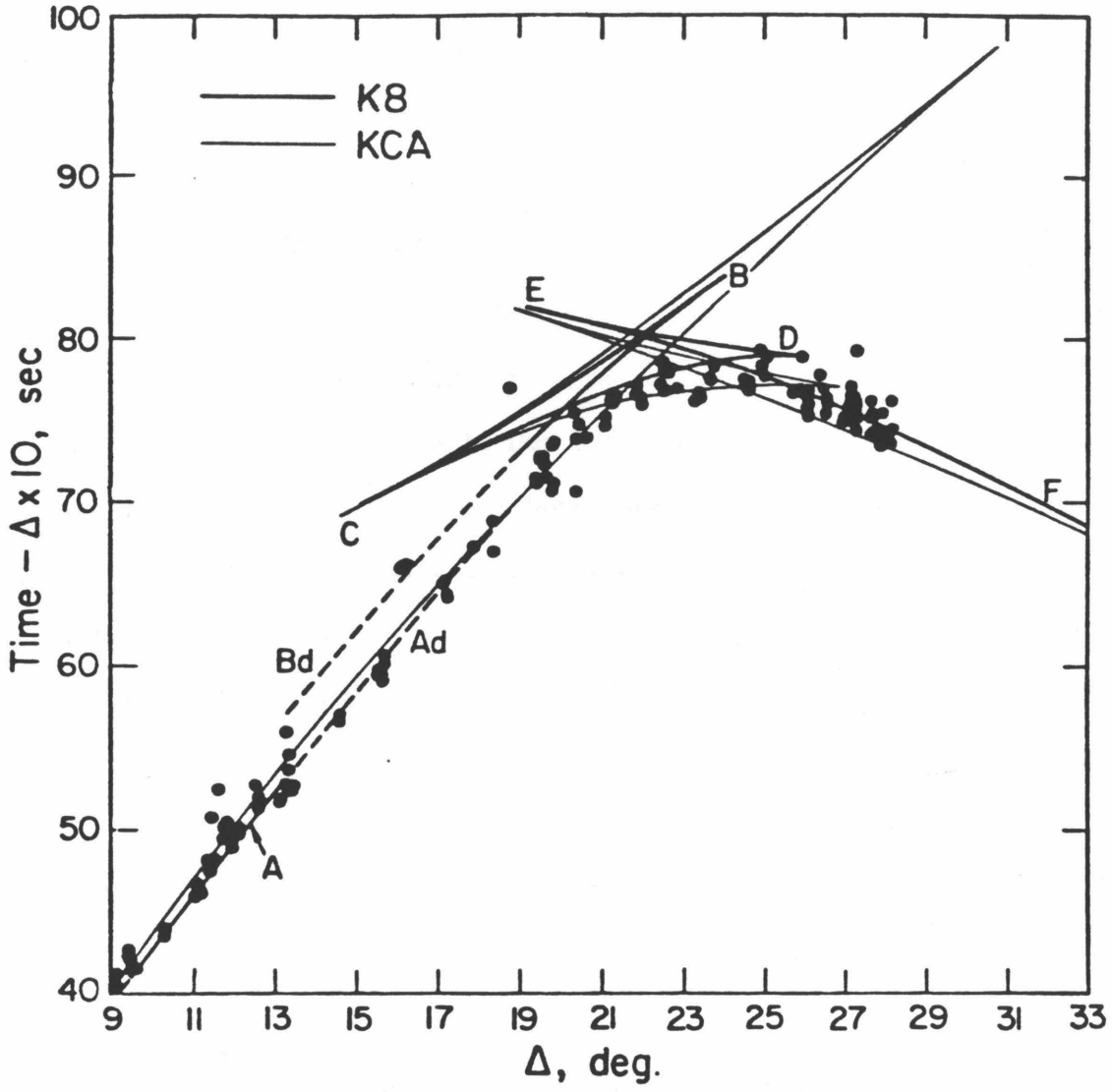

Figure 1.5 Comparison of predicted travel time curve for K8 and KCA and travel times of Novaya Zemlya explosions as reported by the ISC. The letters on the K8 travel time plot label the branches for futher reference in the text. Solid lines indicate direct ray theoretical arrivals, dashed lines indicate the prolongation of certain branches by diffraction due to a low velocity zone.

period seismograms confirm their observation but the phase seems to be limited in regional extent. We saw no evidence that the branch extends beyond 24° on any of the long-period data. The low velocity gradient above 420 km in KCA appears to be incompatible with our interpretation of the waveform observations.

1-4.1 Crustal Structure (0 to 40 km)

The crustal structure of model K8 was taken from KCA, which assumed a single 40 km layer with velocity of 6.4 km/sec. This structure was derived from a synthesis of published data by Der and Landisman (1972). The vertical travel time is consistent with the three layer model derived by Masse and Alexander (1974) and slightly shorter than the more recent model of Vinnik et al. (1978). There are undoubtedly lateral variations in crustal structure within the east European platform that are larger than the differences between these models, so the model actually chosen has no great significance (Vinnik et al., 1978). Since the details of the crustal layering have little effect on the synthetic P-waveshapes beyond 9°, we felt justified in choosing the simplest model available.

1-4.2 Lid and Low Velocity Zone (40 to 300 km)

The profile of the long- and short-period observations that were used to interpret the upper 300 km are shown in Figure 1.6. The long-period P waves from 9° to 11.4° are relatively simple pulses that are essentially a reproduction of the source function. We modeled these seismograms by a simple, smoothly varying velocity structure. The large, later phase at KBS, 11 sec after the first arrival, is most easily explained by PP; however, it is anomalously large at this

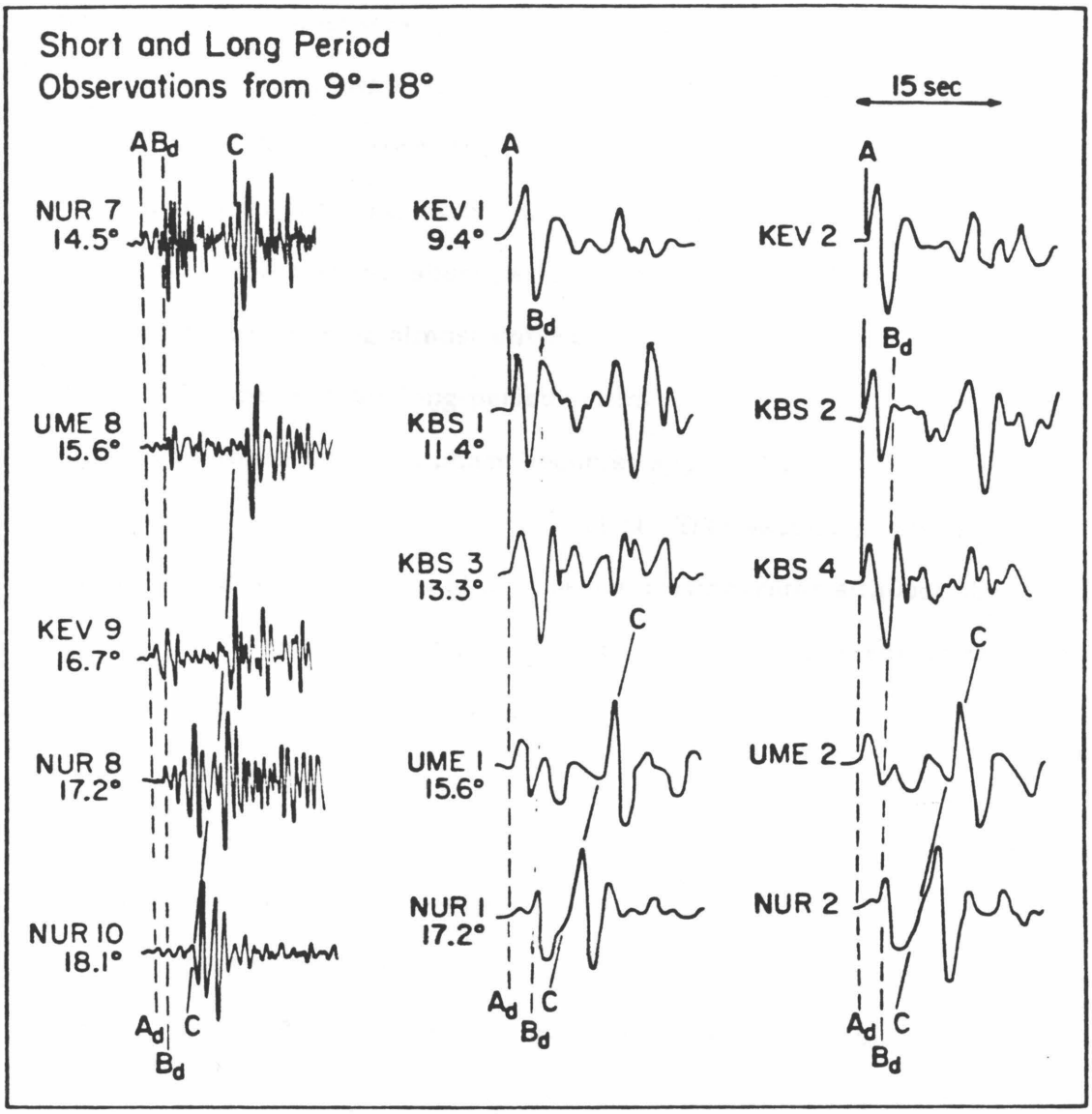

Figure 1.6 Representative seismograms obtained from Novaya Zemlya explosions displaying various arrivals. The lines are keyed to the triplication plots given in Figure 1.5. The number following the station label indicates the event (Table 1.1).

particular station and it does not appear in most of the other observations.

Beyond 13.3° the waveforms begin to show more complexity, the long- and short-period seismograms showing features that are interpreted as upper mantle structure. The most obvious feature on these records is the onset of the CD branch, the reflection from the 400 km discontinuity. Beyond 15° this phase dominates both the long- and short-period seismograms. Another consistent observation is the small, short-period first arrival at 14.5° that grows weaker with distance, becoming almost unobservable on the seismogram at 17.2° in Figure 1.6. The more stable long-period seismograms also confirm this observation of a shadow zone. A second phase becomes apparent on the short-period data at NUR (14.5°) 2-3 sec after the first arrival. This second phase is consistently verified on all of the short and long period seismograms although it is of a variable nature. The onset of the arrival is crucial to the argument for the existence of a low velocity zone near 200 km.

We perturbed the initial model KCA, to fit the long-period records at UME and NUR beyond 15° while trying to preserve the simple nature of the waveforms at the nearer ranges. The results of our modeling efforts are displayed in Figures 1.7 and 1.8 where we have included the synthetics for model KCA for comparison. In both figures it can be seen that the relatively simple structure above 420 km in KCA cannot predict the complexities observed in the data. Furthermore, the relative amplitude of the first arrival in KCA is much too large on both the long- and short-period synthetics. By introducing the low velocity zone we were able to produce a shadow zone and predict the proper decay of the initial arrival P(Ad) with range. By limiting the extent of the low velocity zone we were able to explain the second arrival on the long-period seismograms as a reflection

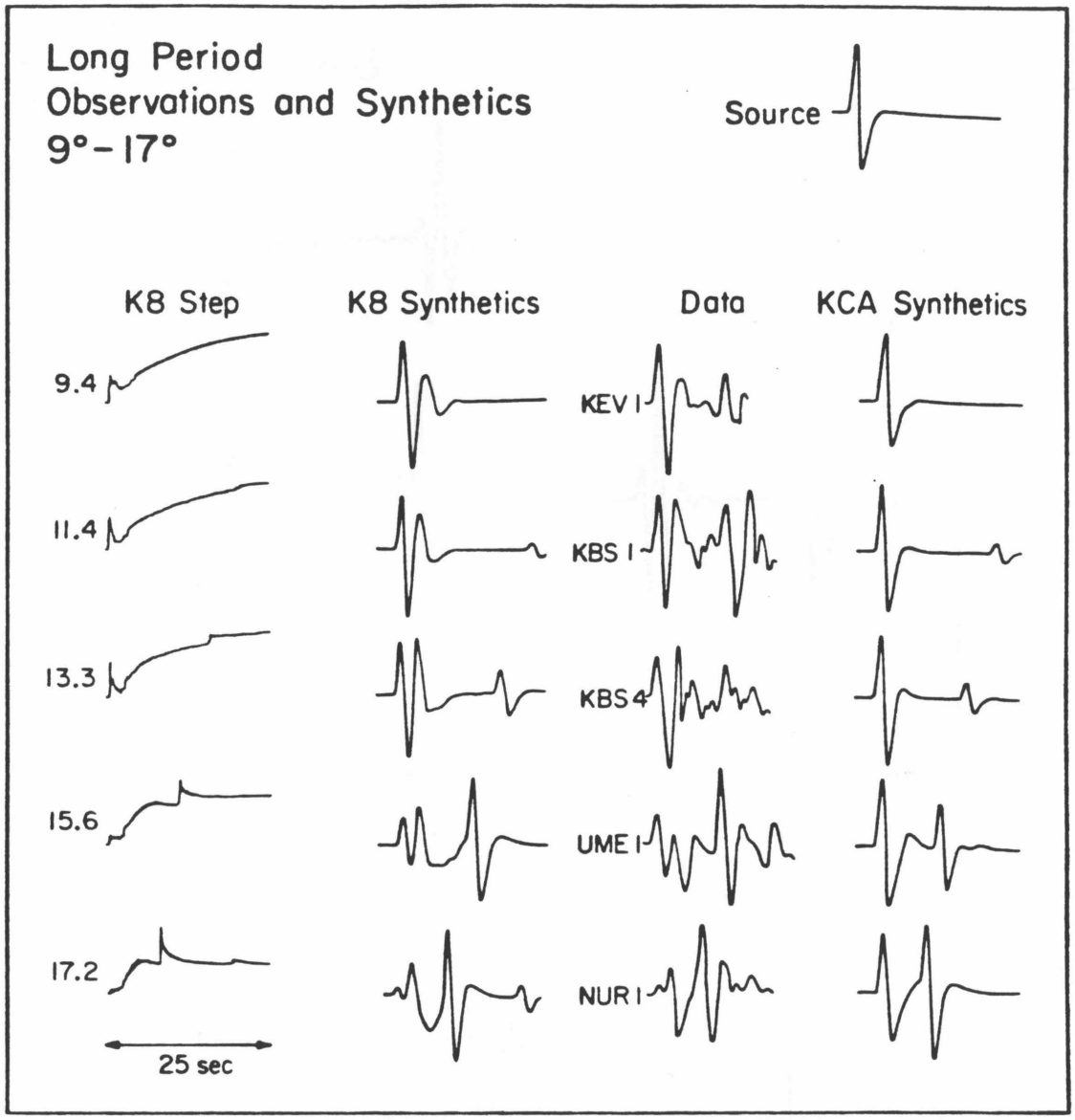

Figure 1.7 Comparison of synthetics with the long-period waveform data. The convolution of source function given in the right-hand corner with the derivative of the step responses yields the synthetics.

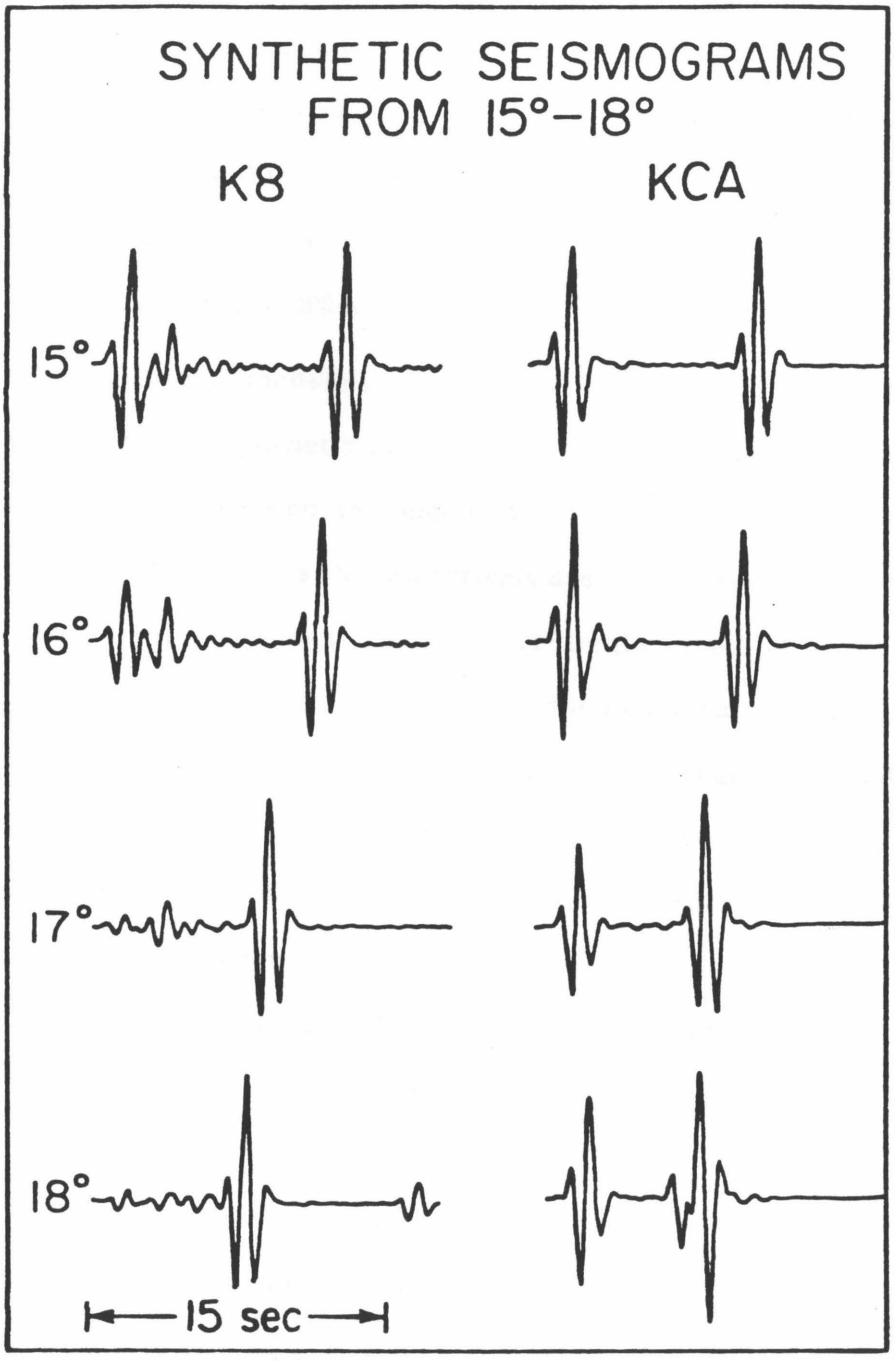

Figure 1.8 Short-period synthtics for KCA and K8 which can be compared with the data in Figure 1.6.

from the gradient beneath the LVZ. The details of the LVZ and gradient below are somewhat uncertain due to lateral heterogeneities and unknown Q structure (see later discussion). However the evidence for a shadow zone in our data, Figure 1.6, and in King and Calcagnile's (1976) record sections (their Figures 2b and 2c) is very good. Resolution of this structure is important to accurately determine the structure below 300 km depth.

The capability of modeling low velocity zones is one of the advantages of using the method of synthetic modeling. Previous array studies have used the Wiechert-Herglotz inversion technique for travel time and apparent velocity data. This method assumes that all arrivals are direct rays and therefore it cannot resolve low velocity zones. The Wiechert-Herglotz method is still useful if low velocity zones can be recognized a priori and included explictly in the inversion. The data presented by King and Calcagnile, while suggestive, did not justfy including any additional structure above 420 km and thus their model is too simple in this region. Our data clearly require some structure above 200 km and our synthetic calculations indicate that we are observing diffraction effects caused by a low velocity zone. These calculations enable us to determine the extent of the shadow zone where $(dT/d\Delta)$ observations should be interpreted with caution.

1-4.3 Transition Region (300 to 800 km)

The seismograms used in modeling the transition region are particularly interesting as can be surmised by noting the intersections of the triplication plots in Figure 1.5. As in the previous section, we relied heavily on the long-period waveform data in determining the branch positions and the resulting

model. The synthetics and representative waveform for these ranges are displayed in Figure 1.9 where the observed waveforms are somewhat variable in quality. For instance, the KON (21.1°) observation is the only seismogram at that range from an explosion at the southern Novaya Zemlya site and is a weak recording. On the other hand, KON (21.9°) is from the northern site where large shots were abundant. Some examples are given in Figure 1.10, where events 1 and 2 are the same events pictured in Figure 1.7. Thus, we considered this waveform as particularly worthwhile to model. The same situation occurs for the COP (24.6°) observation. In general, these waveforms are extremely difficult to model using a trial and error inversion technique because each record is essentially an interference phenomenon where small changes in the source or model can drastically alter the waveform.

One of the principal differences between K8 and KCA is the gradient above the 400-km discontinuity. Part of the difference is due to the low velocity zone, which changes the bottoming depth of rays from above 420 km. To predict correctly the relative arrival times we increased the gradient between 300 and 400 km and reduced the size of the 400 km discontinuity. With these changes we were able to model the interference at 21.9° and the cut-off of the long-period AB branch. At 21.1° the relative arrival times of the phases predicted by K8 fit better than those calculated for KCA. However there is some mismatch in the relative amplitudes with the arrival from above the 420-km discontinuity being too large. The choice of velocity gradient below 270 km depends crucially on how we modeled the low velocity zone. Any errors in determining the model or any lateral heterogenity in the upper 250 km will seriously affect our inversion for the structure between 280 and 400 km. The uncertainties in K8 are probably

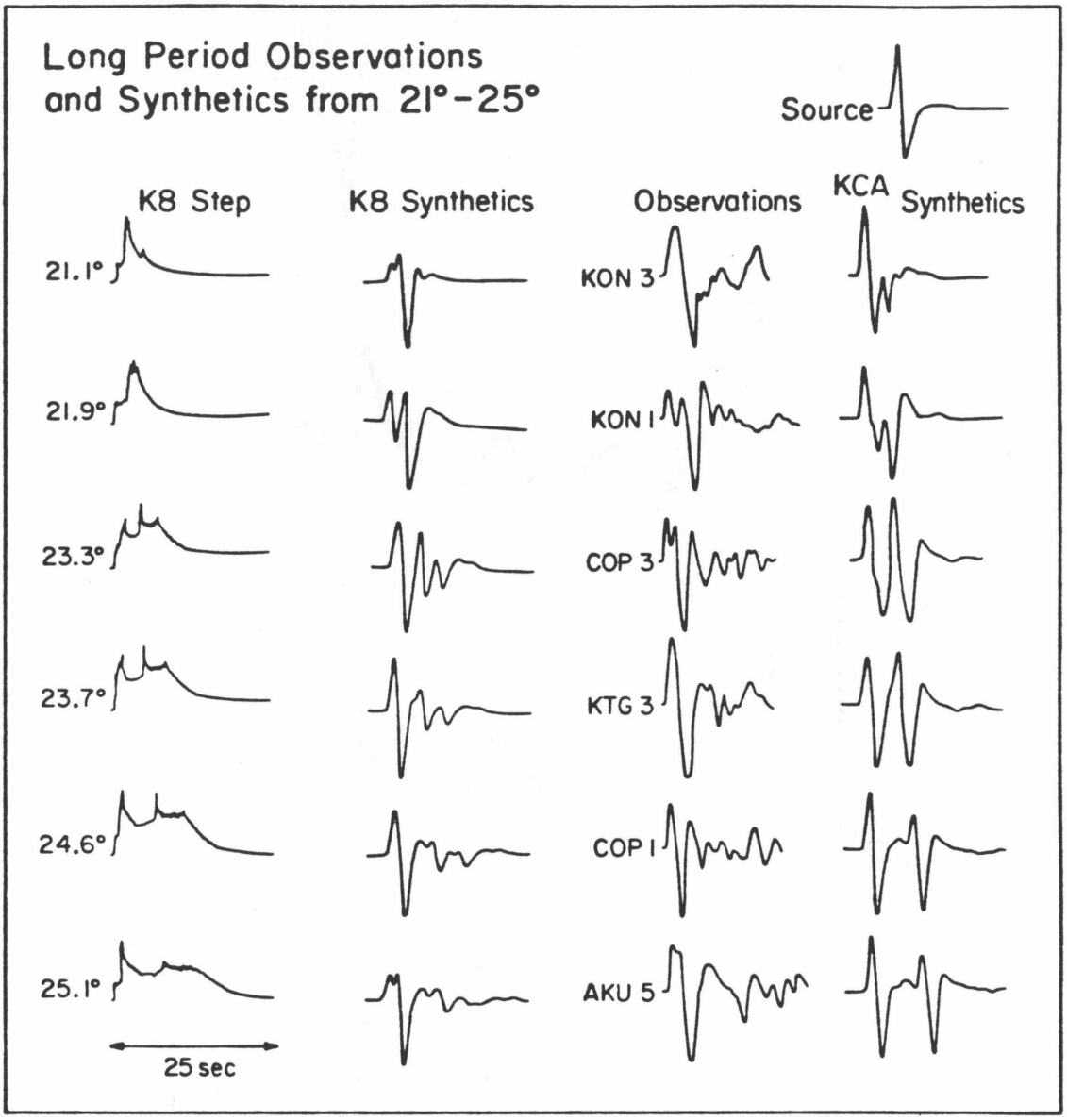

Figure 1.9 Comparison of the observed waveforms with synthetics. K8 synthetics were produced by a convolution of the source function displayed in the right-hand corner with the derivative of the step responses.

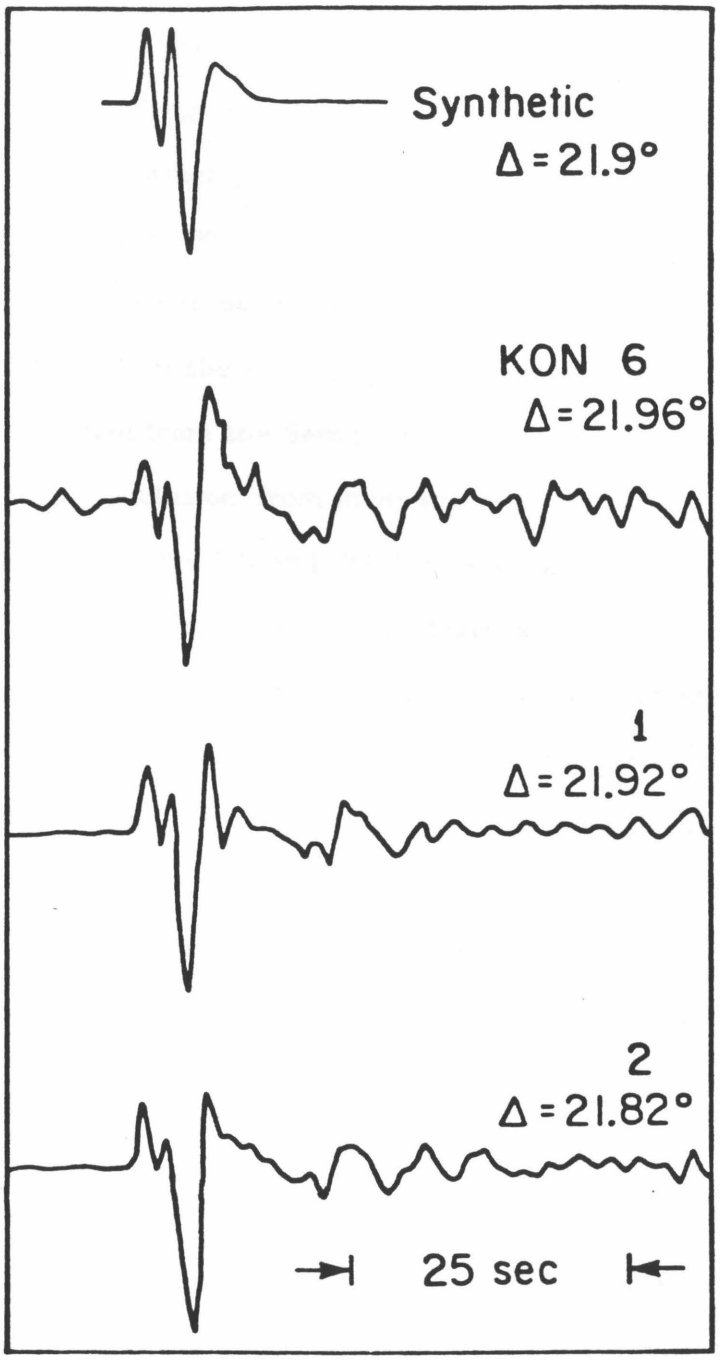

Figure 1.10 Comparison of synthetics (K8) with observations from various events at the Northern Novaya Zemlya test site, indicating source variability.

greatest in this depth range.

The evidence for a discontinuity at 675 km is clear in King and Calcagnile's array data and in our long- and short-period observations. The reflection is first evident as a clear distinct pulse at 23.3° (COP) where the E-F phase is the second pulse. At 25.1° AKU, the E-F arrival is first and the shoulder on the waveform is interpreted to be the C-D phase moving back. The best data showing the position of D on the C-D branch is displayed in Figure 1.11 where the observations obtained from the Semipalatinsk test site are compared with synthetics. The main conclusion from modeling these obsrvations is the increased velocity gradient between 670 and 750 km (see Figure 1.2) that increases the amplitude of the first arrival beyond 25 degrees. Such a feature is also consistent with the long-period observations at COP (23.3°) and AKU (25.1°). At COP (23.3°) the strong second arrival relative to the first arrival indicates that the gradient below the 670 km discontinuity must be comparable to the gradient between 400 and 670 km. The disparity between synthetic and observation can be explained to some extent by the relative timing of the two arrivals. If we change the range used in the calculations by 25 km the fit would be better. At still larger ranges, we saw no compelling evidence for the C-D branch, (Figures 1.12 and 1.13).

Examples of the short-period observations are shown in Figures 1.12 and 1.13. K8 fits the data as well as KCA, however, it is obvious that for ranges 20-25 degrees these data could hardly be used for distinguishing between the two models. One observation which can be made from these figures is that, although of marginal use for inversion, the complexities in the seismograms can be modeled quite well. With a few exceptions these seismograms seem to indicate

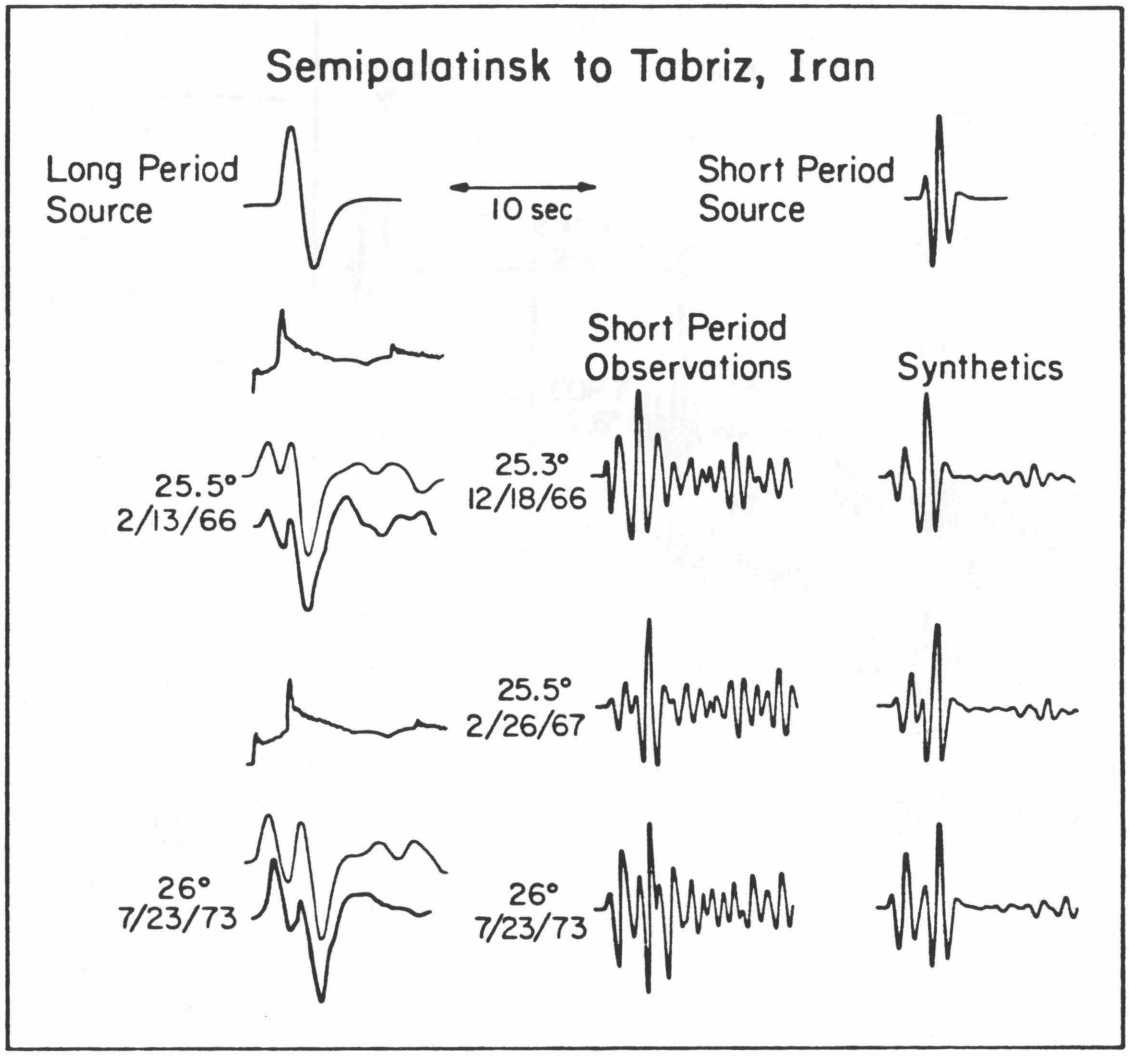

Figure 1.11 Observations at Tabriz, Iran, from nuclear explosions in Semipalatinsk. The data clearly show evidence for the 675 km discontinuity and the position of the end of the C-D branch.

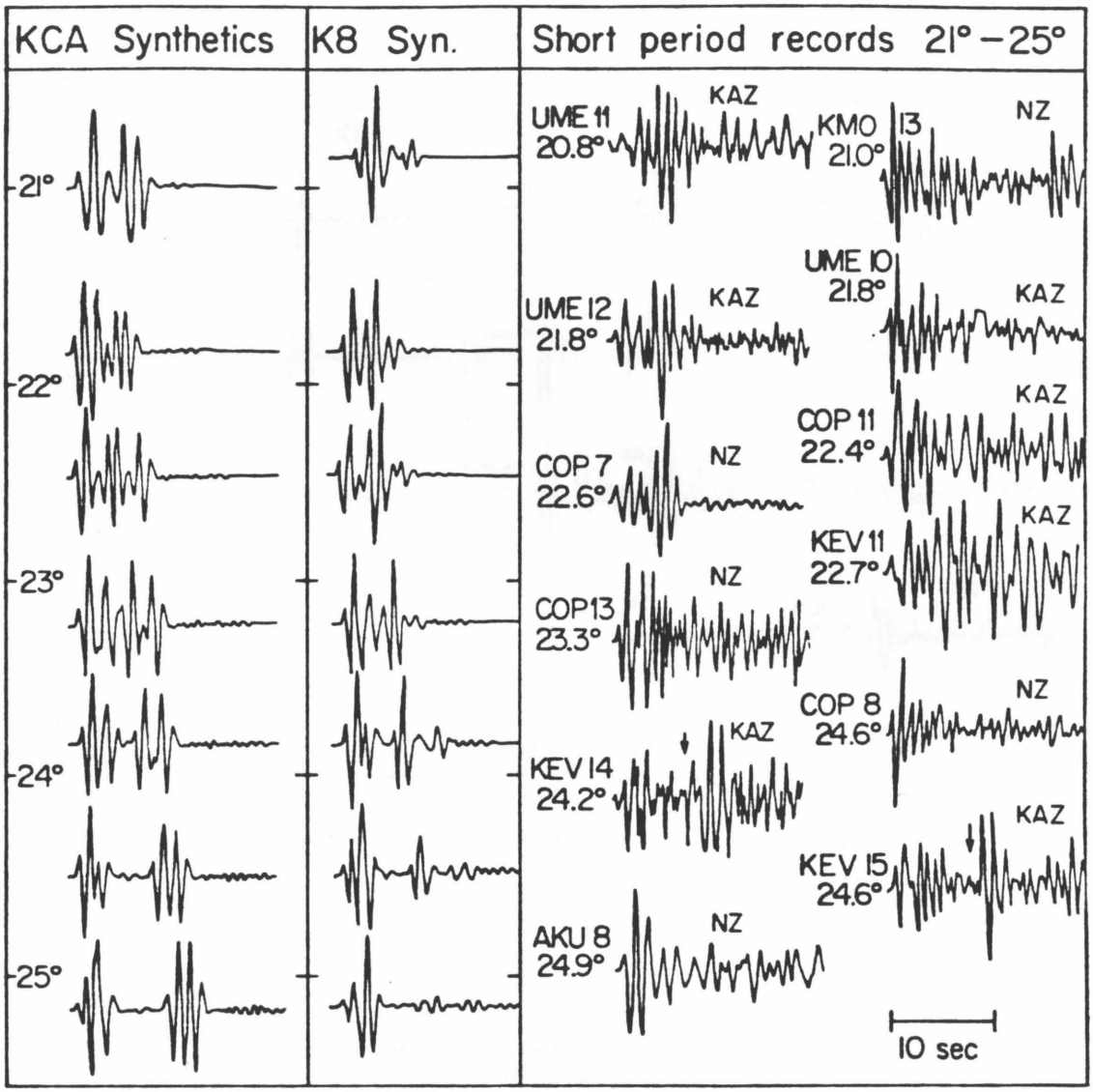

Figure 1.12 Theoretical seismograms from K8 fit the short-period seismograms as well as KCA. The inconsistency of the records between 24 and 25° should be noted. The large later phase indicated by the arrows is similar to the arrival of King and Calcagnile (1976) interpreted as the reflection from the 420-km discontinuity.

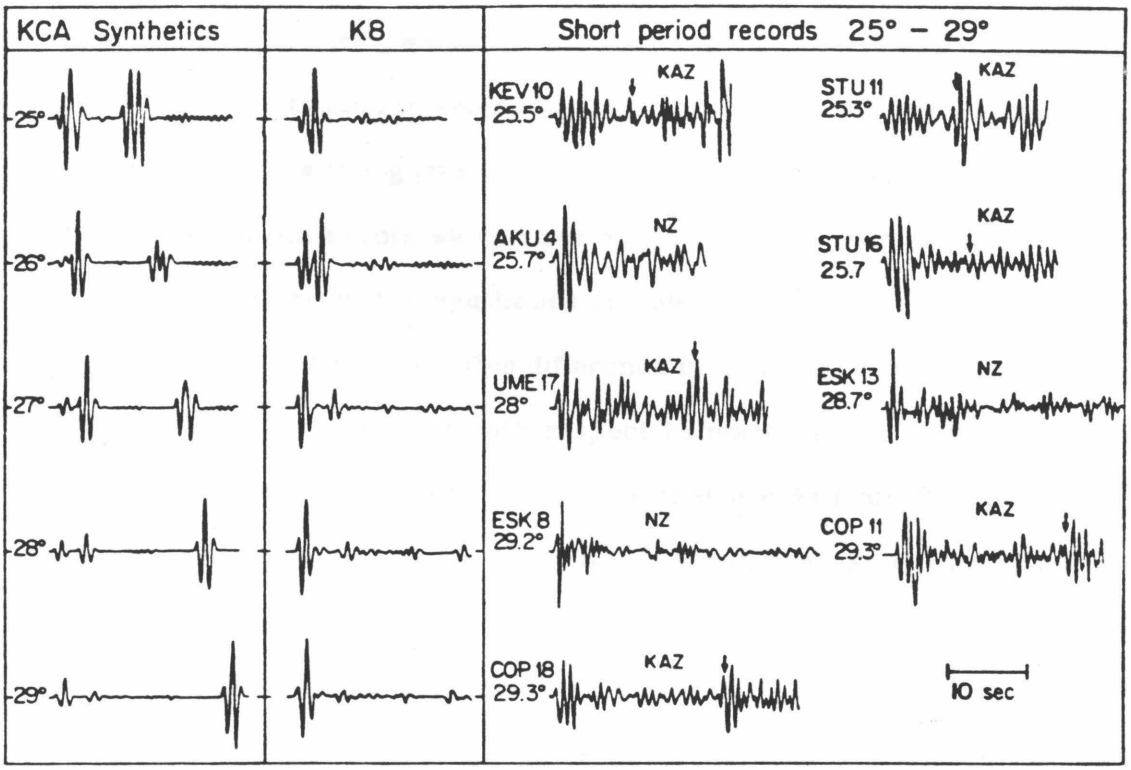

Figure 1.13 The figure compares theoretical and observed seismograms from 25 to 29°. Again note the occasional appearance of the reflection from the 420-km discontinuity, marked by the arrows. This appears to be a regional phenomenon, observed only from sources in Kazakh and receivers in northwest Europe.

that the salient features are indeed due to upper mantle structure and not anomalous source or receiver complications. For this reason as we look at larger ranges 25-30°, some puzzling features become evident.

If we restrict our attention to only NZ events we see relatively simple seismograms beyond 27°, which are in agreement with our model. On the other hand, Kazakh events tend to show a major secondary arrival out to larger ranges (labeled by an arrow in Figures 1.12 and 1.13). Since King and Calcagnile (1976) used mostly Kazakh events we can see why their AB branch extends to larger ranges. This feature in the synthetics for their model is the result of the low gradient above 420 km. Thus, this difference in data suggests lateral variations in velocity as deep as 400 km with respect to northern and southern Eurasia. The difficulties with this interpretation are that events from Semipalatinsk do not show this feature,see Figure 1.11, and that many Kazakh events do not show this branch, for example see KEV (10) and STU (16). It should also be noted that the onset of the AB branch becomes less impulsive with distance and looks more like the onset of a wavetrain (Figures 2k-2m of King and Calcagnile, 1976). Perhaps this phenomenon could be caused by multipathing due to small-scale irregularities. It would be particularly interesting to obtain some long-period seismograms that sample this region so that a comparison similar to Figure 1.14 could be made.

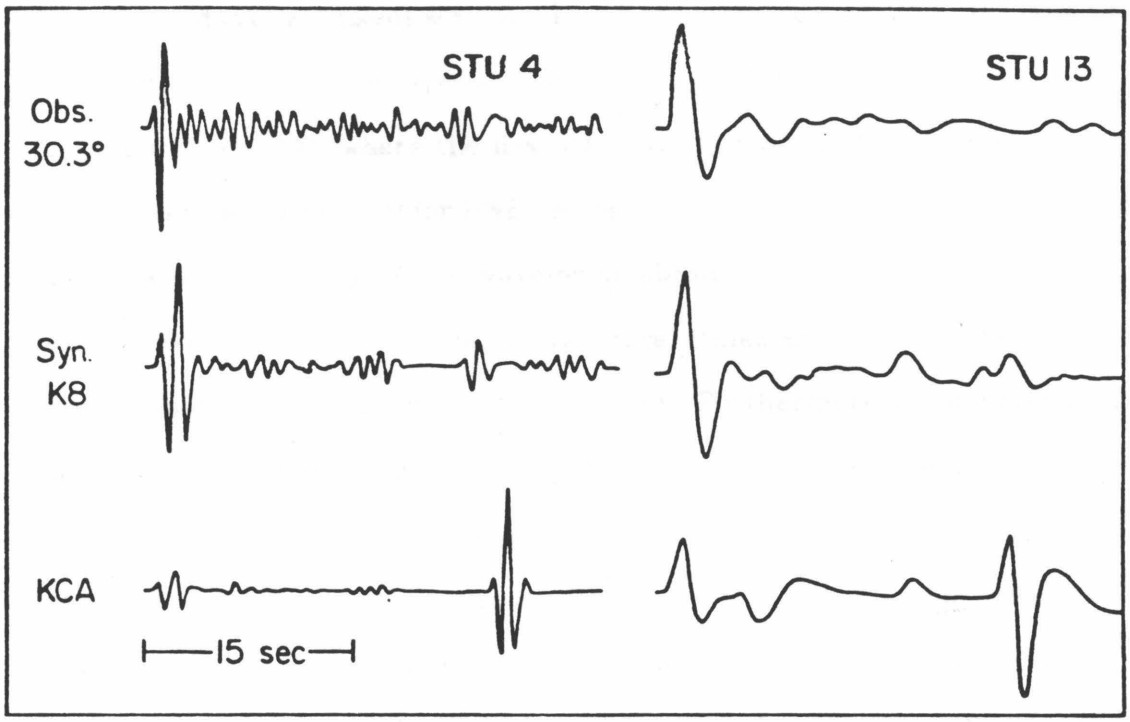

Figure 1.14 Theoretical and observed seismograms of Novaya Zemlya explosions recorded at STU (Δ=30.0°). Model KCA predicts a large reflection from the 420-km discontinuity indicated by the arrows, which is not evident in the data.

1-5 Discussion

It is interesting to compare model K8 with models proposed for western United States (WUS), see Figure 1.15, where the same basic modeling techniques were applied. Models HWA and HWB were derived from ($dT/d\Delta$) measurements (Johnson, 1967), travel times from the NTS explosions and short-period waveform data as discussed earlier. The travel times and δt separations between the triplication arrivals for HWB and HWA are substantially different between 13 and 19°, where the first arrivals appropriate for the HWA region are from 3 to 6 sec later than for HWB. Model T7 was constructed to fit the HWA data set as well as the long-period waveforms obtained from a series of well-studied earthquakes. On the other hand, the travel times and δt's for the model HWB are compatible with those predicted by K8. Furthermore a comparison of the short-period seismograms displayed in Figure 1.6 are quite similar to the short-period profile presented by Helmberger and Wiggins (1971, their Figure 2). At ranges beyond 20°, the distinction between the regionalization HWA and HWB disappears and there appears to be little evidence of lateral variations below this depth. The slight offsets in discontinuities reflect the lid and LVZ disparity, which is worth a brief review.

The upper 200 km and T7 was constructed to fit the average travel times and amplitude properties of WUS where appears to be an effective shadow zone along some profiles (Helmberger, 1973b). This effect can be caused by an LVZ as in T7 but it could be caused by lateral changes in velocity across the boundaries of the various structural provinces, for instance see York and Helmberger (1973). Thus, the basic vertical structure of HWB or K8 may be more appropriate for some portions of the northern Western U. S. and the known short-period

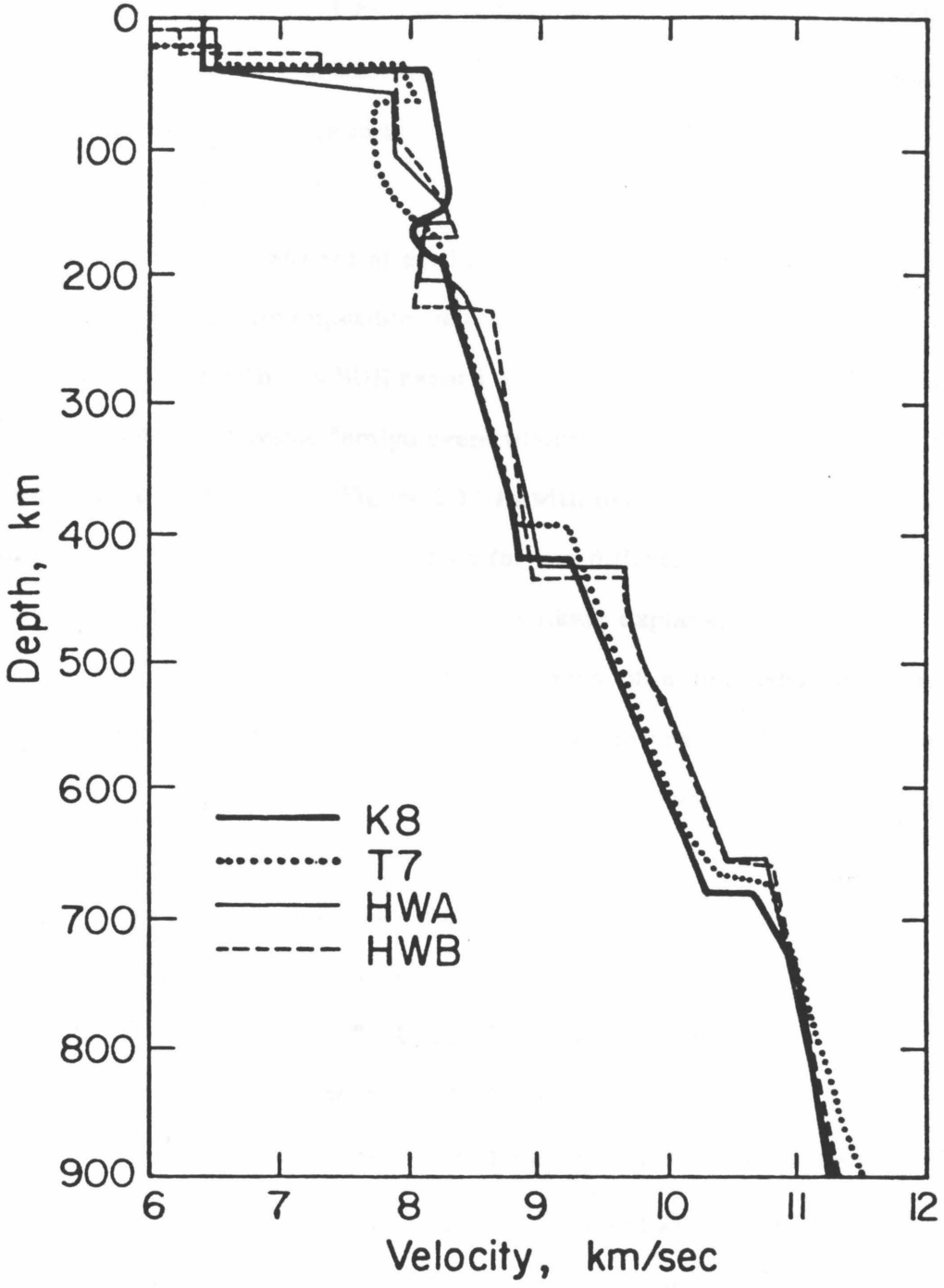

Figure 1.15 Comparison of model K8 with models HWA, HWB and T7 derived from WUS observations.

amplitude pattern caused by horizontal changes in velocity. Small changes in the velocity structure of the lid and LVZ can make a dramatic change in synthetic seismograms at the near-in distance of 8 to 19° as can be seen by the following case study.

In collecting a data set of seismograms one invariably finds an odd observation that appears incompatible in travel time and waveshape with the others. Such is the case with the NUR record displayed in Figure 1.16. NUR is a recording of a southern Novaya Zemlya event whereas UME was produced by a northern Novaya Zemlya event, see Figure 1.1. As with nearly all of the long-period obsertvatons, the NUR record is duplicated for two different events so that an unusual source function does not appear to be a likely explanation for the difference in waveforms. Explaining this record in terms of a perturbation of model K8 prroved to be quite easy and enlightening. By slowing the first arrival by about 1 sec relative to the reflection from below the low velocity zone and the 420 km discontinuity, we can reproduce the relative timing of the seismograms. The result is model K8' shown in Figure 1.17. Note that we have also slightly decreased the depth to the low velocity zone. Another characteristic of the model is that a critically reflected arrival now comes from below the low velocity zone; i.e., the shadow zone ends at 15° rather than 19°. This feature substantially increases the amplitude of the second arrival relative to the C-D reflection.

We conclude that the upper mantle in northwestern Eurasia is somewhat variable. Model K8 may average over variations as large as those between K8 and K8' so that the detailed features of K8 may be considered to be exemplary. The trade-offs involved in modeling low velocity zones are well-known, (Dowling and Nuttli, 1964; Helmberger, 1973b). To more fully constrain the features of a

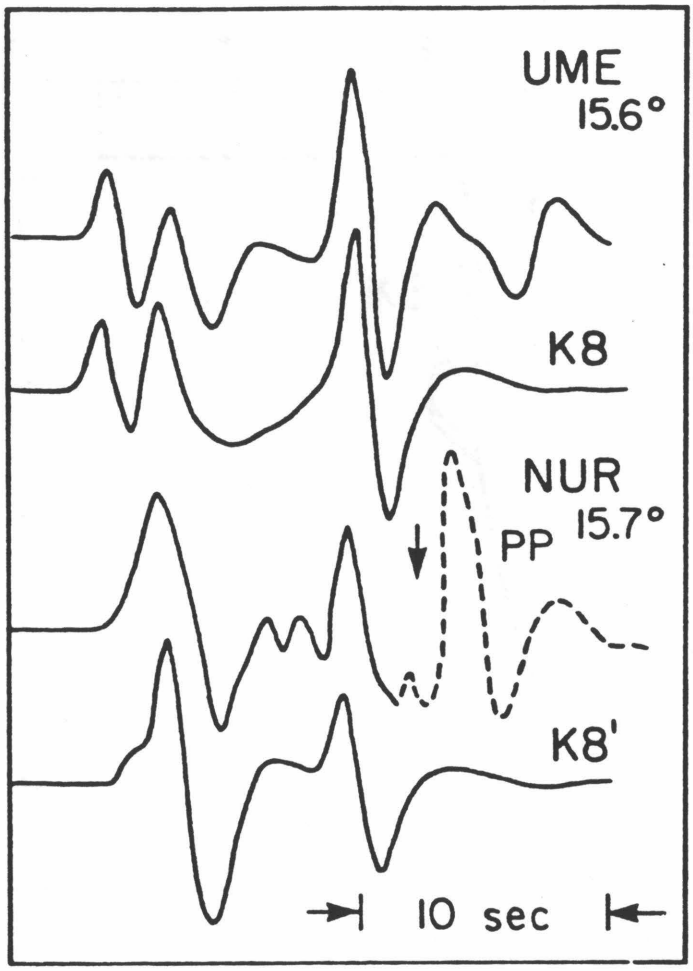

Figure 1.16 Seismograms from Northern Novaya Zemlya to UME and from southern Novaya Zemlya to NUR. These seismograms are along slightly different azimuths. The difference can be explained by variation in the velocity structure above 180 km (see Figure 1.17).

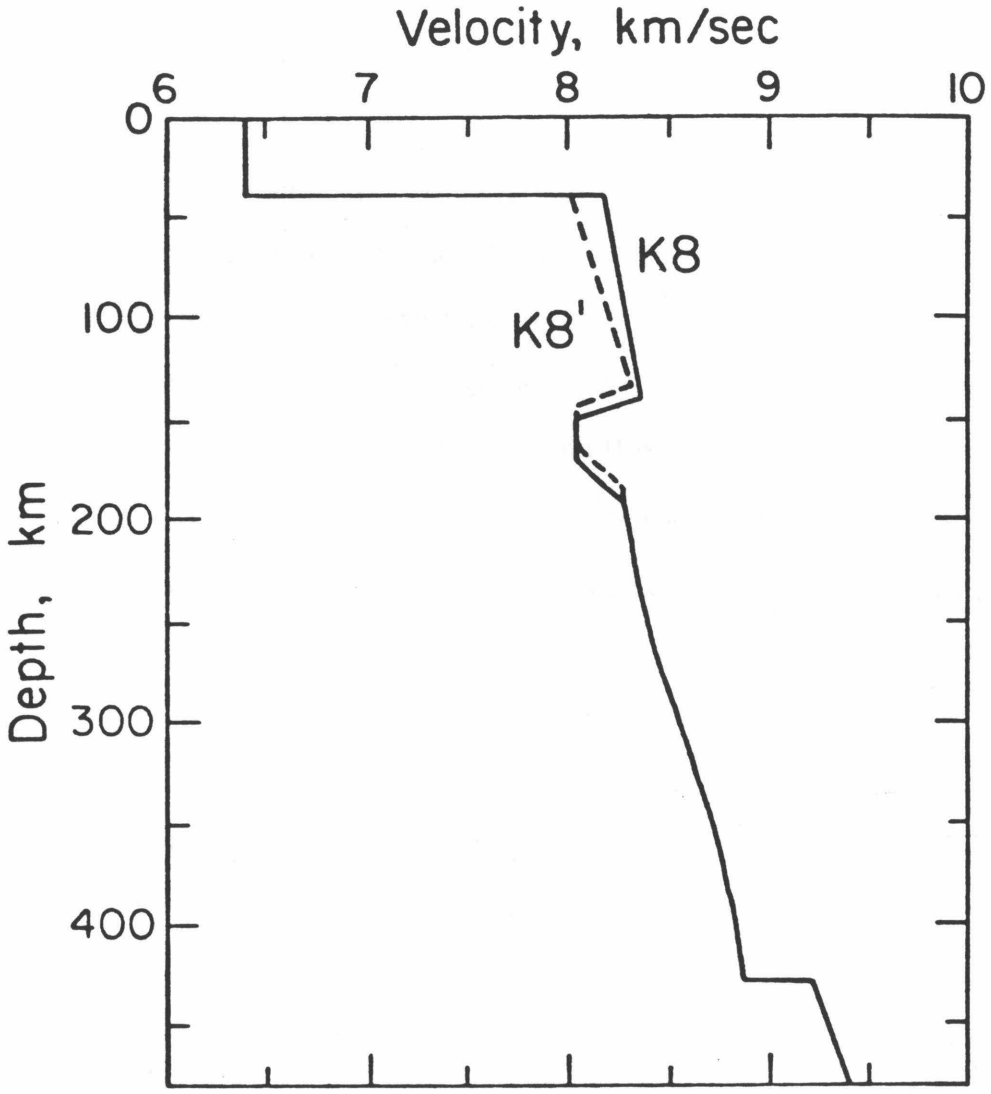

Figure 1.17 Model K8' which was derived from K8 to explain the variation at 15.6°, see Figure 1.16.

low velocity zone, we need to incorporate longer-period data from earthquake sources. Figure 1.18 complements Figures 1.16 and 1.17 by comparing long-period and short-period synthetics for K8 and K8'. The long-period seismograms are from an earthquake source appropriate for the March 23, 1978 Bermuda event (Gordon Stewart, personal communication). The long-period seismograms are very similar, hence their usefulness in constraining the overall features of the model such as the average gradients and the sizes of discontinuities. The short-period data are more sensitive to small scale details. The need to consider broad-band information, long- and short-period waveshapes as well as $dT/d\Delta$ and travel time data, is obvious from this series of figures.

The low velocity zone in K8 is a feature that has not been included in any of the models proposed in the high quality array studies undertaken. This is probably due to the effect of lateral heterogeneities and the inherent difficulty in recognizing shadow zones on short period data. However observations of structure around 200 km in Europe and other regions have been reported in the literature. Lehmann (1959) studied the travel times of P-waves in Europe and proposed a discontinuity at 220 km. She has also studied North America (Lehmann, 1962, 1967), reporting similar structure there. Other studies using different analytical techniques have had similar results. Whitcomb and Anderson (1970) found a strong reflector at around 200 km by analyzing precursors to P'P'. Sacks et al. (1977) observed P to SV conversions, which they modeled as having originated from the base of the low velocity zone between 200 and 250 km beneath the Baltic shield. Cara (1979) has found high velocity gradients at 200 km beneath the U.S. and the western Pacific from the analysis of high mode Rayleigh waves. Anderson (1979) reviews the various studies and concludes there is

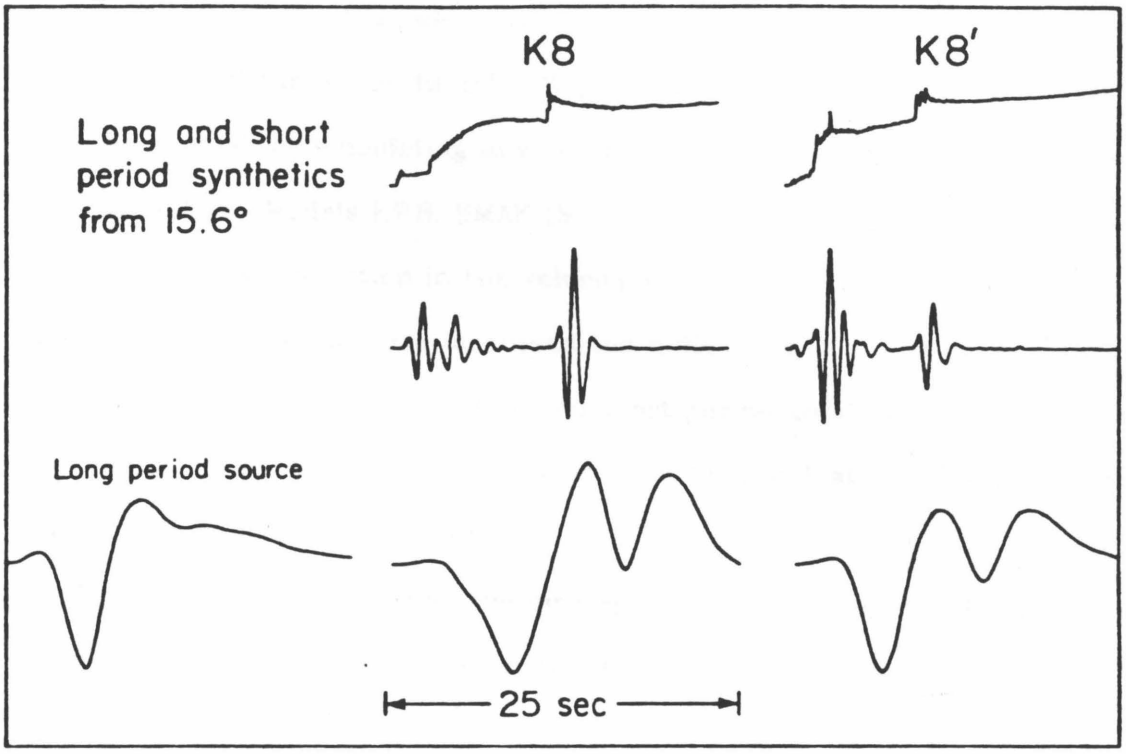

Figure 1.18 Short- and long-period synthetics for K8 and K8'. The long-period source function is from the March 23, 1978 Bermuda earthquake (G. Stewart, personal communication).

a worldwide discontinuity at the base of the low velocity zone at 220 km. In order to resolve the characteristics of this feature, additional studies are required, taking into account the effect of lateral heterogeneity and attenuation on travel times and waveforms.

It is unfortunate that we do not have a very dense coverage of long-period receivers at distances of 19-25°. The high-frequency explosion source would have been ideal for elucidating any additional structure between the two major discontinuities. Models HWB, SMAK (Simpson et al., 1974), and ARC-TR (Fukao, 1977) all have an inflection in the velocity structure at about 550 km. Burdick and Helmberger (1978) have discussed the difficulties in observing this feature. The effect of the proposed inflection on short-period amplitudes is smaller than the regional variation due to receiver structure and attenuation. The long-period observations average too much of the mantle to resolve such a small feature. However, considering the discrepancies in the observed and predicted waveforms the structure between the two discontinuities remains somewhat uncertain.

In summary, we have incorporated the long-period and short-period waveform data with travel time and apparent velocity measurements to derive the model K8 (Table 1.2) for Northwest Eurasia. The significant features of the model are:.

(1) A low velocity zone between depths of 150 and 200 km;

(2) A 4.5 % velocity increase at 420-km depth;

(3) A large velocity gradient between 420 and 675 km;

Table 1.2 Velocity Model K8

Velocity	Depth	Velocity	Depth	Velocity	Depth	Velocity	Depth
6.39	0	8.392	250	9.572	496	10.955	749
6.40	1	8.419	260	9.583	506	10.998	759
8.170	40	8.445	270	9.624	517	11.040	770
8.187	50	8.478	280	9.667	528	11.061	783
8.205	60	8.511	290	9.708	539	11.083	796
8.222	70	8.545	300	9.750	550	11.105	808
8.239	80	8.578	310	9.792	560	11.127	821
8.256	90	8.612	320	9.834	570	11.148	834
8.274	100	8.645	330	9.876	580	11.170	847
8.291	110	8.678	340	9.818	590	11.192	859
8.308	120	8.712	350	9.960	604	11.213	872
8.325	130	8.745	360	10.003	610	11.235	885
8.343	140	8.764	370	10.045	620	11.256	898
8.250	150	8.783	380	10.090	631	11.278	911
8.180	155	8.803	391	10.135	641	11.300	923
8.050	160	8.822	400	10.180	653	11.321	963
8.040	170	8.841	410	10.225	664	11.343	949
8.150	180	9.24	420	10.660	675	11.365	962
8.270	190	9.292	431	10.702	686	11.385	974
8.287	200	9.333	442	10.744	696	11.408	987
8.305	210	9.375	452	10.789	707		
8.323	220	9.415	467	10.829	717		
8.340	230	9.458	474	10.891	728		
8.366	240	9.50	485	10.913	738		

(4) A 4 % velocity increase at 675-km depth.

Model K8 is similar to model T7 proposed recently for the Western United states; however, without a detailed determination of the uppermost velocity structure, any discussion of lateral heterogeneity is premature.

References

Anderson, D. L., (1979), The deep structure of continents, *J. Geophys. Res.*, *84* ,7555-7560.

Burdick, L. J. and D. V. Helmberger, (1978), The upper mantle P-velocity structure of the western United States, *J. Geophys. Res.*, *83* , 1699-1712.

Burdick, L. J. and D. V. Helmberger, (1979), Time functions appropriate for nuclear explosions, *Bull. Seism. Soc. Am.*, *69* , 951.

Burdick, L. J. and C. A. Langston, (1977), Modeling crustal structure through the use of converted phases in teleseismic body waveforms, *Bull. Seism. Soc. Am.*, *67*, 677-691.

Burdick, L. J. and J. A. Orcutt, (1979), A comparison of the generalized ray and reflectivity methods of waveform synthesis, *Geophys. J. R. Astr. Soc.*, *58* , 261.

Cara, M, (1979), Lateral variations of S velocity in the upper mantle from higher Rayleigh modes, *Geophys. J. R. Astr. Soc.*, *57* , 649-670.

Carpenter, E. W., (1966), Absorption of elastic waves - an operator for a constant Q mechanism, *AWRE Report No. 0-43/66* , 16 pp.

Der, Z. A. and M. Landisman, (1972), Theory of errors, resolution and separation of unknown variables in inverse problems with application to the mantle and

the crust in southern Africa Scandanavia, *Geophys. J. R. Astr. Soc.*, *27*, 137.

Dey-Sarkar, S. K., and R. A. Wiggins, (1976),Upper mantle structure in Western Canada, *J. Geophys. Res.*, *81*, 3619.

Dowling, J., and O. Nuttli, (1964), Travel time curves for a low velocity channel in the upper mantle, *Bull. Seism. Soc. Am.*, *54*, 1981.

England, P. C., M. H. Worthington and L. W. King, (1977), Lateral variation in the structure of the upper mantle beneath Eurasia, *Geophys. J. R. Astr. Soc.*, *48*, 71-79.

England, P. C., and B. L. N. Kennett and M. H. Worthington, (1978), A comparison of the upper mantle structure beneath Eurasia and the North Atlantic and Arctic Oceans, *Geophys. J. R. Astr. Soc.*, *54*, 575-585.

Fukao, Y., (1977), Upper mantle P-structure at the trench side of the Japan-Kurile arc, *Geophys. J. R. astr. Soc.*, *50*, 621.

Futterman, W. I., (1962), Dispersive body waves, *J. Geophys. Res.*, *67*, 5279.

Helmberger, D. V., (1973a), Numerical seismograms of long-period body waves from seventeen to forty degrees, *Bull. Seism. Soc. Am.*, *64*, 45.

Helmberger, D. V., (1973b), On the structure of the low velocity zone, *Geophys. J. R. Astr. Soc.*, *34*, 241.

Helmberger, D. V., and L. J. Burdick, (1979), Synthetic seismograms, *Ann. Rev. Earth. Planet. Sci.*, *7*, 417.

Helmberger, D. V. and R. A. Wiggins, (1971), Upper mantle structure of the midwestern United States, *J. Geophys. Res.*, *76*, 3229.

Johnson, L. R., (1967), Array measurements of P-velocities in the upper mantle, *J. Geophys. Res.*, *92*, 6309.

Kennett, B. L. N., (1975), The effects of attenuation seismograms, *Bull. Seism. Soc. Am.*, *65*, 1643.

King, D. W. and G. Calcagnile, (1976), P-wave velocity in the upper mantle beneath Fennoscandia and Western Russia, *Geophys. J. R. Astr. Soc.*, *46*, 407.

Lehmann, I., (1959), Velocities of longitudinal waves in the upper part of the earth's mantle, *Ann. Geophysique*, *15*, 93-118.

Lehmann, I., (1962), The travel times of the longitudinal waves of the Logan and Blanca atomic explosions and their velocities in the upper mantle, *Bull. Seism. Soc. Am.*, *52*, 519.

Lehmann, I., (1967), On the travel times of P as obtained from the nuclear explosions Bilby and Shoal, *Phys. Earth and Planet. Int.*, *11*, 14-23.

Masse, R. P. and S. S. Alexander, (1974), Compressional velocity distribution beneath Scandanavia and Western Russia, *Geophys. J. R. Astr. Soc.*, *39*, 587.

Romney, C. B., B. G. Brooks, P. H. Mansfield, D. S. Carter, J. N. Jordan, and D. W. Gordon, (1962), Travel times and amplitudes of principal body phases recorded from Gnome, *Bull. Seis. Soc. Am.*, *57*, 829.

Sacks, I. S., J. A. Snoke and E. S. Husebye, (1977), Lithospheric thickness beneath the Baltic Shield, *Carnegie Inst. Year Book 76*, 805-822.

Simpson, D. W., R. F. Mereu and D. W. King, (1974), Array study of P-wave velocities in the upper mantle transition zone beneath Northeastern Australia, *Bull. Seism. Soc. Am.*, *61*, 1751.

Vinnik, L. P., V. Z. Ryaboy, L. N. Starobinets, A. V. Egorkin and N. M. Chernyshev, (1978), Velocity of P-wave in the upper mantle of the East European platform, *Proc. (Dokl.) Acad. Sci. USSR*, *70*, 244 (in Russian).

von Seggern, D. and R. Blandford, (1972), Source time functions and spectra for underground nuclear explosions, *Geophys. J. R. Astr. Soc.*, *31*, 83.

Whitcomb, J. H. and D. L. Anderson, (1970), Reflections of P'P' seismic waves for discontinuities in the mantle, *J. Geophys. Res.*, *75*, 5714-5728.

Wiggins, R. A., (1969), Monte Carlo inversion of body wave observations, *J. Geopyhs. Res.*, *74*, 3171.

Wiggins, R. A. and D. V. Helmberger, (1973), Upper mantle structure of the western United States, *J. Geophys. Res.*, 78, 1870.

York, J. E. and D. V. Helmberger, (1973), Low velocity zone variation in the southwestern United States, *J. Geophys. Res.*, *78*, 1883.

Chapter 2. Approximations Appropriate for Body-Wave Seismograms

2-1 Introduction

In Chapter 1 we demonstrate how seismic velocity models can be further constrained by including waveform data with travel times and apparent velocity information. Our final model, K8, was derived after a tedious and costly trial and error inversion method. Qualitative arguments are presented to explain those features of the model required by the data. The difficulty of finding one velocity model that satisfied the data is implicitly used as an argument that the model was unique. An automated procedure to invert body wave seismograms would be very useful. We could then test different hypotheses very quickly and the questions concerning resolvability and uniqueness could be then answered more succinctly.

To invert body-wave seismograms we require an efficient computational technique for the generation of theoretical seismograms and their derivatives with respect to velocity model parameters. In recent years, there have been several techniques proposed to quickly and accurately model seismograms in vertically heterogeneous media. Of particular interest are the studies by Mellman and Helmberger (1978), Wiggins and Madrid (1974), Wiggins (1976) and Chapman (1976a, b; 1978).

Most approximate methods are high frequency approximations and break down when applied to high velocity gradients, discontinuities, or low velocity zones, where diffraction effects are important. An accurate modeling of these effects is necessary to constrain the velocity structure from observations of body-wave seismograms. For example, because of diffraction, it is difficult, using long-period seismograms, to pick the distance at which the cusp of a travel time curve ends. To infer this information we must model accurately the behavior of later arrivals over a range of distances. As an example, consider a shear velocity model typical of the uppper mantle, model TNA of Grand and Helmberger (1983) in Figure 2.1. At distances between 23° to 27°, a second arrival is observed and is the result of a discontinuous velocity increase at 660 km depth. The second arrival disappears from the travel time curve beyond 27° yet a diffracted arrival remains in the seismograms that decays with distance. Accurate modeling of this phenomenon is necessary to infer the velocity structure near the discontinuity. We encounter a similar difficulty when trying to detect and model low velocity zones. Therefore, we need to improve our approximations so that they will be accurate and applicable to a wide variety of possible earth models.

The simplest approximation to the wave equation that can be used to accurately synthesize seismograms is the WKBJ approximation (Chapman, 1976b; see textbooks by Aki and Richards, 1980; Ben Menahem and Singh, 1981 for review). The method is essentially geometrical ray theory extended to finite frequencies and is well behaved at cusps in the travel time curve where the infinite-frequency theory of optics breaks down. The assumption necessary to use the WKBJ method is that the medium be slowly varying at wavelengths of

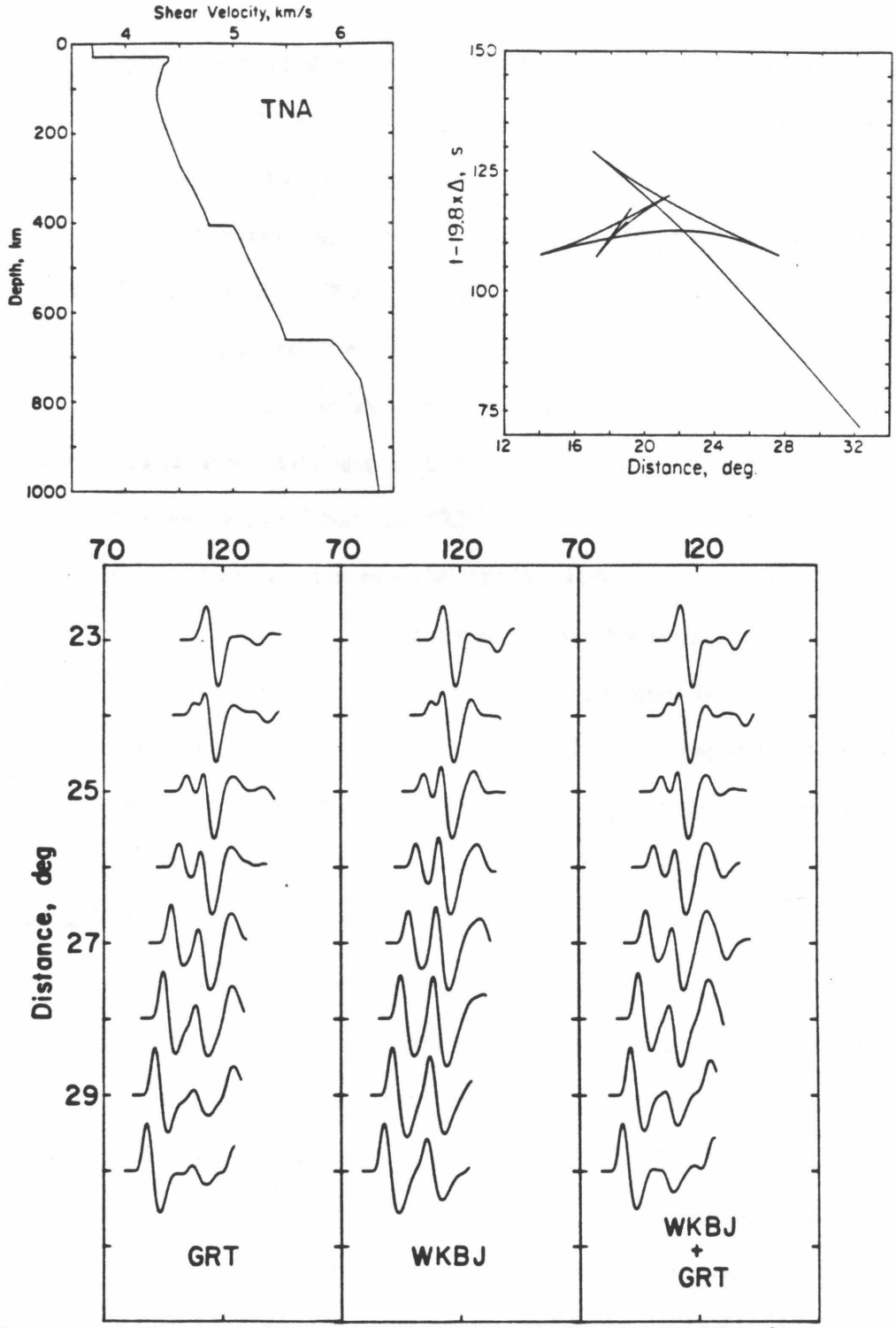

Figure 2.1 S-wave seismograms computed for model TNA (Grand and Helmberger, 1983) for distances ranges 22°–30° using the approximations GRT, WKBJ and WKBJ+GRT. The end of the triplication due to the 660 km discontinuity occurs at about 27°. The amplitude of the second arrival beyond 27° predicted by the WKBJ method is too large compared to GRT. The seismograms computed by WKBJ+GRT agree very well with those computed by GRT.

interest. Typical wavelengths used in modeling long-period body waves are on the order of 50 to 100 km; in the upper 1000 km of the mantle the velocity increases by roughly 40% so this is a valid assumption overall. There appear, however, to be several regions in the upper mantle where large velocity gradients exist (e.g. Fig. 2.1). When the heterogeneity is strong, or when diffraction effects are important, the WKBJ approximation becomes inaccurate. A simple way to improve the approximation is to model high velocity gradients as discontinuous changes in velocity and include reflection and transmission coefficients. However, it is well known that the WKBJ approximation is not uniformly valid in the medium. Problems arise when we try to evaluate displacements at the bottoming depths (turning points) of rays and, thus, for rays that turn near discontinuities, reflection and transmission coefficients cannot be evaluated (Richards, 1976). If these rays contribute significantly to the response at distances of interest, the approximation can be grossly in error. This problem is most serious at the onset of the diffracted regions where accurate modeling is important (see Fig 2.1).

Another, commonly used, method is to approximate the vertical heterogeneity by a stack of plane homogeneous layers. We can expand the exact solution to the elastodynamic equation in a plane layered medium in terms of an infinite sum of generalized rays which have reflected and reverberated within the layers (Helmberger, 1967; Cisternas et al, 1973; Kennett, 1974). The ray expansion allows us to isolate the contribution to the response of waves that have interacted with specific layer boundaries or regions. In homogeneous plane layered media, the displacements in each layer are expressed as sums of plane waves and, thus, the turning point problem is avoided. By summing

enough rays, generalized ray theory (GRT) can be made as accurate as one desires within the limits imposed by a flat layered approximation to radially stratified spherical geometry.

The well known remedy to the turning point problem associated with WKBJ theory is to use a different approximation due to R. E. Langer (see Wasow (1965) for a discussion of Langer's work), that is uniformly valid at and away from the turning point (Chapman, 1973; Richards, 1976). However, the WKBJ approximation is so simple that we would like to retain it when possible. We propose to avoid the turning point problem by the following scheme: we will approximate the medium above or within a discontinuity, transition zone, or low velocity zone by homogeneous layers and use a ray expansion to isolate the energy that has interacted with these regions. With these approximations, there is no turning point problem and the contribution to the seismogram by reflections from the heterogeneous regions can be accurately determined. The part of the solution corresponding to energy that has not interacted with the strongly heterogeneous region (except for transmission) will be computed using the WKBJ approximation.

2-2 Approximations for Body Wave Seismograms

We will illustrate how to compute the approximate SH-wave response of a vertically heterogeneous, isotropic elastic whole space to a point horizontal double couple, i.e. a strike-slip fault with strike, dip, slip, of 0^0, 90^0, 0^0, respectively. We assume a cylindrical coordinate system (r,φ,z) with the $+z$ axis representing depth. The source location (r_s,φ_s,z_s) is taken to be below the receiver location (r_r,φ_r,z_r) and the medium is assumed to be homogeneous

above the source. To be relevant to a spherical symmetry, an earth flattening transformation must be made; an exact transformation exists for SH-waves (Biswas and Knopoff, 1970; Chapman, 1973) and the details are not necessary here.

It is convenient and intuitively useful to approximate the vertically heterogeneous medium as a stack of homogeneous layers with shear velocity, β_i, density, ρ_i, and rigidty μ_i, in the i -th layer. The response can be modeled as an infinite sum of generalized rays that have reflected and reverberated within the layers (Cisternas, et al, 1973; Kennett, 1974). We write the Laplace transform for the tangential component of displacement at the receiver $u(r_r,\varphi_r,z_r,s)$ for our problem as

$$u(r_r,\varphi_r=0,z_r,s) = \frac{s^2 M_o}{4\pi\mu_s}\sqrt{2\pi/r_r s}\cdot\sum_{Rays}^{\infty}\int_0^{i\infty} R_j(p)\frac{p^{3/2}}{\eta_s}e^{-s(pr+\tau(p))}dp \qquad (2.1)$$

In Equation (2.1), p is the ray parameter or the horizontal wave slowness; $R(p)$ is the product of reflection and transmission coefficients along the ray path; $M_o(s)$ is the source spectra; s is the Laplace transform parameter; $\eta_i=(\beta_i^{-2}-p^2)^{1/2}$ is the vertical wave slowness in the i-th layer; and

$$\tau = \sum_{Path}\eta_i Th_i. \qquad (2.2)$$

where Th_i is the thickness of the i -th layer. The azimuthal dependence is simpy $\cos 2\varphi$ and has been omitted by assuming $\varphi=0$.

Equation (2.1) represents an approximation to the exact solution in that an asymptotic expansion is used for the cylindrical wave functions (the Bessel functions). Otherwise it is complete, although the sum is over an infinite number of

generalized rays. A time domain expression for $u(r_r,\varphi_r,z_r,t)$ can be found using the Cagniard - de Hoop method (e.g. Helmberger and Malone, 1975; Wiggins and Helmberger, 1974)

$$u(r,\varphi_r=0,z_r,t) = \sqrt{2/\pi r_r}\,\frac{d^2}{dt^2}\,\frac{M_0}{4\pi^2\mu_s} * \frac{1}{\sqrt{t}} * \sum_{Rays}^{\infty}\left[R_j(p)\,\frac{p^{2/3}}{\eta_s}\,\frac{dp}{dt}\right]_{p=p(t)} \qquad (2.3)$$

where $p(t)$ is the solution to

$$\mathrm{Im}(t) = \mathrm{Im}(pr + \sum_{Path} \eta_i Th_i) = 0. \qquad (2.4)$$

In the above, * denotes convolution.

The ray expansion must, in practice, be truncated. Hron (1971) discusses the systematics for determining which rays are important in a given problem. In modeling body waves for determining structure, it is often sufficient to truncate the ray sum after including only those rays that have undergone, at most, one reflection in the medium. The convergence of the ray sum has been explored by Gilbert and Helmberger (1972), Helmberger (1973), Chapman (1974), and Burdick and Orcutt (1979), among others. They found that for velocity structures typical of those encountered in the earth, the primary ray expansion was adequate. They discussed the situations in which the ray sum does not converge after including only the primary reflections. Burdick and Orcutt (1979) found that the primary ray approximation is not accurate for thin regions of large velocity gradient and that these structures are most easily modeled by a single discontinuous change in velocity. In addition, multiple reflections are required to accurately model waves that have been strongly diffracted. These restrictions are not serious and the primary ray

approximation has been used extensively to model long-period body waves with excellent results.

It is important to recognize the band limited nature of (2.4). At long periods the approximation is inaccurate due to the asymptotic expansion, truncation of the ray sum and, in the similar case of P-SV waves, the earth flattening transformation. These effects are often sufficiently far beyond the recording bandwidth of the instrument used to observe the phenomena that they can be ignored. At short periods the limitation is the assumption of homogeneous layers as an approximation to velocity gradients. The ray sum is a series of discrete arrivals that must be smoothed (i.e. low pass filtered) to be meaningful. To accurately model the response at high frequencies a finely layered model must be assumed. In a typical upper mantle modeling experiment, velocity structures contain between 50 to 100 layers. The computation of seismograms by summing even the primary rays thus becomes quite time consuming. Of course the alternative at high frequencies is to use geometrical optics (Bullen, 1965); however, the frequency band over which this approximation is valid varies enormously depending on the velocity structure and breaks down entirely at caustics and low velocity zones.

Wiggins and Madrid (1974) and Wiggins(1976) use geometrical arguments and experience in modeling seismograms with generalized ray theory to make some high frequency approximations to Equation (2.3) which remain accurate over a broad range in frequencies. They note that the response (2.3) was dominated by rays that had been reflected from within the medium at the critical angle. They devise a method (called disc ray theory) whereby the response could be computed by a superposition of plane waves, each of which had

propagated as a geometrical ray. The technique reproduced the results of geometrical ray theory yet did not break down at caustics.

Chapman (1974; 1976a, b; 1978) derives the same results using the WKBJ approximation. The frequency domain expression for $u(r,\varphi=0,z,t)$ can be written

$$u(r_r,\varphi_r,z_r,\omega) = -\omega^2 M_0(\omega)\cdot\left[\frac{\pi}{\omega}\right]^{1/2}\cdot e^{-i\frac{\pi}{4}}\left\{\int_{-\infty}^{\infty}\frac{p^{3/2}}{4\pi^2(2r\mu_s\eta_s\mu_r\eta_r)^{1/2}}exp(-i\omega\theta)dp\right\} \qquad (2.5)$$

where

$$\theta(p)=pr+\tau(p)=pr+\int_{z_r}^{z_p}\eta(\zeta)d\zeta+\int_{z_s}^{z_p}\eta(\zeta)d\zeta \qquad (2.6)$$

and z_p is the turning point of the ray with ray parameter p, $p=1/\beta(z_p)$. Performing the inverse Fourier transform of (2.5) we have

$$u(r_r,\varphi_r,z_r,t)=\frac{d^2}{dt^2}M_0(t) * \frac{1}{\sqrt{t}} * \qquad (2.7)$$

$$\int_{-\infty}^{\infty}\frac{p^{3/2}}{4\pi^2(2r\mu_s\eta_s\mu_r\eta_r)}\delta(t-\theta(p))dp$$

At a given time, t, the function $\theta(p)$ may have several roots. Denoting these roots as p_m we integrate (2.7) to obtain

$$u(r,\varphi,z,t)=\frac{d^2}{dt^2}M_0(t) * \frac{1}{\sqrt{t}} * \sum_{p_m(t)}\left\{\frac{p^{3/2}}{4\pi^2(2r\mu_s\eta_s\mu_r\eta_r)^{1/2}}\frac{1}{\left|\frac{d\theta}{dp}\right|}\right\} \qquad (2.8)$$

Equations (2.5), (2.6), (2.7), and (2.8) can be easily interpreted as in Wiggins (1976). At a given distance r_0, a direct ray arrives with ray parameter p_0. The

travel time of this ray is given by $t_o = p_o r_o + \tau(p_o)$. At a nearby distance r_1, the direct ray has ray parameter, p_1. If we imagine a plane wavefront perpendicular to the ray paths, the plane wave associated with p_o will arrive at r_o at time t_o. The wavefront associated with p_1 will arrive at r_o at approximately $t = \theta(p_1) = p_1 r_o + \tau(p_1)$. The superposition of all these plane wavefronts is implied by the integral in Equation (2.8) and approximates the response. The method is essentially geometrical optics but the singularities encountered in optics at the cusps of the travel time curves are integrated and the corresponding amplitudes remain finite and accurate.

The above approximation breaks down when either the source or the receiver is at the turning point of a ray that contributes significantly to the response. This problem will become significant if we attempt to fit boundary conditions near the turning point of a ray. As an example we may wish to model a reflection from a discontinuity using the WKBJ approximation. A ray expansion similar to (2.2) is possible and valid as long as no turning rays that contribute to the response bottom near the discontinuity. But $u(r,\varphi,z,t)$ will not be accurate for distances at which the direct ray bottoms near a discontinuity and reflection and transmission coefficients will not be valid. At distances where these geometrical rays are significant the response cannot be computed. As another example we may wish to compute seismograms at distances where the rays of interest leave the source almost horizontally.

The frequency band of the WKBJ response is also limited by the velocity structure. For regions of high velocity gradient or for a discontinuity the long period part of (2.20) can be grossly in error. This is a serious limitation in applying the WKBJ approximation to the modeling of long-period body waves in

the upper mantle. In these studies we are often concerned with velocity structures that contain essentially discontinuities compared to the wavelengths of interest. We would like to modify the approximation to give accurate results in these situations yet remain as easy to compute as (2.8).

The work of Wiggins suggests how this might be done. The p integral in (2.7) is the sum of all turning rays in the medium and thus can be likened to the sum of primary rays in Equation (2.3) when the layer thicknesses become small. If we wish to consider only rays that have interacted with a certain depth range say $z_1 \le z \le z_2$ we simply confine the integral to $1/v(z_1) \ge p \ge 1/v(z_2)$. Now consider a discontinuous velocity increase at $z = z_d$ (Fig. 2.1). We compute the response from above and below the discontinuity by (2.9) using

$$u(r_r, \varphi_r = 0, z_r, t) = \frac{d^2}{dt^2} M_o(t) * \frac{1}{\sqrt{t}} * \left\{ \int_0^{1/v(z_d^+)} \frac{T(p) p^{3/2}}{4\pi^2 (2r \mu_s \eta_s \mu_r \eta_r)^{1/2}} \delta(t - \Theta(p)) dp \right.$$

$$\left. + \int_{1/v(z_d^-)}^{1/v_s} \frac{p^{3/2}}{4\pi^2 (2r \mu_s \eta_s \mu_r \eta_r)^{1/2}} \delta(t - \Theta(p)) dp \right. \tag{2.9}$$

where the function $T(p)$ accounts for the transmission through the discontinuity. The contribution to the response due to energy that has reflected from the discontinuity at z_d is computed with Equation (2.4) after approximating the velocity structure with a layered model. The turning point problem is avoided by using generalized ray theory to describe the interaction with the discontinuity. For rays that bottom immediately below the discontinuity we note that the function $T(p)$ behaves as

$$T(p) = \frac{\mu_+ \mu_- \eta_+ \eta_-}{(\mu_+ \eta_+)^2 + (\mu_- \eta_-)^2} \tag{2.10}$$

where the subscripts (+) and (−) indicate the values above and below the discontinuity respectively. We see that because η_+ is small for these rays, their contribution to the response will be small. These ideas can be easily extended to the modeling of more complex structure with low velocity zones and several discontinuities.

2-3 Numerical Examples

We now present several numerical examples to explore the accuracy of the technique. Approximate seismograms will be compared to seismograms computed by generalized ray theory including only the primary reflections. In Figure 2.1 we compare synthetics for a realistic upper mantle shear wave velocity model. There is a cusp in the travel time curve at around 27° and later arrivals become diffracted at distances beyond. The generalized ray theory solution using only primary rays has been shown by Burdick and Orcutt (1978) to be accurate for some distance beyond the position of the cusp. In the WKBJ calculation, we modeled the discontinuity by a thin high gradient transition zone. Note that at the nearer distances, the two calculations compare quite well but at and beyond the cusp in the travel time curve, the WKBJ response cannot accurately predict the amplitude of the second arrival.

We next illustrate two simple examples of seismograms using the WKBJ approximation, Equation (2.8), alone in order to review the computational procedures involved. The direct calculation of (2.8) presents some minor numerical difficulty. The quantity $(\partial\Theta/\partial p)^{-1}$ is singular at the arrival of each geometric ray. The singularity is integrable and, for a band limited input pulse, an accurate seismogram can be computed provided proper care is taken. Dey-Sarkar

and Chapman (1978) and Chapman (1978) provide adequate practical details concerning the filtering and sampling of Equation (2.8).

Our first example deals with a simple turning ray from a linear gradient. Assuming $d^2/dt^2\, M_o(t) = 1$, $u(t) = u(r,\varphi = 0, z, t)$ will be the integrated response to a step function dislocation. Figure 2.2 illustrates the computational steps necessary to generate a theoretical seismogram. On the right hand side is the model, plotted as inverse velocity, or alternatively the parameter, p, of the ray that bottoms at depth z. The velocity varies linearly from 3.61 km/sec at the surface to 8.06 km/sec at a depth of 1000 km. Starting at $p = 1/3.61$ sec/km and decrementing, we compute the integral

$$\tau = \int_{z_s}^{z_p} \eta\, dz + \int_{z_r}^{z_p} \eta\, dz \qquad (2.11)$$

We also evaulate the coefficients

$$\frac{p^{3/2}}{4\pi^2} (2\eta_r \eta_s \mu_r \mu_s)^{-1/2}$$

The plot of τ vs. p is shown in the center of Figure 2.2. Up to this point the quantities computed are relevent to all distances. On the left hand side we have computed the quantity $\Theta(p) = pr + \tau(p)$ for a distance of 20°. This relation maps the functions of p into the time domain for $\Theta(p) = t$. Computing the slope of the $\Theta(p)$ curve for each branch, we obtain the time-domain seismogram, $\bar{u}(t)$, shown in the lower left hand side of Figure 2.2. Convolution of this function with $1/\sqrt{t}$ yields the step function response $u(t)$ shown in the lower right.

Figure 2.3 gives an example of a seismogram from a model in which there is an increase in velocity at depth. In this case there are extrema in $\Theta(p)$ curve,

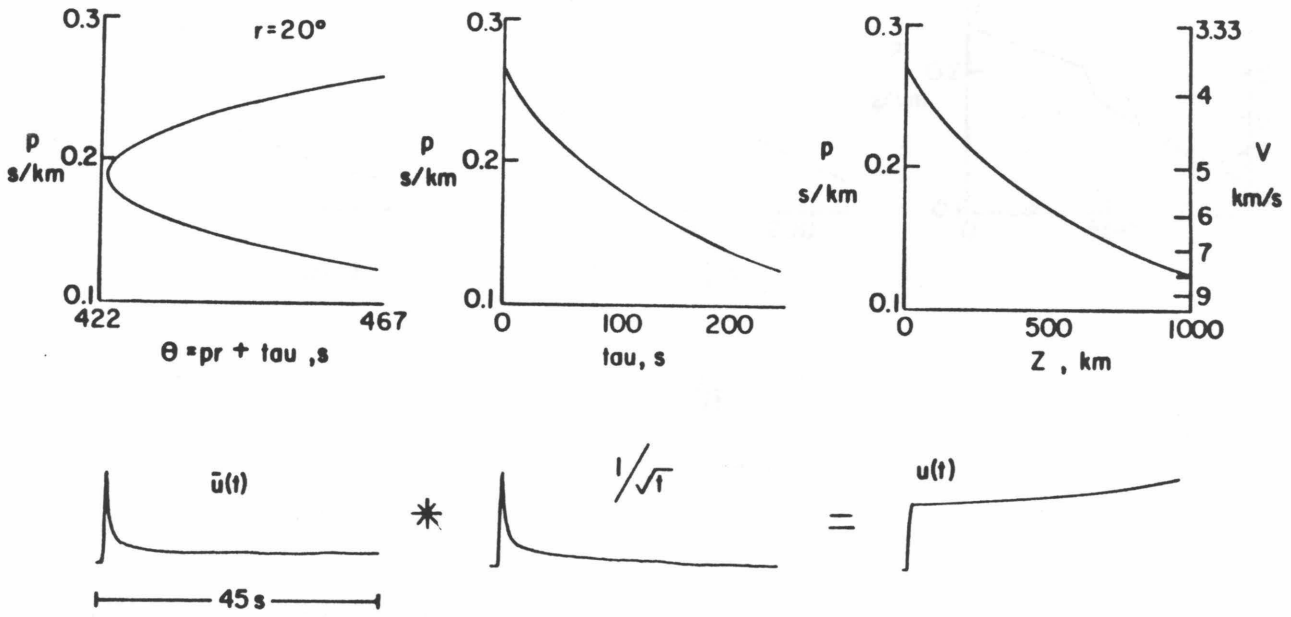

Figure 2.2 An example of the computational steps in computing the integrated step function response from WKBJ approximation. Upper right is a plot of $1/v(z)$ or equivalently the ray parameter p vs the bottoming depth of the ray. Upper center is the function $\tau(p)$, and upper left is a plot of $\theta=pr+\tau$. For each $\theta=t$ we simply compute $1/(d\theta/dp)$, thus there are two branches at each time point shown. Note singularity at the time t_o. Convolution of resulting time series (lower left) with $1/\sqrt{t}$ gives step function response.

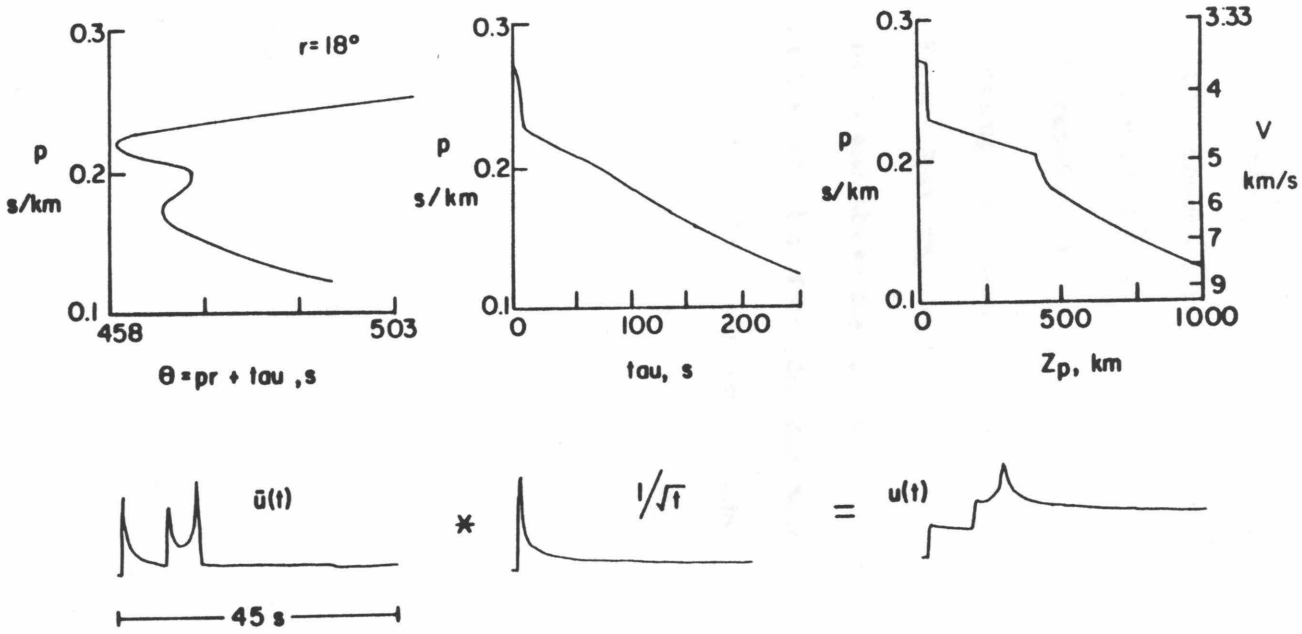

Figure 2.3 Another example of computation of a step function response using the WKBJ approximation. In this case there is a high velocity gradient around 400 km. Note three extrema in the $t(p)$ curve; these correspond to three geometrical arrivals from the velocity structure.

two relative minima and a relative maximum. These correspond to three direct geometrical arrivals from the velocity structure: the familiar triplication due to an increase in the velocity gradient at depth. Note that two of the arrivals have the same phase after convolution with $1/\sqrt{t}$, i.e. both are step functions; the third arrival is distorted (actually phase shifted by $\pi/2$). These features are consistent with the results predicted by a more accurate theory.

For a third example we replace the velocity increase in Figure 2.3 with a discontinuity (Figure 2.4). The WKBJ approximation is used to compute the response from below and above the discontinuity and generalized ray theory is used to compute the reflection from the discontinuity. In this case the range of p used to compute (2.9) excludes those values of p such that $1/v(z_d^-)>p>1/v(z_d^+)$, thus the gap in the $\tau(p)$ and $\Theta(p)$ curves. Some of excluded values of p reappear in the contribution to the solution by the generalized ray used to model the reflection from the discontinuity. The response is in many respects, very similar to the one in Figure 2.3.

A profile of seismograms from a velocity structure including a discontinuity is given in Figure 2.5. The response including long-period instrument, source time function, and attenuation are shown along with the integrated step function responses. At 12° the reflection from the discontinuity is pre-critical, and at 24° the reflection is post-critical. At all ranges the agreement between the generalized ray synthetics and the combination generalized ray - WKBJ synthetics (WKBJ+GRT) are quite good yet the latter required about 1/20 of the computation time.

As a final example we model a velocity structure that includes a low velocity zone (Figure 2.6). In this case, generalized ray theory must be used to account

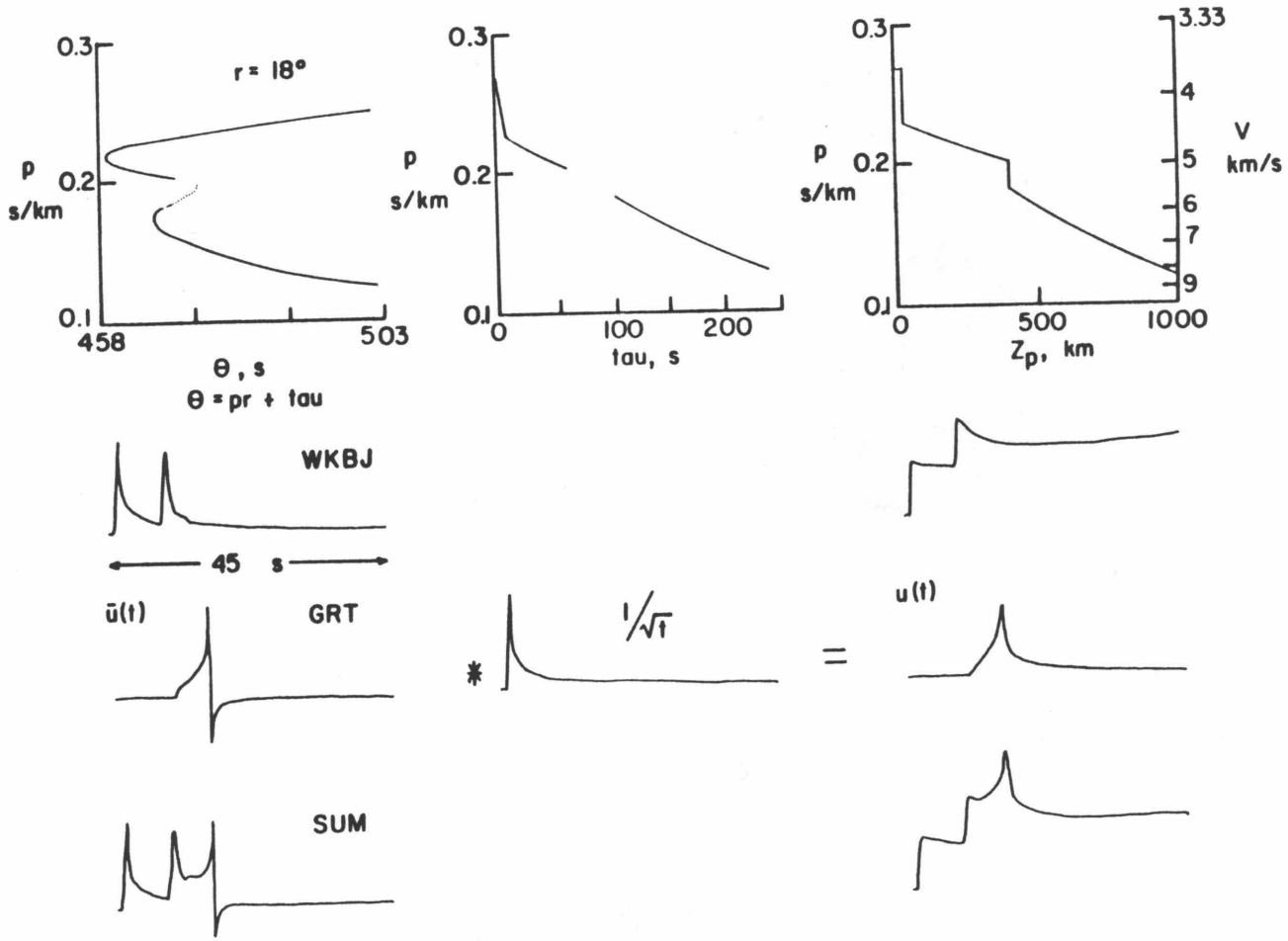

Figure 2.4 Example of computation of step function response using WKBJ approximation and generalized ray theory. The high velocity gradient in Figure 2.2 has been replaced with a discontinuous velocity increase. The response from the discontinuity is computed using generalized ray theory. The dotted portion in $\theta(p)$ curve ar from those values of real p curve which are included in the computation of the generalized ray.

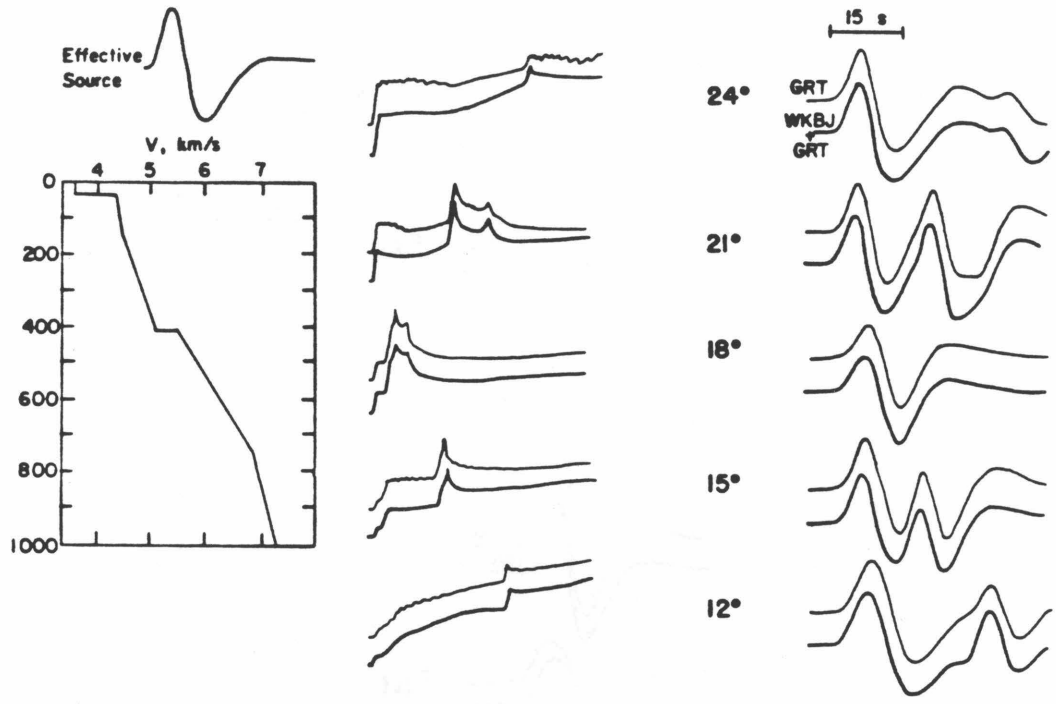

Figure 2.5 Comparison of full generalized ray theory and WKBJ+GRT for a simplified upper mantle model including a Moho and discontinuity at 400-km depth.

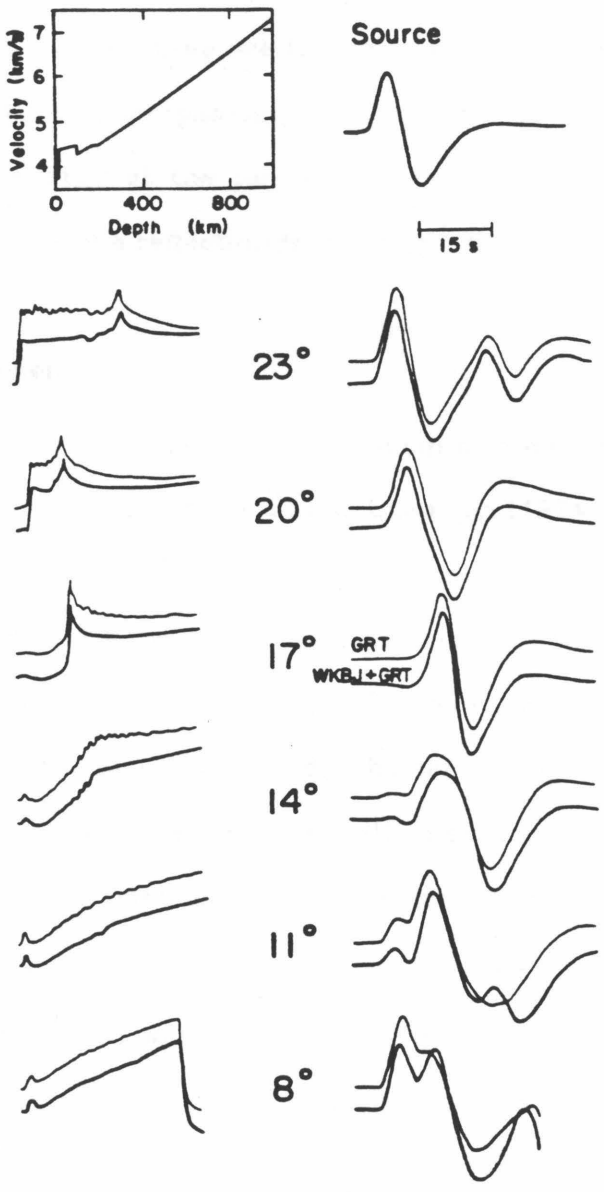

Figure 2.6 Test of WKBJ+GRT for a model including a low velocity zone. Rays were used to model the upper 200 km including energy which has diffracted in the lid and tunnelled through the lid.

for both the diffracted energy within the high velocity lid and energy that has tunnelled through the lid and interacted with the velocity gradient below (Mellman and Helmberger, 1974). The primary ray approximation may not be sufficiently accurate at very long periods, however multiples can be added as needed. In Figure 2.6 we see that the agreement between WKBJ+GRT and GRT is fairly good; the discrepancies that occur are due to inadaquate modeling of the tunnelled energy at the nearer ranges. The WKBJ approximation apparently gives too large of a reflection from the gradient below the low velocity zone.

2-4 Discussion

The ideas presented here may seem obvious and, indeed, they are implicit in the papers of Wiggins (1976) and Chapman (1974; 1976b). However we know of no numerical checks of the accuracy and applicability of these techniques. As seen in Figure 2.1 the WKBJ technique works quite well for modeling long period body waves at some distances. The most annoying breakdown of the WKBJ method was the inability to model the decay in amplitude off the end of the triplication cusps. A more accurate method ensures that we are not modeling these phenomena with some artifacts of the computational method.

The method presented here can be used to model a wide variety of velocity structures. There will still be some problems in modeling high velocity gradients of finite thickness where both the WKBJ approximation and the primary ray expansion are invalid. In some cases judicious selection of multiples in the generalized ray expansion may be all that is necessary to correct the solution. New methods have recently been given to handle such situations using the Langer approximation (Chapman, 1981; Kennett and Illingworth, 1981) and these

will probably prove valuable when sufficient experience has been gained in applications.

The technique presented here is also simple enough that an inverse problem can be posed. Using Equations (2.9) and (2.3) the perturbations in a seismogram due to changes in the velocity structure can easily be evaluated. We can now develop an iterative technique that allows us to take an initial estimate of the velocity structure and compute the perturbations to the model necessary to accurately predict the observed seismograms.

2-5 Conclusions

The computation involved in generating synthetic seismograms using generalized ray theory can be enormously reduced by using a WKBJ approximation to account for those rays that are critically reflected from regions with weak velocity gradients. The generalized ray approach is retained to model discontinuities, high velocity gradients and low velocity zones. The problems associated with turning points in the WKBJ method can thus be avoided.

2-6 References

Aki, K. and P. G. Richards, 1980, *Quantitative Seismology* , W. H. Freeman and Co., New York.

Ben Menahem A. and S. J. Singh, 1981, *Seismic Waves and Sources*, Springer-Verlag, New York.

Biswas, N. N. and Knopoff L. , 1970, Exact earth flattening calculation for Love waves, *Bull. Seism. Soc. Am.*, *60*, 1123-1137.

Bullen, K.E., 1965, *An Introduction to the Theory of Seismology* , Cambridge

University Press.

Burdick, L. J., and J. A. Orcutt, (1979), A comparison of generalized ray and reflectivity methods of waveform synthesis, *Geophys. J. R. astr. Soc. 58*, 261-278.

Cisternas, A., O. Betancourt and A. Leiva, 1973, Body waves in a "real earth", Part I, *Bull. Seis. Soc.. Am.*, *63* , 145-156.

Chapman, C. H., 1973, The earth flattening transformation in body wave theory, *Geophys. J. R. Astr. Soc.*, *35* , 55-70.

Chapman, C. H., 1974, Generalized ray theory for an inhomogenous medium, *Geophys. J. R. Astr. Soc.*, *36*, 673-704.

Chapman, C. H., 1976a, A first motion alternative to geometrical ray theory, *Geophys. Res. Lett.*, *3*, 153-156.

Chapman, C. H., 1976b, Exact and approximate generalized ray theory in vertically inhomogenous media, *Geophys. J. R. Astr. Soc.*, *46* , 201-233.

Chapman, C.H., 1978, A new method for computing synthetic seismograms, *Geophys. J. R. Astr. Soc 54*,, 481-518.

Chapman, C. H. , 1981, Long period corrections to body waves: theory, *Geophys. J. R. Astr. Soc.*, *64* , 321-372.

Dey Sarkar S. K. and Chapman, C. H., 1978, A simple method for the computation of body-wave seismograms, *Bull. Seis. Soc. Am.*, *63*, 145-156.

Gilbert, J.F. and D.V. Helmberger, 1972 Generalized ray theory for a layered sphere, *Geophys. J. R. astr. Soc. 27*, 57-80.

Grand, S. P. and D. V. Helmberger, 1983 Upper mantle shear structure of North America, *Geophys. J. R. Astr. Soc.* (in press).

Helmberger, D.V., 1967, Head waves from the oceanic Mohorovicic discontinuity,

Ph.D. thesis, Univ. Calif., San Diego, La Jolla, Calif.

Helmberger, D.V., 1973, Numerical seismograms of long period body waves from seventeen to forty degrees, *Bull. Seism. Soc. Am.*, *64* , 45-64.

Helmberger, D.V. and S.D. Malone, 1975, Modeling local earthquakes as shear dislocations in a layered halfspace, *J. Geophys. Res.*, *80*, 4881-4885.

Hron, F., 1971, Criteria for selection of phases in synthetic seismograms in layered media, *Bull. Seis. Soc. Am.*, *61*, 765-779.

Kennett, B.L.N., 1974, Reflections, rays and reverberations, *Bull. seismol. Soc. Am.*, *65*, 1685-1696.

Kennett, B. L. N. and M. R. Illingworth, 1981, Seismic waves in a stratified half space-III, piecewise smooth models, *Geophys. J. R. Astr. Soc.*, *66*, , 633-675.

Mellman, G. R. and D. V. Helmberger, 1974, High frequency attenuation by a thin high-velocity layer, *Bull. Seis. Soc. Am.*, *64*, 1383-1388.

Mellman, G. R. and D. V. Helmberger, 1978, A modified first motion approximation for synthesis of body wave seismograms, *Geophys. J. R. Astr. Soc.*, *54* , 129-140.

Richards, P. G., 1976, On the adequacy of plane-wave reflection-transmission coefficients in the analysis of seismic body waves, *Bull. Seis. Soc. Am.*, *66*, 701-718.

Wasow, W., 1965, Asymptotic Expansions for Ordinary Differential Equations, *Interscience Publisher*, New York.

Wiggins, R. A., 1976, Body wave amplitude calculations II, *Geophys. J. R. Astr. Soc.*, *46*, 1-10.

Wiggins R.A. and D.V. Helmberger, 1974, Synthetic seismogram computation by

expansion in generalized rays, *Geophys. J. R. Astr. Soc. 37*, 73-90.

Wiggins, R. A. and J. A. Madrid, 1974, Body wave amplitude calculations, *Geophys. J. R. Astr. Soc., 37*, 423-433.

Chapter 3. A Method for the Inversion of Body-Wave Seismograms for Earth Structure

3-1 Introduction

Seismology has advanced to where the recorded waveforms in addition to travel times, and apparent velocities, $(dT/d\Delta)$, must be considered as data in order to derive satisfactory models of the earth's velocity structure. During the past decade, there has been widespread use of synthetic seismograms to constrain velocity models. In many of these studies, however, the agreement of theoretical and observed seismograms is achieved through laborious trial and error perturbation of the velocity structure. Discussion of uniqueness and resolution are largely based on qualitative arguments. There have been few attempts to quantify the quality of a comparison between observations and synthetics.

Recently, several authors have formalized the inversion process in order to examine the resolving power of waveform data (Mellman, 1980; Chapman and Orcutt, 1980). These authors were successful in applying an inversion technique to the interpretation of oceanic refraction data. With a formal inversion procedure, different constraints on the velocity structure can be introduced and the uniqueness of an interpretation can be evaluated. Furthermore an analysis of the resolution of a set of data can be performed using the formalism introduced to geophysics by Backus and Gilbert (1968). Although the problem of

waveform inversion is non-linear, resolution studies assuming linearity can still be very useful.

In the following we will outline a technique for the inverison of seismic body waves for velocity structure. The approximations derived in Chapter 2 will be used to model the seismograms and thus the technique will be applicable to a wide range of velocity structures.

3-2 Inversion Procedure

Given a data set consisting of observed seismograms and travel times, we propose to derive a velocity model from a reasonable, initial estimate of the velocity structure. The final model will be required to fit the data in some well defined sense.

Before proceding, we must clearly define how we will treat observed seismograms as data. In many seismological experiments designed to investigate velocity structure, the absolute amplitudes are not well enough understood to be useful for constraining the velocity structure. However, seismograms consisting of multiple arrivals from a major triplication are remarkably consistent between different seismic sources and receivers. The relative amplitudes of the various arrivals contain information concerning the velocity structure in addition to that provided by travel times and apparent velocity data. We will, therefore, treat the waveshapes as data and use a normalization scheme from Mellman (1980) to remove the absolute amplitudes. When reliable, the absolute amplitude data can easily be incorporated.

We define the j^{th} observed seismogram $o_j(t)$ and the corresponding theoretical seismogram computed for some starting model as $s_j(t)$. The

waveforms of $o_j(t)$ and $s_j(t)$, $\hat{o}_j(t)$ and $\hat{s}_j(t)$ are defined as:

$$\hat{o}_j(t) = \frac{o_j(t)}{\left[\int_{W_j} o_j^2(t)dt\right]^{1/2}} \tag{3.1}$$

$$\hat{s}_j(t) = \frac{s_j(t)}{\left[\int_{W_j} s_j^2(t)dt\right]^{1/2}} \tag{3.2}$$

The denominators in (3.1) and (3.2) are proportional to the RMS power in some time window W_j. There is an obvious problem with this normalization. Noise present in the data, including random background noise, arrivals not included in the modeling process, and errors in the source time function, will cause the normalization of the observed seismograms to be misestimated. The time window W_j must be carefully chosen to include similar arrivals in both the starting model and the observed seismograms and yet to exclude as much noise as possible. For instance, given a seismogram containing two arrivals widely separated in time, we may choose to normalize over a window that includes the first arrival only. Including both arrivals would also include noise from scattered energy, etc., and the normalization term would likely be overestimated. We will also try to account for possible errors in the normalization in the inversion procedure.

Absolute travel times can be strongly affected by local velocity structure and source mislocation. It is necessary, then, to either remove the travel times from the waveform inversion or be able to correct the observed travel time for possible errors in source location and for insufficient knowledge of the shallowest velocity structure. In the case of, say, long-period S-waves propagating in the upper mantle, errors in source-receiver distance of as little as 25 km implies

travel time differences of 3 to 4 sec while the resolvable waveform differences are negligible.

We then define $e'_j(t)$, the waveform error, in some time window T_j as

$$e'_j(t) = \hat{o}_j(t-\tau_j) - \hat{s}_j(t) \tag{3.3}$$

where τ_j is a time correction. τ_j can be determined by assuming the travel time vs distance curve is known or by maximizing the quantity $\varphi_{os}(t)$,

$$\varphi_{os}(t) = \int_{W_j} \hat{o}_j(t+\tau)\hat{s}_j(\tau)d\tau \tag{3.4}$$

is maximized. We note that the time window, T_j in Equation (3.4), is the interval over which we desire to fit the data and may be longer than, or equal to, W_j.

For N observations, the best fitting model is the one that minimizes the residual $(\mathbf{r}',\mathbf{r}')$, where

$$(\mathbf{r}',\mathbf{r}') = \sum_{j=1}^{N} \int_{T_j} e'^2_j(t)dt \tag{3.5}$$

We assume that the error $e'_j(t)$ can be reduced by perturbations in the velocity structure and corrections to the normalization of $\hat{o}_j(t)$. Assuming linearity about the starting model, Equation (3.3) becomes

$$e'_j(t) = \frac{\partial \hat{s}_j(t)}{\partial m'_i}\delta m'_i + b_j \hat{o}_j(t-\tau_j) \tag{3.6}$$

where m'_j is some parameter of the velocity structure, and b_j is a constant correction term for each observed seismogram. From our definition of $\hat{s}_j(t)$ we note that

$$\partial \hat{s}_j(t) / \partial m'_i = \hat{s}'_{ji}(t) - \hat{s}_j(t) \int_{W_j} \hat{s}_j(t) \hat{s}'_{ji}(t) dt \tag{3.7}$$

where

$$\hat{s}'_{ji}(t) = \frac{\partial s_j / \partial m'_i}{\left[\int_{W_j} s_j^2(t) dt \right]^{1/2}} \tag{3.8}$$

The function $e'_j(t)$ is a discrete time series sampled at interval Δt_j. Each seismogram consists of $L_j = T_j / \Delta t_j$ samples and $(\mathbf{r}', \mathbf{r}')$ is the inner product of a vector of length $K = \sum_N L_j$. The problem can then be expressed as

$$\mathbf{r}' = \mathbf{A}' \delta \mathbf{m}' \tag{3.9}$$

where $\delta \mathbf{m}'$ is now a vector of length , say M, containing the model perturbations and the corrections to the normalization of the observed seismograms. $\mathbf{A}'$ in Equation (3.9) is a matrix with elements given by Equation (3.6) and the correspondence between the time points in $\mathbf{r}'$ and $e_j(t)$. At this point we can include additional travel time data by appending the residual vector $\mathbf{r}'$ with the travel time errors and including the appropriate derivatives in $\mathbf{A}'$.

The problem of determining $\delta \mathbf{m}'$ from Equation (3.9) is the generalized inverse problem which has received exhaustive treatment in the geophysical literature in the past two decades (e.g. Backus and Gilbert, 1967; 1968; 1970). We will follow quite closely the development in Wiggins (1972).

Because we are treating each sample of the seismogram as a data point, there will normally be many more data than model parameters and the problem is formally an overdetermined one. In general, however, not all of the

parameters, $\mathbf{m}'$ can be resolved from (3.9) uniquely; only linear combinations of the δm_i can be determined. We, therefore choose to solve (3.9) such that some linear combination of $(\mathbf{r}',\mathbf{r}')$ and $(\delta\mathbf{m}',\delta\mathbf{m}')$ is minimized.

The inner product $(\delta\mathbf{m}',\delta\mathbf{m}')$ obviously depends on the dimensions of the $\delta m'_j$, and it is desirable to remove this dependence by minimizing $(\delta\mathbf{m}',\mathbf{W}\delta\mathbf{m}')$ where $\mathbf{W}$ is the parameter covariance matrix. In the simplest case $\mathbf{W}$ is an $M\times M$ diagonal matrix. We also use $\mathbf{W}$ to control the tradeoff between the model perturbations and the normalization corrections.

We also recognize that observational errors may cause some elements of $\mathbf{r}'$ to be less reliable than others. We introduce the covariance matrix $\mathbf{C}$, $C_{ij} = cov(\Delta r'_i, \Delta r'_j)$ where the $\Delta r'_i$ are the uncertainties in r'_i. We now weight the observations in such a way as to minimize $(\mathbf{r}',\mathbf{C}\mathbf{r}')$.

The problem of minimizing a linear combination of $(r',\mathbf{C}r')$ and $(\delta\mathbf{m}',\mathbf{W}\delta\mathbf{m}')$ can be expressed by rewriting (3.9),

$$\mathbf{r} = \mathbf{A}\delta\mathbf{m} \tag{3.10}$$

where $\mathbf{A} = \mathbf{C}^{-1/2}\mathbf{A}'\mathbf{W}^{-1/2}$, $\mathbf{r} = \mathbf{C}^{-1/2}\mathbf{r}'$ and $\delta\mathbf{m} = \mathbf{W}^{-1/2}\delta\mathbf{m}'$.

The covariance matrix $\mathbf{C}$ is diagonal if the observations are independent. For our waveform data, where each sample of the observed seismogram represents an observation, this is not the case. Each observation, and, hence, its error, is related to adjacent ones through the smoothing effects of attenuation, the instrument and the source time function. In this sense, the proper $\mathbf{C}^{-1/2}$ may be considered as a deconvolution operator. We avoid the problems associated with deconvolution and simply assume that the errors at each time point are uncorrelated. Normally the same observational error is assumed to be

appropriate for an entire seismogram, however, a tapered weighting function may be useful in some cases. Because we are fitting some smoothed data, the result of these assumptions will be smoother model perturbations.

It is convenient to decompose **A** into its eigenvalue spectrum (Lanczos, 1961; Wiggins, 1972)

$$\mathbf{A} = \mathbf{U}\Lambda\mathbf{V}^T \tag{3.11}$$

where superscript T denotes transpose. For M parameters and K observations, matrix **A** will have rank R, and **U** and **V** will be $K\times R$ and $M\times R$ matrices, respectively. Λ is an $R\times R$ matrix with elements λ_i. Λ, **U**, and **V** are determined by solving the eigenvalue problems

$$\mathbf{A}\mathbf{A}^T\mathbf{V} = \Lambda\mathbf{V} \tag{3.12}$$

and

$$\mathbf{A}^T\mathbf{A}\mathbf{U} = \Lambda\mathbf{U} \tag{3.13}$$

U and **V** are, thus, composed of orthogonal column vectors denoted as **u** and **v**. Using the singular value decomposition, (3.11),

$$\delta\mathbf{m} = \mathbf{V}\Lambda^{-1}\mathbf{U}^T\mathbf{r} \tag{3.14}$$

is the generalized inverse of (3.10).

The matrix **A** is nearly always almost singular. In other words the eigenvalue matrix Λ contains elements that are negligibly small. It is desirable to suppress these eigenvalues by substituting the matrix Λ^* for Λ such that

$$\lambda^{*-1} = \lambda_i / (\lambda_i^2+\gamma). \tag{3.15}$$

If γ is properly chosen, the large elements of Λ^{*-1} transform to

$$1/\lambda_i^* = \frac{\lambda_i}{\lambda_i^2+\gamma} \approx 1/\lambda_i \tag{3.16}$$

and the small elements behave as

$$1/\lambda_i^* = 0. \tag{3.17}$$

γ is chosen by inspecting the variance of the model perturbations, σ_i:

$$\sigma_i^2 = \sum_M \left[v_{ij}/\lambda_j^*\right]^2 \tag{3.18}$$

We simply adjust γ so that σ_i is smaller than some predetermined value.

The inversion of body-waves for structure is expected to be very non-linear and several (or many) iterations may be necessary before $(\delta\mathbf{m},\delta\mathbf{m})$ and $(\mathbf{r},\mathbf{r})$ are minimized. A resolution analysis of such a procedure may be difficult to perform. Parts of the model that are well resolved in one iteration may be poorly resolved in later steps. This will be particularly true if low velocity zones are introduced. Nevertheless it will be useful to examine the resolution ("averaging kernels") at various stages in the inversion procedure in order to obtain a succinct, if somewhat qualitative, feel for resolvability of the data. The resolution matrix $\mathbf{R}$ is defined as

$$\mathbf{R} = \sum_R \frac{\lambda_i^2}{\lambda_i^2+\gamma} \mathbf{v}_i \mathbf{v}_i^T \tag{3.19}$$

The rows of $\mathbf{R}$ represent the resolution obtainable from the data set given the

data covariance matrix **C** and the desired accuracy for the parameter corrections.

The preceeding discussion is a straightforward application of the generalized inverse theory of Backus and Gilbert (1967;1968;1970) as reviewed by Wiggins (1972). The most difficult task is the computation of **A**. In the next section we will use the approximations derived in Chapter 2 to evaluate the elements of **A**.

3-3 Change in Synthetic Seismograms Induced by a Perturbation in the Velocity Structure

We now demonstrate how to approximate the change in a synthetic seismogram $s_i(t,\mathbf{m})$ due to some model perturbation $\delta\mathbf{m}$. Expanding $s_i(t,\mathbf{m}+\delta\mathbf{m})$ about the starting model $\mathbf{m}_o$, we write

$$s_i(t,\mathbf{m}_o+\delta\mathbf{m}) = s_i(t,\mathbf{m})+\frac{\partial s_i}{\partial m_j}\delta\mathbf{m}_j+O(\delta m_j^2). \tag{3.20}$$

In the following we will neglect the terms of order $O(\delta m_j^2)$ and assume linearity about the initial model.

In Chapter 2 we derive some approximations that allow us to effectively compute $s_i(t,\mathbf{m})$ for a wide variety of velocity structures. Specifically,

$$s_i(t,\mathbf{m}) = u^{WKB}(t)+u^{GR}(t). \tag{3.21}$$

The WKBJ seismogram, $u^{WKB}(t)$, is the contribution to $s_i(t,\mathbf{m})$ from those regions of the velocity structure for which the WKBJ approximation is valid; $u^{GR}(t)$, the generalized ray seismogram, corrects the synthetic for long-period

propagation effects that are not accurately modeled by the WKBJ approximation. $u^{GR}(t)$ is computed using a generalized ray expansion to model those waves that have interacted with a particular region of the velocity model.

3-3.1 The Change in the WKBJ Seismogram Induced by a Perturbation in the Velocity Structure

Following Equation (2.5), the frequency domain expression for $u^{WKB}(\omega)$ is

$$u^{WKB}(\omega) = -\omega^2 S_0(\omega)\cdot\sqrt{\frac{\pi}{\omega}}e^{-i\pi/4} \tag{3.22}$$

$$\cdot\left\{\int_{p_1}^{p_2}+\int_{p_3}^{p_4}+\cdots F_{RS}(p)R(p)e^{-i\omega(pr+\tau(p))}dp\right\}$$

$S_0(\omega)$ is the effective source function and includes the source time function, attenuation operator and instrument response. (A dislocation source is explicitly assumed, hence the ω^2 factor). $F_{RS}(p)$ includes the source radiation pattern and receiver functions. $R(p)$ is the product of the transmission coefficients, often approximated by unity. The function $\tau(p)$ is defined by

$$\tau(p) = \int_0^{z_s}\eta dz + 2\int_{z_s}^{z_p}\eta dz \tag{3.23}$$

where $\eta = (1/v^2(z) - p^2)$, z_s is the source depth and z_p is the depth at which $1/v(z) = p$.

The integral in (3.23) is over real p; the intervals $p_1<p<p_2$, etc., can be mapped directly into the velocity-depth function $v(z)$ by the transformation $p = 1/v(z)$. In the subsuquent discussion we will consider the first integral in

(3.22) over the interval (p_1, p_2).

It is straightforward to differentiate (3.22) with respect to some velocity parameter, say, v_j. $u^{WKB}(\omega)$ depends on the velocity structure through the functions $R(p)$ and $\tau(p)$.

$$\partial u^{WKB}(\omega)/\partial v_j = -\omega^2 S_o(\omega)\sqrt{\frac{\pi}{\omega}}e^{-i\pi/4} \tag{3.24}$$

$$\cdot\left\{\int_{p_1}^{p_2} F_{RS}(p)\frac{\partial R(p)}{\partial v_j}e^{-i\omega(pr+\tau(p))}dp\right.$$

$$\left.-i\omega\int_{p_1}^{p_2} F_{RS}(p)R(p)\frac{\partial \tau(p)}{\partial v_j}e^{-i\omega(pr+\tau(p))}dp\right\}$$

The quantities $\partial R/\partial v_j$ and $\partial \tau/\partial v_j$ will depend on the model parameterization but in general wil be functions of p only. We obtain a time domain expression, $\partial u^{WKB}(t)/\partial v_j$, by the method developed by Chapman (1978) and reviewed in Chapter 2. Essentially the Fourier transform from the frequency domain to the time domain is performed prior to evaluation of the p-integral. The resulting contribution to $\partial u^{WKB}(t)/\partial v_j$ for $p_2 > p > p_1$ is

$$\frac{\partial u^{WKB}(t)}{\partial v_j} = \frac{1}{\sqrt{t}} * \left\{\frac{d^2 S}{dt^2} * u'_1(t) + \frac{d^3 S}{dt^3} * u'_2(t)\right\} \tag{3.25}$$

where

$$u'_1(t),\ u'_2(t) = 0 \qquad p < p_1 \tag{3.26}$$

$$u'_1(t) = \sum_m \left[F_{RS}(p)\frac{\partial R(p)}{\partial v_j}\frac{1}{|\partial\Theta/\partial p|}\right]_{p=p_{m(t)}} \qquad p_1 < p < p_2 \tag{3.27}$$

$$u'_2(t) = \sum_m \left[F_{RS}(p) R(p) \frac{\partial \tau(p)}{\partial v_j} \frac{1}{|\partial \Theta / \partial p|} \right]_{p=p_m(t)} \quad p_1 < p < p_2 \tag{3.28}$$

$$u'_1(t),\ u'_2(t) = 0 \quad p > p_2 \ . \tag{3.29}$$

$p_m(t)$ is the m^{th} root of $\Theta = pr + \tau$ at $\Theta = t$.

Equation (3.25) is a very easy function to evaluate. Most of the quantities required in computing u'_1 and u'_2 are also necessary for computing the WKBJ seismogram $u^{WKB}(t)$; obtaining $\partial u^{WKB}(t) / \partial v_j$ requires little effort beyond the calculation of the synthetic seismogram. Examples of expressions for $\partial R(p) / \partial v_j$ and $\partial \tau(p) / \partial v_j$ are given in the Appendix.

3-3.2 The Change in the Generalized Ray Seismogram Induced by a Perturbation in the Velocity Structure

Following Equation (2.1), the expression for $u^{GR}(s)$, where s is the Laplace transform parameter is

$$u^{GR}(s) = -s^2 S_0(s) \cdot \sqrt{\frac{\pi}{s}} \sum_{RAYS} \mathrm{Im} \int_0^{i\infty} F_{RS}(p) R(p) e^{s(pr + \tau(p))} dp. \tag{3.30}$$

The function $S_0(s)$ and $F_{RS}(p)$ are the same as in Equation (3.23) with $\omega = -is$. $R(p)$ now includes the product of all transmission and reflection coefficients and $\tau(p)$ is now defined by

$$\tau(p) = \sum_{PATH} \eta_i Th_i \tag{3.31}$$

where Th_i is the layer thickness and the sum is over layers along the ray path. The computation of $\partial u^{GR}(t) / \partial v_j$ is similar to that of $\partial u^{WKB}(t) / \partial v_j$.

Differentiating (3.30) with respect to v_j, we obtain

$$\frac{\partial u^{GR}(s)}{\partial v_j} = s^2 S_o \cdot \sqrt{\frac{\pi}{s}} \tag{3.32}$$

$$\cdot \sum_{RAYS} \left\{ \mathrm{Im} \int_0^{i\infty} F_{RS}(p) \frac{\partial R(p)}{\partial v_j} e^{-s(pr+\tau(p))} dp \right.$$

$$\left. -s \ \mathrm{Im} \int_0^{i\infty} F_{RS}(p) R(p) \frac{\partial \tau(p)}{\partial v_j} e^{-s(pr+\tau(p))} dp \right.$$

The terms $\partial R(p)/\partial v_j$ and $\partial \tau(p)/\partial v_j$ are functions of p only. The resulting time domain expressions can be obtained from (3.32) using the Cagniard-de Hoop method,

$$\frac{\partial u^{GR}(t)}{\partial v_j} = \frac{H(t)}{\sqrt{t}} * \left\{ \frac{d^2 S(t)}{dt^2} * \sum_{RAYS} \mathrm{Im} \left[F_{RS}(p) \frac{\partial R(p)}{\partial v_j} \frac{dp}{dt} \right]_{p=p(t)} \right. \tag{3.33}$$

$$\left. - \frac{d^3 S(t)}{dt^3} * \sum_{RAYS} \mathrm{Im} \left[F_{RS}(p) R(p) \frac{\partial \tau(p)}{\partial v_j} \frac{dp}{dt} \right]_{p=p(t)} \right.$$

where $p = p(t)$ is the Cagniard path defined by $Im(t) = Im(pr+\tau) = 0$. Again, computation of $\partial R(p)/\partial v_j$ and $\partial \tau(p)/\partial v_j$ is efficiently performed during the evaluation of $R(p)$ and $\tau(p)$ for the synthetic seismogram. The time-consuming task of locating the Cagniard contours is done only once. Expressions for $\partial R(p)/\partial v_j$ and $\partial \tau(p)/\partial v_j$ are given in Appendix.

3-3.3 Nonlinearity in $\partial s_i(t)/\partial v_j$

In order to gain some insight into the nonlinear nature of the inversion procedure, we discuss, qualitatively, the behavior of the time series $\partial s_i(t)/\partial v_j$, as approximated by (3.20). We note that if $d^2S_o(t)/dt^2=\delta(t)$ in Equations (3.25) and (3.33), then the $s_i(t)$ is the response of the velocity structure to a step function input.

The error introduced by neglecting higher order terms in (3.18) is primarily in the inability of the linear term to adequately model time shifts due to velocity perturbations. If $s_i(t)$ is a step, say, arriving at t_o, then, using our method to compute $\partial s_i(t)/\partial v_j$, the only way to approximate a time shift is to add or subtract delta function at $t=t_o$. Qualitatively, it can be seen that this is accomplished by our expressions (3.25) and (3.33) through the higher order derivative (d/dt) in the second term of each. In pratice, our step $s_i(t)$ is viewed through an instrument of finite bandwidth. Obviously for time shifts that are large with respect to the period range of interest our approximation of (3.20) will be in error.

Time shifts are also caused by singularities in $\partial R(p)/\partial v_j$ and $\partial \tau(p)/\partial v_j$. These singularities are also responsible for nonlinearities in (3.25) and (3.33) over small ranges in p and hence small intervals of time. Again it can be argued and checked numerically that these singularities introduce significant error only at high frequencies.

Therefore, it seems plausible that our approximation of (3.20) by neglecting higher order terms may be reasonably linear for periods that are longer than the time shifts implied by the velocity perturbation. Chapman and Orcutt (1980) make explicit use of this behavior by inverting the waveforms in the

frequency domain and effectively filtering the high frequency components. In our subsequent work we will invert the data in the time domain and rely on the long period source function to act as a low pass filter. We will also restrict the size of the velocity perturbation allowed in any one iteration.

3-4 Examples of the Inversion Procedure

We will demonstrate the inversion procedure by attempting to invert for a model used to generate some synthetic "data". The "true" shear velocity model indicated in Figure 3.1 was used to generate six SH seismograms (assuming the WKBJ approximation is valid) from 15° to 25°. The model is similar to models proposed for the Western U.S. (model TNA of Grand and Helmberger, 1983). We will try to recover the true model from an initial model, also indicated in Figure 3.1 in which the rapid increase in velocity around 400 km depth has been removed.

Figure 3.2 shows the "data" and the synthetics for the initial model. The biggest discrepancy is the absence of the large reflection apparent at 15° in the initial model. This reflection is due to the 400 km discontinuity.

We invert the trial data by allowing the velocity structure to vary between 100 and 600 km depth. The velocity-depth function is sampled at 25 km intervals and the velocity is assumed to vary linearly with depth in each interval. The normalization time window W_j is 35 sec and the total time window for inversion, T_j, is 52 sec for each seismogram. The inversion is stabilized by assuming observation errors of 0.05 for the normalized observations, $\hat{\sigma}_j(t)$, and by limiting the maximum variance of any one parameter correction to 0.005 km/sec. Travel times are not used in this test case and the normalization correction

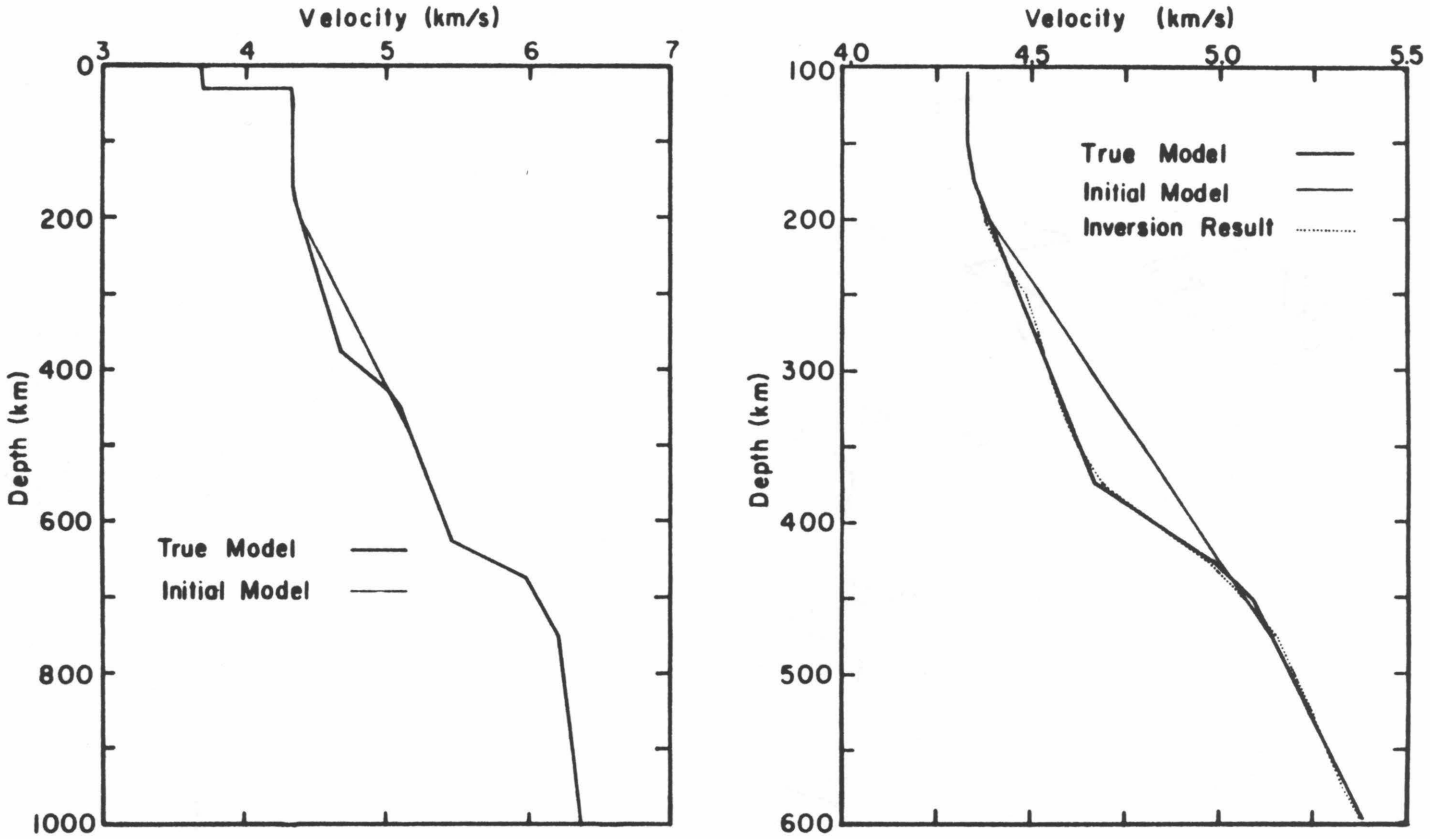

Figure 3.1 Upper mantle models used in trial inversion (before earth flattening transformation). Left) Velocity structure used to generate "data" compared to starting model for the inversion. The starting model does not have a high velocity gradient near 400-km depth. Right) Velocity structure (100 km - 600 km) resulting from 16 iterations of the inversion procedure compared to the starting and "data" model.

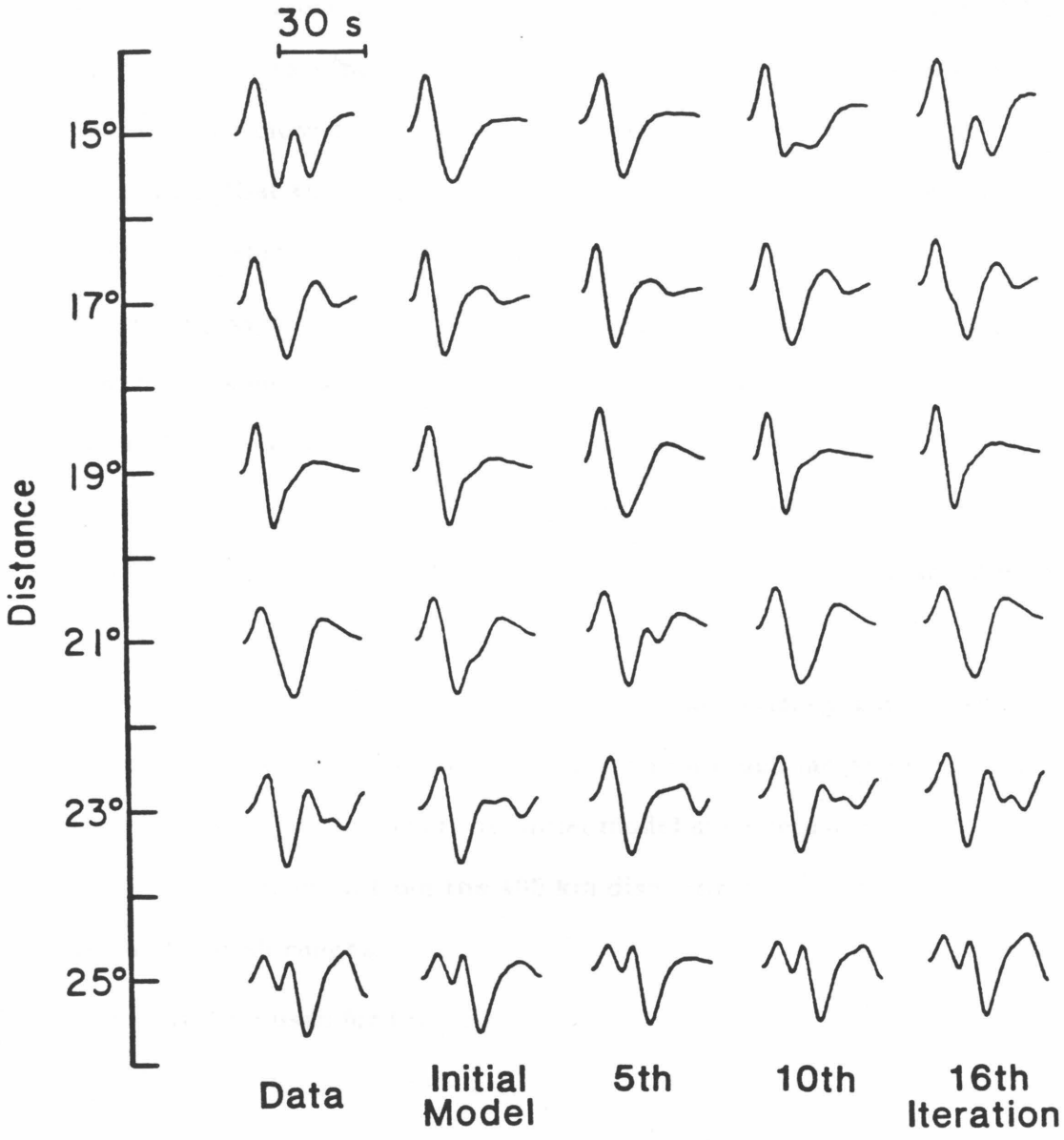

Figure 3.2 Comparison of "data" seismograms and synthetic seismograms for a trial inversion. The data, initial and final models are given in Figure 3.1. After 16 iterations the "data" waveform has been completely modelled.

factors were omitted from the parameters.

After 16 iterations, no further significant parameter corrections are calculated. As evident in Figure 3.2 the synthetic seismograms are virtually indistinguishable from the data. The model resulting from the inversion is shown in Figure 3.1 and is very close to the true model used to generate the "data". It is very encouraging that the inversion procedure can accurately fit seismograms even when the initial model is substantially in error.

Another, perhaps more interesting test case involves the ambiguities caused by the presense of a low velocity zone. In Figure 3.3, the model labeled "data" is used to generate synthetic seismograms. The WKBJ approximation is used for the depth intervals 200-405 km, 405-600 km and >600 km. Generalized ray theory is used to compute the response above 200 km and from the discontinuities at 405 and 600 km.

We start with a model with a less pronounced low velocity zone, a smaller velocity gradient between 200 km and 405 km, and a much larger discontinuity at 405 km. The seismograms from the initial model are compared to the "data" in Figure 3.4. The reflection from the 405 km discontinuity is much too large in the initial model at all ranges.

The stabilization used for this trial inversion is identical to that used for our first test. The velocity model was permitted to vary between 50 and 450 km depth. The normalization correction factors are introduced and assigned a weight of four relative to the model corrections through the parameter covariance matrix $\mathbf{W}$.

Figure 3.4 also shows the results after 10 and 16 iterations of the inversion procedure. The numbers accompanying each seismogram in the figure are

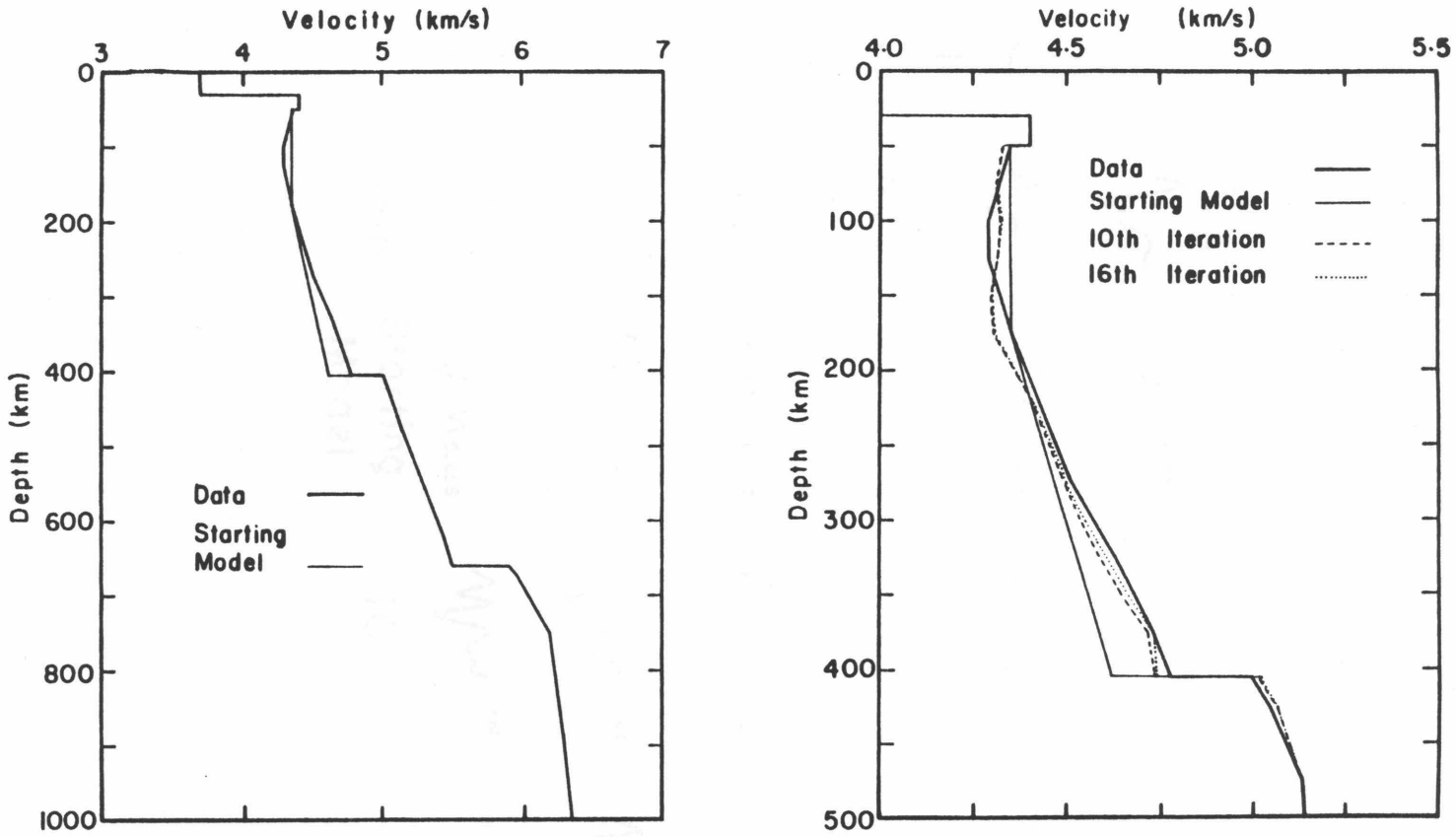

Figure 3.3 Upper mantle models with low velocity zones used in trial inversion (before earth flattening transformation). Left) Velocity structure used to generate "data" compared to starting model for the inversion. The starting model has a much less pronounced low velocity zone. Right) Velocity structures (0-500 km) resulting from 10 and 16 iterations of the inversion method. The differences resulting from the final 6 iterations are slight.

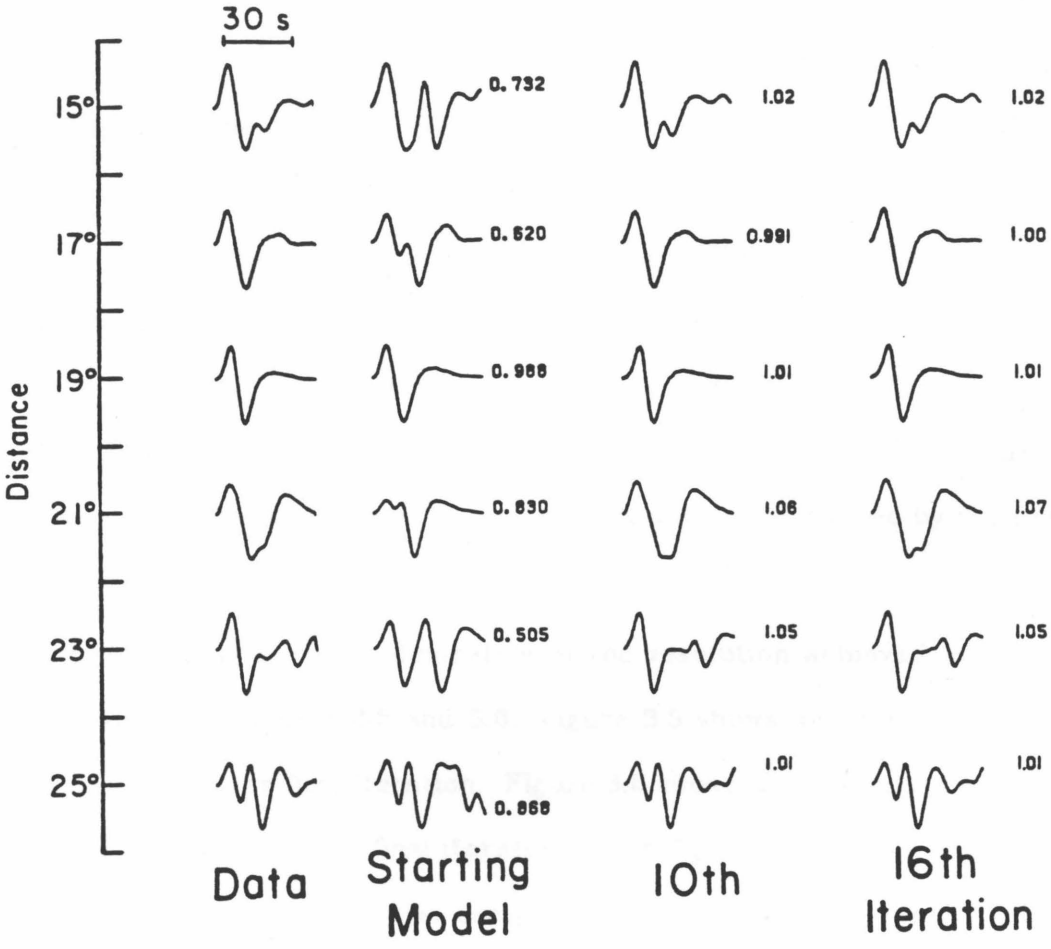

Figure 3.4 Comparison of "data" seismograms and synthetic seismograms for a trial inversion. The corresponding velocity models are given in Figure 3.3. The number accompanying each seismogram reflects the quality of the waveform comparison; 1 is a perfect fit. After 10 iterations, the significant features in the "data" have been modeled in the synthetics.

$$\varphi_j = \frac{\int_{T_j} \hat{s}_j(t-\tau)\hat{o}_j(t)\,dt}{\int_{T_j} \hat{o}_j(t)\hat{o}_j(t)\,dt.} \tag{3.34}$$

where $\hat{o}_j(t)$ has been corrected for normalization errors. The change in φ_j for each seismogram is indicative of the improvement in the fit. After 10 iterations, most of the significant features in the data are matched by the synthetics; six more iterations do not improve the fit significantly.

The resulting velocity models are shown on the right side of Figure 3.3. As might be guessed by the small changes in waveform between the 10^{th} and 16^{th} iteration, little perturbation in the velocity structure resulted from the final 6 iterations. The models are significantly different from the model used to generate the data, a manifestation of the nonuniqueness caused by the presence of the low velocity zone.

Averaging kernels, illustrative of the resolution achieved in the inversion, are shown in Figures 3.5 and 3.6. Figure 3.5 shows where model changes were resolvable in the first iteration. Figure 3.6 shows the resolution at the tenth, or for practical purposes, final iteration. Both figures demonstrate that at no time during the inversion process are perturbations to velocity structure in low velocity zone well resolved. The gradient between 200 and 405 km appears to be resolvable to wavelengths of 100 km or so. The velocity immediately below the 405-km discontinuity is poorly resolved. Both figures suggested that, although the problem is nonlinear, the resolution achievable with this data set is not a strong function of velocity structure, for the perturbation of the model required by this inversion.

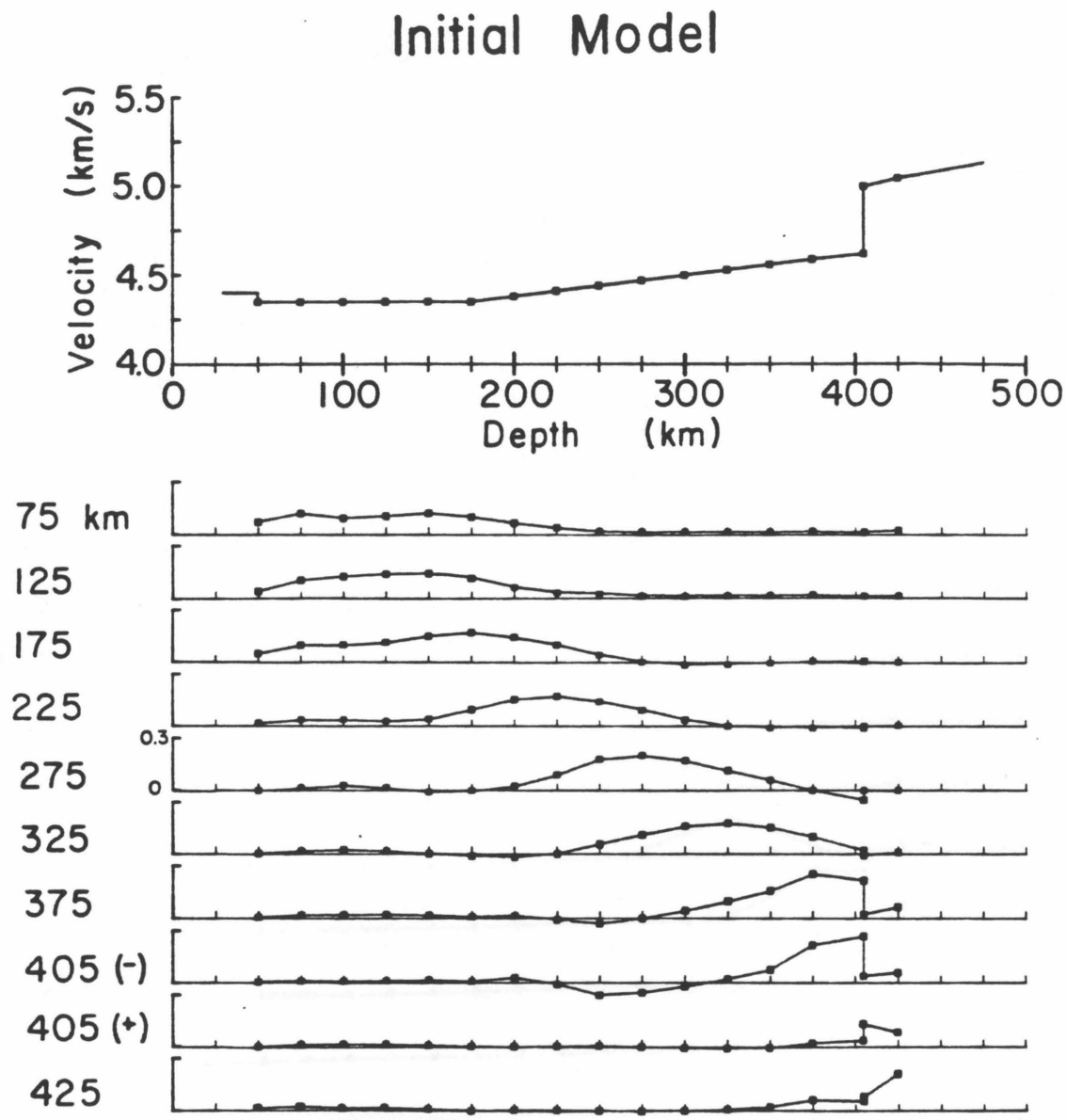

Figure 3.5 Resolution curves for the initial iteration in the trial inversion presented in Figures 3.3 and 3.4. Top) Initial velocity model sampled at approximately 25 km intervals. The points indicate which samples are determined in the inversion procedure. Bottom) The averaging kernels for various depths of the velocity structure. (-) and (+) denote above and below the discontinuity, respectively. The horizontal axis is depth and corresponds to the depth axis of the velocity-depth function shown at the top of the Figure. This Figure illustrates the model perturbations from the initial model which are resolvable given the errors assigned to the waveforms and the desired accuracy of the model perturbations.

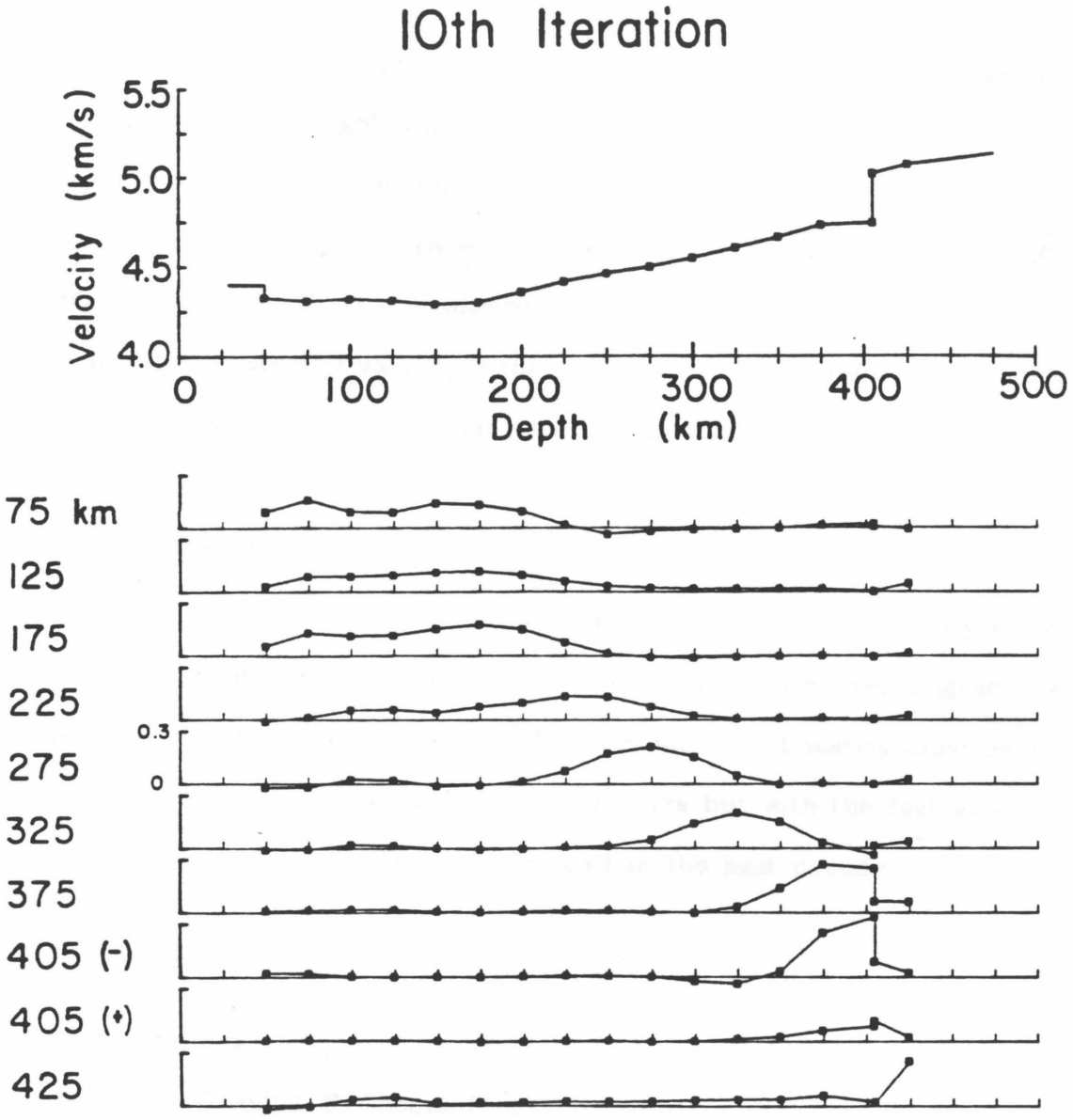

Figure 3.6 Resolution curves for the 10th iteration, the final model resulting from the trial inversion shown in Figures 3.4 and 3.5 (see Fig 3.5 for description). The differences in the resolution curves shown above and those shown in Fig. 3.5 are not substantial, indicating that the resolveability of the inversion procedure is not changing with respect to changes in the velocity model.

3-5 Discussion

The trial inversion problems considered here are only simple examples to illustrate how we might implement the technique. Although inversion of synthetic data is intrinsically dull, known exercises such as these prove enlightening for investigating the tradeoffs between the velocity structure in different regions of the earth. It may also prove interesting to invert synthetic data generated for a laterally varying model in order to study how our assumption of lateral homogeneity may bias our interpretation.

3-6 Conclusions

Normalized waveform data can be directly inverted for velocity structure. The differences in the normalized observed and theoretical seismograms can be modeled by perturbations to the velocity model. Nonlinearity must be accommodated by iterating several (or many) times but with the fast approximate solutions to the wave equation developed in the past decade, the inversion is practical.

3-7 References

Backus, G. E. and J. F. Gilbert, (1967), Numerical application of a formalism for geophysical inverse problems, *Geophys. J. R. Astr. Soc.*, *13*, 247-276.

Backus, G. E. and J. F. Gilbert, (1968), The resolving power of gross earth data, *Geophys. J. R. Astr. Soc.*, *16*, 169-205.

Backus, G. E. and J. F. Gilbert, (1970), Uniqueness in the inversion of inaccurate gross earth data, *Phil. Trans. Roy. Soc. London, Sec-A, 266*, 123-192.

Chapman, C. E., (1978), A new method for computing synthetic seismograms,

Geophys. J. R. Astr. Soc., *54* , 481-518.

Chapman C. H. and Orcutt J. A., (1980), Inversion of seismic refraction data (abst), *EOS, Trans. Am. Geophys. Union.*, *61* , S-118.

Grand S. P. and D. V. Helmberger, (1983), Upper mantle shear structure of North America, *Geophys. J. R. Astr. Soc.* (in press).

Lanczos, C., (1961), *Linear Differential Operators*, D. Van Nostrand, London.

Mellman, G. R., (1980), A method of body-wave waveform inversion for the determination of earth structure, *Geophys. J. R. Astr. Soc.*, *62* , 481-504.

Wiggins, R. A., (1972), The general linear inverse problem: implication of surface waves and free oscillations for earth structure, *Reviews of Geophys. and Space Phys.*, *10* , 251-285.

Chapter 4 Inversion of SH-Waves for the Upper Mantle Structure beneath the Western U. S. and East Pacific Rise

4.1 Introduction

The structure of the shear velocity of the upper mantle is constrained largely from surface wave and free oscillation data and the travel times of body phases (e.g. Dziewonski and Anderson, 1981). These data can resolve the gross structure of the upper mantle under much of the world and are useful in mapping out large scale lateral heterogeneity (e.g. Dziewonski and Steim, 1982; Nakanishi, 1981; Dziewonski et al., 1977). However, they are difficult to use to determine the interesting features of the fine structure. More detailed information of the shear structure and its regional variation can be obtained by modelling shorter-period, higher-mode Rayleigh waves (e.g. Cara, 1978; Lernar-Lam and Jordan, 1983). Still these data cannot resolve the S-wave structure to the same extent as is possible to achieve for P-waves. We must investigate the shear structure from the viewpoint of body waves to accomplish this.

There have been few studies of S-wave body phases for the determination of detailed upper mantle structure. Ibrihim and Nuttli (1967) and Nuttli (1969) have studied the travel times of S-waves recorded on long-period seismograms. Kovach and Robinson (1969) and Robinson and Kovach (1972) used a long-period array of seismographs in Arizona to measure apparent velocities($dT/d\Delta$) of S-waves. All of these authors detected multiple arrivals that they interpreted as

due to an upper mantle structure with features similar to those proposed by detailed interpretations of P-wave observations.

These investigators used simple geometrical optics to interpret their travel time and $dt/d\Delta$ data and did not quantitatively take into account the effects of complicated wave propagation phenomena that are important in interpreting these data. Thorough modeling studies of long-period body waves by Helmberger and Engen (1974), Burdick and Helmberger (1978), Lay and Helmberger (1983), Grand and Helmberger (1983), as well as Chapter 1, have demonstrated that, when the other variables such as source and attenuation can be accurately accounted for, these phenomena can be accurately modeled and the observed seismograms can be used to provide constraints on the detailed structure of the mantle. In most regions of the world this is the only type of data available providing information about the fine structure. Helmberger and Engen (1974) proposed that the various S-wave models could be tested by comparing observed seismograms to theoretical ones and refined shear velocity models for the western U.S. to derive one that could simultaneously fit the observed travel times, $dT/d\Delta$, and waveform data. Helmberger and Engen (1974) also found that the previous investigators had not fully realized the extent to which vertically polarized S waves (SV) are contaminated by crustal structure and that some of the later arrivals identified on the seismograms may have been misinterpreted. In their study, Helmberger and Engen (1974) focussed primarily on horizontally polarized SH waves for modeling structure.

Grand and Helmberger (1983) applied the same technique to the study of SS waves for paths beneath the tectonic region of North America and East Pacific Rise and for paths beneath stable continental regions of North America.

By analyzing the SS-S differential travel times and by modeling the waveforms, they were able to determine the extent of the lateral heterogeneity in the upper mantle beneath North America and estimate the depth to which it must persist. Using this technique and similar data, they proposed to map out a large part of the world.

Using the waveform data typically invloves a trial and error inversion through complex forward modeling experiments. These calculations are crucial in the early stages of an investigation for understanding the nature of the propagation phenomena under observation and a preliminary, qualitative, interpretation is fairly easy to make. However, more quantitive information appears to be resolvable from the data, justified by observable consistencies and trends in the seismograms. To extract this information, we must construct models to accurately predict the observations. Such a procedure involves making many, small perturbations to our initial model that affect the calculations in ways that are very difficult to predict: It is useful to develop an automated inversion method to speed up the analysis, particularly in the stages after a preliminary interpretation of the data has been made. Methods of inverting observed seismograms, utilizing the direct inversion of the observed waveforms, have been being used to interpret fundamental and higher-mode surface waves (Dziewonski and Steim, 1982; Woodhouse, 1983; Lernar-Lam and Jordan, 1983) and regional body waves (Wallace, 1983). Mellman (1980) and Chapman and Orcutt (1980) have developed methods for inverting body-wave seismograms and have applied them to the interpretation of oceanic refraction data. These data had been previously interpreted by extensive trial and error modeling. Their results are encouraging and suggest that once a thorough understanding of the observed phenomena has

been obtained, an inversion method is, indeed, very useful.

In the following paper we will apply a simple waveform inversion technique to the interpretation of horizontally polarized shear waves observed in the western U.S. The region has been previously investigated by Grand and Helmberger (1983) using the SS phase. Our purpose is to use a different data set to verify their result, test the capability of an automated inversion scheme, and determine the resolution of the various features in the upper mantle structure.

4.2 Observations

Tangential component (SH polarized) seismograms from 24 events located in the western United States, Gulf of California, and East Pacific Rise comprise the data set used in our study. The recording seismographs are located in the western and central U. S. such that the travel paths sampled primarily the tectonic regions of the U.S. and Mexico, consistent with the regionalization proposed by Grand and Helmberger (1983). The earthquakes selected are shallow and have predominantly strike-slip focal mechanisms. Seismograms from these events are chosen such that the azimuth from source to receiver is in the direction of maximum SH energy radiation, and such that the SH energy was recorded principally on one component (i.e. naturally rotated seismograms) in order to minimize any possible SV contamination.

We expend the effort of examining over 100 events from 1964 through 1979 in order to obtain a data set that can be easily interpreted. The SH waveform from a strike-slip earthquake does not change with azimuth. Furthermore the surface reflection sS has the same polarity as direct S and the time separation $t_{sS}-t_S$ does not change significantly for distances from 15° to 50°. Shallow

strike-slip earthquakes thus yield very simple waveforms that change only in dominant period from event to event as the depth and source time function change. For each event, we can estimate the source from a single teleseismic SH-wave seismogram and that source will be appropriate for all SH-wave records from that event.

There are several other important reasons for concentrating on SH-wave seismograms. As mentioned earlier, Helmberger and Engen (1974) found that the SV waveforms can be severely distorted at the distance ranges of interest (15^{o} to 30^{o}) due to coupling with P-wave energy at the source and receiver. Another reason for examining only SH energy is that the upper-mantle may be anisotropic as proposed by Dziewonski and Anderson (1981). Although we will assume the upper mantle is isotropic in our modelling study, we feel it will be easier to reinterpret this data set in the context of other hypotheses if we confine our observations to only the one type of motion.

We did not perform detailed focal mechanism studies for all of the events selected. When possible, events with published mechanisms were used (Dean and Drake,1978; Molnar and Sykes ,1969; Chandra, 1974). Otherwise we chose events based on a favorable tectonic setting (e.g. fracture zone earthquakes) and estimated from the observations whether our assumptions concerning depth and focal mechanism were correct.

The earthquakes selected and the corresponding source parameters are listed in Table 4.1. Figure 4.1 shows the source regions and the recording stations. The propagation paths are primarily in the tectonic region as delineated by Grand and Helmberger (1983) with a few exceptions. The tectonic region of Grand and Helmberger includes the western half of Mexico, the East Pacific Rise,

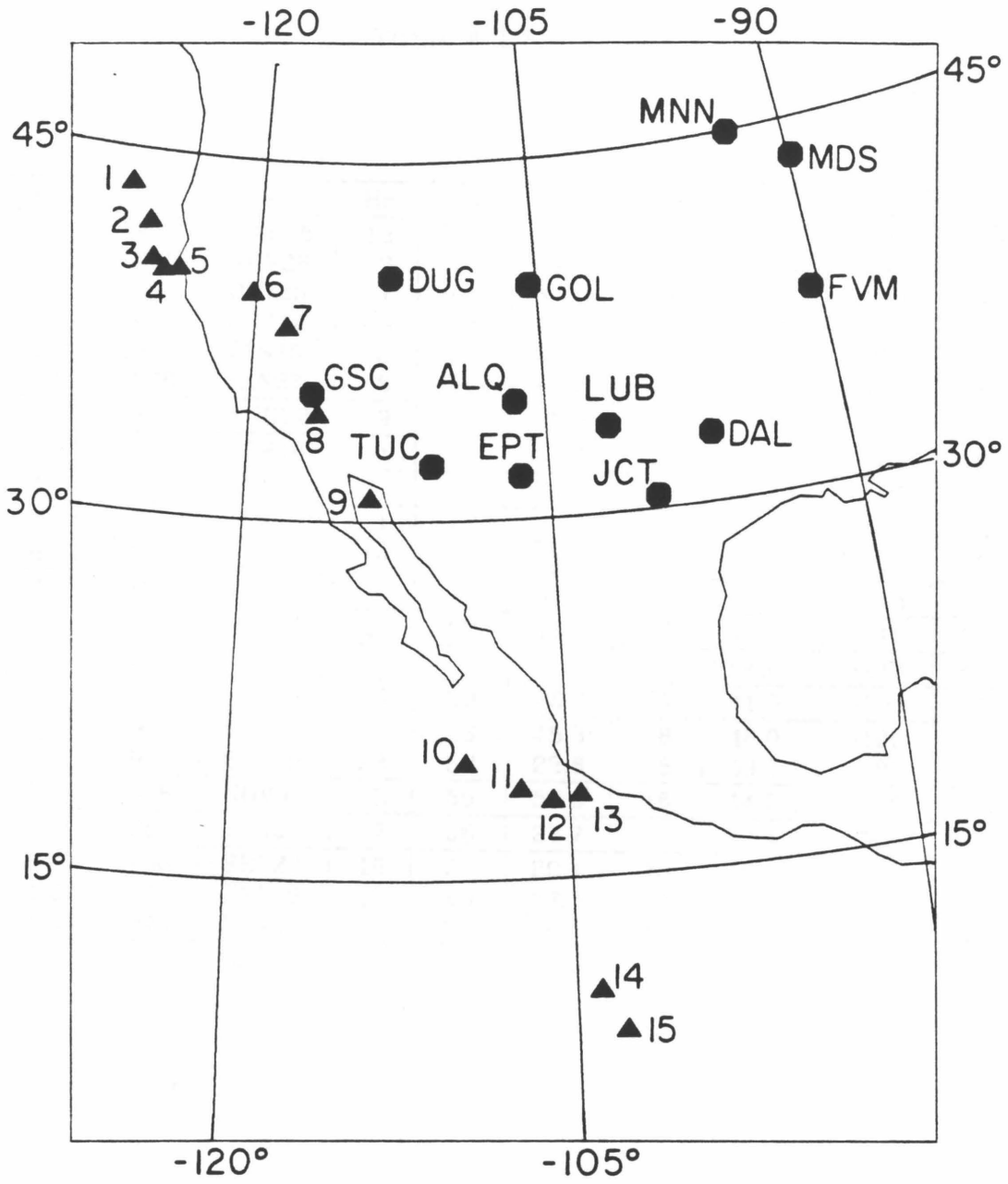

Figure 4.1 Map of events and seismograph stations used in this study. Sources are triangles; stations are octagons. An azimuthal equidistant projection centered on source 9 is used.

Table 4.1 Event List

No	Yr	Date	Hr	Min	Sec	Lat		Long	
1.1	1968	MAY08	12	17	13.4	43	34.0	-127	53.9
1.2	1970	NOV26	3	11	42.8	43	46.56	-127	26.94
1.3	1972	OCT25	1	01	41.0	43	26.3	-127	43.9
1.4	1973	OCT12	5	54	27.7	43	44.2	-127	28.1
1.5	1976	JAN10	8	58	47.5	43	33.1	-127	25.9
1.6	1976	JAN27	16	06	47.5	43	34.3	-127	24.5
2	1963	AUG22	9	27	3.3	42	0.0	-126	24.0
3	1965	SEP16	4	10	8.8	40	30.0	-125	48.0
4	1970	SEP13	21	10	21.0	40	7.8	-125	4.8
5	1968	JAN26	1	42	20.5	40	13.8	-124	16.2
6	1966	SEP12	16	41	1.1	39	25.2	-120	9.0
7	1968	FEB06	0	41	38.6	38	1.2	-118	21.0
8	1979	MAR15	21	07	16.5	34	19.0	-116	27.0
9	1963	NOV19	8	23	12.0	30	54.0	-113	48.0
10	1973	JAN13	8	39	26.8	19	41.5	-109	29.9
11.1	1966	FEB08	17	06	45.3	18	48.0	-106	48.0
11.2	1969	SEP23	22	37	22.6	18	39.7	-107	4.3
12	1968	NOV01	3	55	50.3	18	14.3	-105	39.8
13	1969	JUN23	7	08	27.7	18	22.4	-104	32.8
14.1	1966	SEP23	16	24	20.4	10	18.0	-104	6.0
14.2	1970	FEB08	16	40	57.5	10	2.7	-104	10.1
14.3	1975	NOV14	10	50	10.5	10	20.3	-103	35.1
15.1	1965	OCT15	0	34	8.9	8	30.0	-102	54.0
15.2	1978	DEC17	8	01	32.0	8	39.9	-102	55.3

the Gulf of California, and the U.S west of GOL and LUB. We choose to include seismograms from FLO, FVM, DAL, MNN, and MDS from California-Oregon events because the waveforms appear to be consistent with the other seismograms located well within the tectonic region. We proceed with caution, however, since Grand and Helmberger (1983) reported SS-S travel time variations of as much as 5 s from events on the East Pacific Rise recorded at stations LUB and DAL suggesting that the shear velocity in the upper mantle is increasing rapidly from the western to the central U.S. This observation was, in part, the basis of their regionalization. Lay (1983) summarized several studies of teleseismic S residuals that also suggests that this is true.

The data are displayed as profiles in Figure 4.2. Also shown in Figure 4.2 are synthetics for model TNA, (shown in Figure 4.3) proposed for the western U. S. by Grand and Helmberger (1983) based on observations of SS phases. The observed seismograms in Figure 4.2 are aligned such that the first arrival is approximately at the time predicted by model TNA. As discussed above we expect that events recorded in the central U.S. may show some effects of lateral heterogeneity. We therefore separate the observations into two profiles based on source locations. The profile labeled EPR includes events on the East Pacific Rise and in the Gulf of California, recorded on western U.S. seismograms; the other profile consists of seismograms recorded from California and Oregon events. In the second profile, seismograms beyond 20° may be affected by lateral velocity gradients in the upper mantle.

The lines labelled AB, CD, EF on the synthetic profile in Figure 4.2 correspond to predicted arrivals for model TNA based on the travel time curve (Figure 4.4); retrograde branches BC and DE have been omitted. The similar

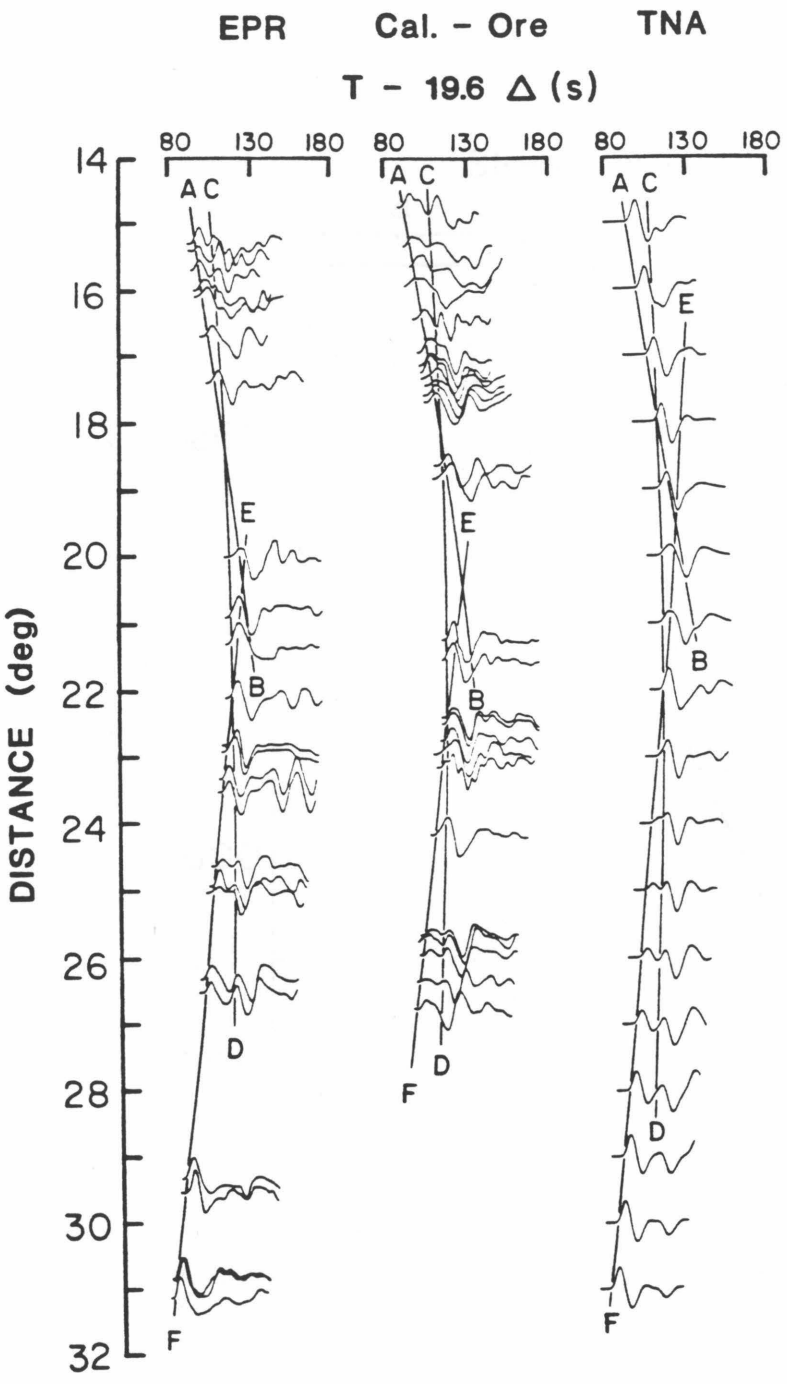

Figure 4.2 Profiles of observed SH seismograms and synthetics predicted for TNA. EPR refers to sources on the East Pacific Rise; Cal-Ore refers to events in California and the Coast of Oregon. The travel time curve for TNA is superposed on the synthetics. The corresponding times superposed on the data reflect our interpretation of the arrivals present in the observations.

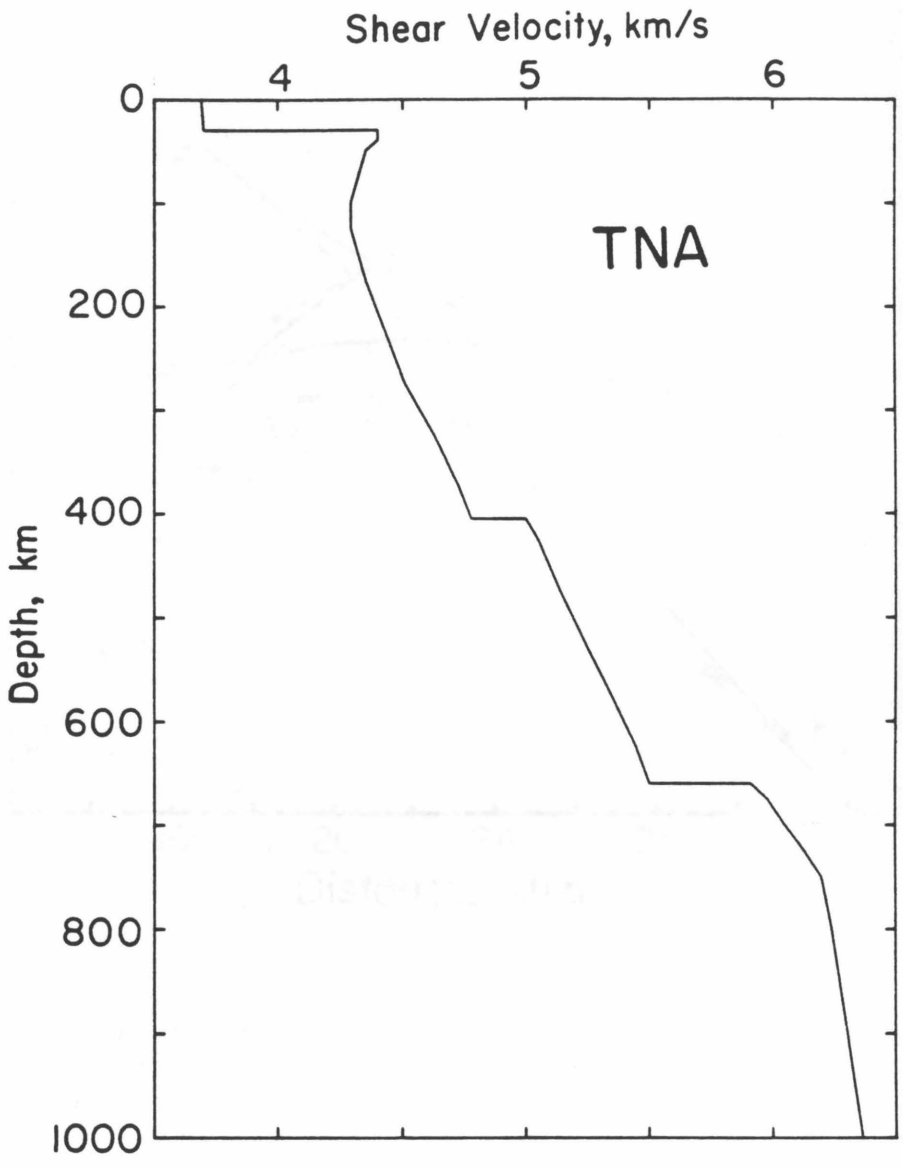

Figure 4.3 Velocity model TNA (Grand and Helmberger, 1983).

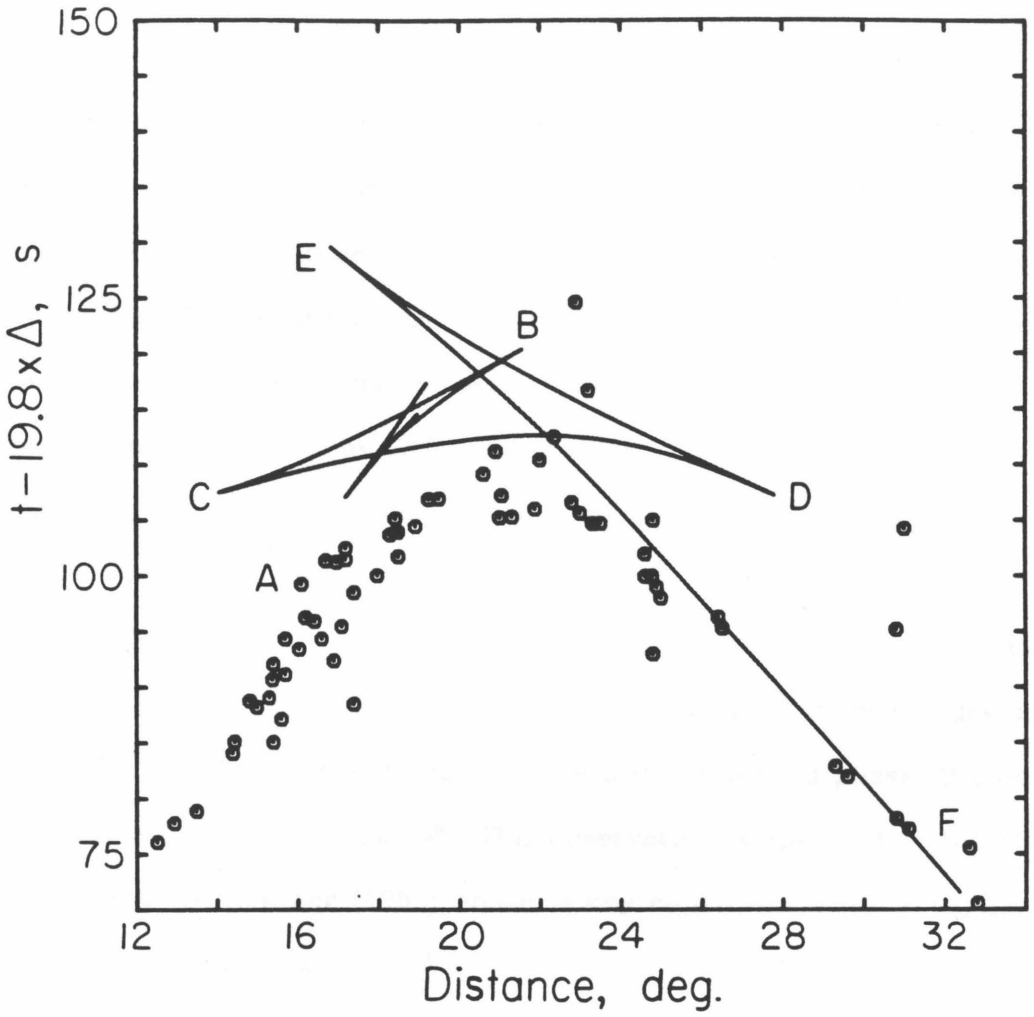

Figure 4.4 Absolute travel time data and travel times predicted by model TNA. The observed travel times are faster than predicted by TNA to at least 20°.

lines on the observed data indicate the upper mantle arrivals we observe in the data.

Both record sections show a clear second arrival in the distance range 14° to 17° which moves forward with respect to the first arrival. This feature is interpreted as the CD arrival, and in model TNA, as well as most models of the upper mantle, it is predicted by an increase in velocity around the depth of 400 km. In both data sections this arrival is larger in amplitude relative to the first arrival than predicted by TNA. The relative amplitude of this phase is perhaps larger for events from California and Oregon than for events located in the Gulf of California (included in the EPR section). On both the observed and the synthetic profiles the relative arrival times of the first and second phases are predicted accurately by model TNA. The CD branch becomes the first arrival at 18°. The AB branch never appears as a distinct second phase; the end of the branch, point B, occurs at 21°. This observation is apparent in the SS data of Grand and Helmberger (1983) and is a key constraint used to fix the velocity structure above 400 km in TNA.

Another obvious feature in both the observed and synthetic profiles in Figure 4.2 is a second arrival moving back with respect to the first arrival in the distance range 24° to 27°. This second arrival is interpreted as the end of the CD branch; in model TNA it is predicted by another discontinuous velocity increase at 660-km depth. Unfortunately, clear observations of SH waves from 27° to 29° were unavailable, but the second arrival appears to have disappeared almost completely by 29.5°. TNA predicts the waveforms between 23° and 31° quite accurately. The branch EF never appears as a distinct latter arrival at distances near 19° to 20° because the large amplitude of the interference between

the AB and CD branches dominates the seismogram. Furthermore, the complexity and the variability of the initial part of the Love wave make interpretation of relatively small arrivals difficult.

The only obvious discrepancy between the two profiles is at distances between 24° and 27°. The records around 25.7° from California- Oregon look very similar to those at 24.8° from the East Pacific Rise. This may be a result of lateral heterogenity. The events from the East Pacific Rise are very consistent between stations from 22°-32°, so we will model these seismograms carefully. In the following analysis we will treat the two profiles as the same for distances less than 21°.

Because of the apparent lateral variations of the upper mantle in the west and central U.S., we must be careful when interpreting absolute travel time data. We will consider travel times from the East Pacific Rise and Gulf of California events recorded at stations west of, and including JCT, along with California-Oregon events recorded at stations west of, and including LUB. Relevent data from Helmberger and Engen (1974) are also considered (see their Table 1).

The travel time data from the events in the profiles in Figure 4.2, particularly those in the Gulf of California and on the East Pacific Rise, are not expected to be very accurate. The events are small, shallow, strike-slip earthquakes and the P-waves are poorly recorded teleseismically. One need only refer to the ISC bulletins for an estimate of the location accuracy. Most of the P-wave recordings at distances greater than 25° are emergent and the resulting locations often indicate source depths of greater than 100 km for events on the East Pacific Rise. The locations are determined using avelocity structure that is probably not appropriate. Furthermore, most of the recording stations are to

the east and north of the source locations. The azimuthal coverage, necessary for accurate source location, is incomplete. We recognize that some of our travel time data may be inaccurate and may be possibly contain systematic errors, especially beyond 20°.

Another way of constraining travel time is to use SS-S differential times. The work of Grand and Helmberger (1983) is very useful to this extent. Their model TNA accurately fits the SS-S times observed for event on the East Pacific Rise as well as the slowest S-wave travel times observed for well-located events in the western U.S. recorded at distances less than 15°.

The travel time data are plotted in Figure 4.4 along with the travel time curve for model TNA. The data for distances less than 20° include the California-Oregon data from Figure 4.2 and the data from Helmberger and Engen (1974). The end of the geometric shadow zone for model TNA is at about 17°, however, this does not preclude the interpretation of travel times for shorter distances, say to 14°. We simply interpret the travel time as being the arrival of near critical reflection from the base of the low velocity zone in model TNA (see Figure 4.3).

From Figure 4.4 it is apparent that we have a difficult decision concerning what absolute travel times we should use to constrain our velocity model. The observed travel times appear to be systematically less than those predicted by TNA at distances less than 24°. On the other hand, TNA satisfies the SS-S travel times for paths that are substantially the same as the ones that we are considering. The data for distances greater than 20° are, perhaps, subject to the uncertainties discussed previously and the discrepancy between TNA and the observations is not necessarily significant. The data for the distances less than

19°, however, include well located events and the difference between the observations and the predictions of TNA cannot be as easily dismissed; we will investigate the implication of this discrepancy in travel times below.

In summary, the observational features in the data which we consider significant are:

1) a large later phase moving forward with respect to the first arrival from 15° to 18°;

2) relatively simple waveforms from 18° to 23°;

3) a large second phase arriving progressively later with respect to the first arrival at distances from 23° to 29°; and

4) simple waveforms beyond 30°.

The implications of different assumptions concerning absolute travel times will be considered.

4.3 Synthetic Seismograms for SH-waves

As is common in modeling studies of upper mantle structure, we will assume that a synthetic seismogram $s(t)$ can be computed by a series of convolutions:

$$s(t) = i(t)*a(t)*r(t)*e(t)*m(t)$$

where $i(t)$ is the instrument response, $a(t)$ is an attenuation operator, $e(t)$ is the earthquake source function, $r(t)$ is the source and receiver structure and $m(t)$ is the upper mantle response. A brief review of the approximations and assumptions involved in this computational procedure is appropriate.

The source function, $e(t)$, is very simple for the events considered in this study. For strike-slip events, assuming a point source, the source wave shape (including the sum of direct S and the reflection from the surface sS) does not depend on azimuth and changes negligibly with respect to distance. Therefore, a single observation of each event at a distance where the propagation effect is not important (i.e. 30° to 90°) is sufficient to estimate the source function.

The operator $a(t)$ is a Futterman operator (Futterman, 1962) and models the effects of attenuation. We will assume that attenuation decreases with depth such that the ratio of travel time to Q, t/Q, is approximately a constant ($t/Q=4s$) for the distance ranges considered. This assumption may not be entirely appropriate but we lack the data to constrain Q. New constraints on attenuation may require that our results be modified.

The effects of the near-source and near-receiver structure are modeled through the operator $r(t)$. Langston (1977) and Burdick and Langston (1977) found that three dimensional structure near the receiver can significantly affect the observed seismogram. These authors observed converted P to S phases beneath Corvallis, Oregon (WWSSN station COR) and interpreted the waveforms in terms of dipping structure in the crust and upper mantle. We find no evidence of substantial effects on the waveforms at the stations we used due to source or receiver structure and, therefore, this operator is assumed to be an impulse.

The quantity $i(t)*a(t)*r(t)*e(t)$ is considered as an effective source; the unknown response $m(t)$ is to be estimated from the observations and is to be interpreted in terms of the velocity structure of the upper mantle. An example of the effective source function can be seen in Fig. 4.2 by inspecting

seismograms at distances greater than 30°. In general, it is very simple and changes slightly from event to event due to variation in source time function and source depth. Because of the simple nature of the source, the effects of upper mantle structure are easy to observe in Figure 4.2.

We will model the earth structure response by combining the WKBJ approximation with generalized ray theory. For regions of the upper mantle where the velocity is slowly varying, we assume the WKBJ approximation is valid and construct the response using the method of Chapman (1978) and Wiggins (1976). Discontinuities or low velocity zones are modeled using a generalized ray expansion in a plane-layered approximation of the velocity structure to isolate the energy that has interacted with those regions where the WKBJ approximation is invalid. The response due to the generalized ray expansion is computed by the Cagniard-de Hoop technique (Helmberger, 1968). The two methods can be combined (see Chapter 2) to give a very good approximation that can be computed very efficiently.

4.4 Inversion

In order to easily assess the effects of various constraints, we devise an inversion algorithm to treat the waveform data. Because the absolute amplitudes are poorly understood and the seismograms used as data come from several different events, it is necessary to normalize the observations to remove the amplitude from consideration. Following Mellman (1980), given the jth observed seismogram, $o_j(t)$, and the corresponding synthetic seismogram, $s_j(t)$, we define the normalized observation, $\hat{o}_j(t)$ and synthetic, $\hat{s}_j(t)$ as

$$\hat{o}_j(t) = \frac{o_j(t)}{P_{oj}} \tag{4.1}$$

and

$$\hat{s}_j(t) = \frac{s_j(t)}{P_{sj}} \tag{4.2}$$

where

$$P_{oj} = \left[\int_{W_j} o_j^2(t)\,dt\right]^{1/2} \tag{4.3}$$

$$P_{sj} = \left[\int_{W_j} s_j^2(t)\,dt\right]^{1/2} \tag{4.4}$$

The window, W_j, must be carefully chosen to minimize the effects of noise on the normalization of the observed seismogram.

We then assume that differences in the observations and synthetics in some time window T_j (not necessarily equal to W_j) are related to the velocity structure by

$$\hat{o}_j(t) - \hat{s}_j(t) = \frac{\partial \hat{s}_j}{\partial m_i}\delta m_i + b_j \hat{o}_j \tag{4.5}$$

δm_i is the change in the ith model paramater, and b_j is an unknown correction factor to account for errors in the normalization of $o_j(t)$ due to noise or an incomplete description of the propagation effects. δm_i and b_j can be computed using the generalized inverse formulation of Backus and Gilbert (1967). Because the problem is actually non-linear, the linear approximation must be iterated several times depending on how accurately the starting model can predict the

observed seismograms. After convergence, the formalism of Backus and Gilbert (1968; 1970) can be applied to estimate how well the resulting features of the velocity model can be resolved.

The functions $\partial \hat{s}_j / \partial m_i$ can be easily computed using the WKBJ-Generalized Ray approximations. In the following analysis, we will assume that the velocity structure is parameterized by points on the velocity-depth curve at intervals of approximately 30 km; the velocity is assumed to vary linearly between points. No attempt was made to prevent the introduction of low velocity zones since the generalized ray method can be used to model these situations with reasonable accuracy.

The application of an inversion formalism to the waveform data is incomplete because no satisfactory means of estimating errors in the waveform data has yet been devised. We are still faced with using our subjective judgment concerning the quality of the fit between synthetics and data. Nevertheless, an inversion scheme is still very useful in determining how various starting models are to be modified to predict well observed features of the data.

4-5 Analysis

From the profiles in Figure 4.2, we select a subset of seismograms that are illustrative of the features which we will try to fit. We consider both profiles to be similar out to distances of 21°. Beyond 21° we will try to fit the waveforms from events on the East Pacific Rise.

As an example of the utility of waveform data for constraining the gross features of the structure, we invert for a model without using travel time information. A starting model is given in Figure 4.5 and consists of a constant

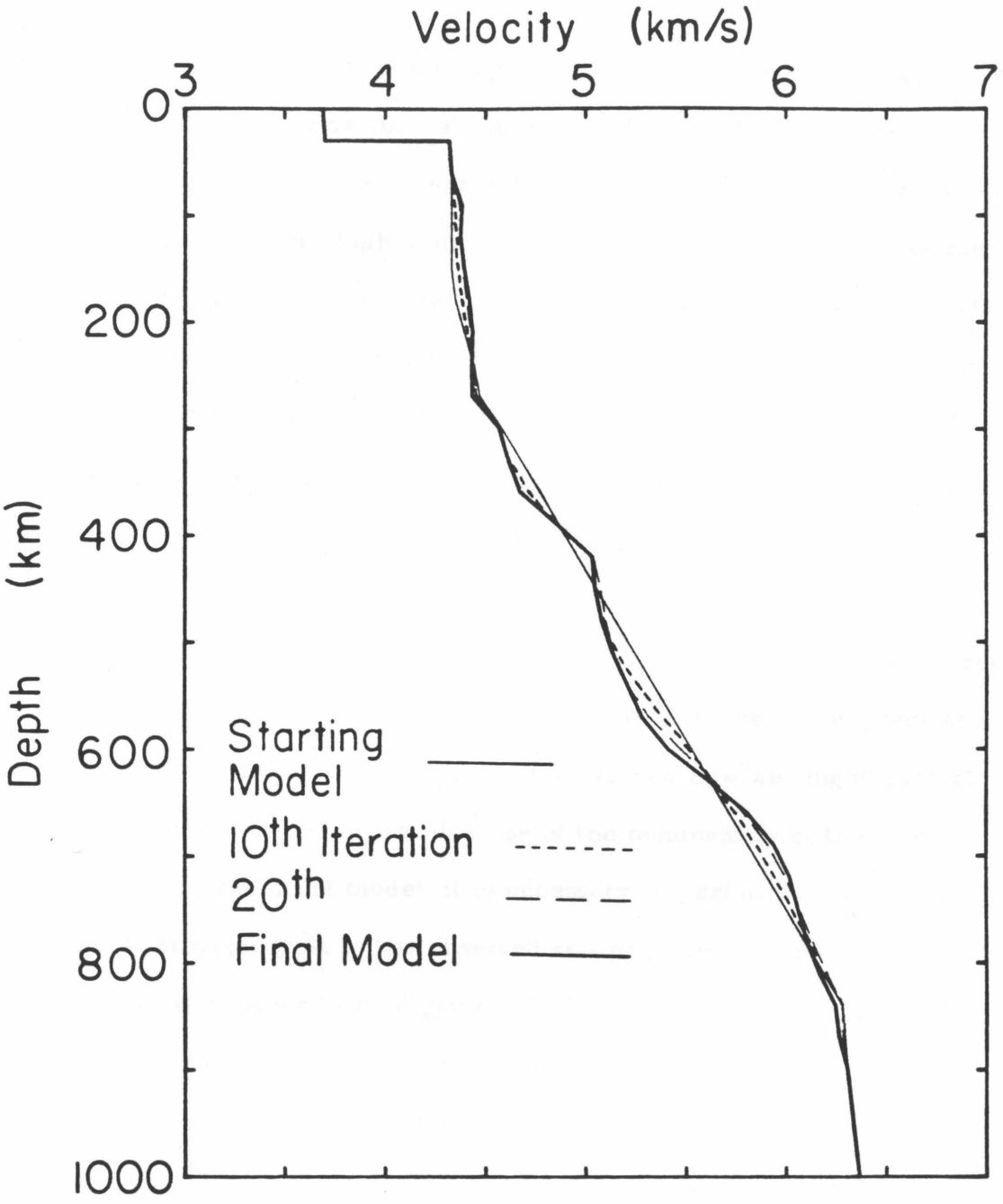

Figure 4.5 Velocity models resulting from a test inversion of waveform data alone.

velocity below a 30 km crust to a depth of 150 km, a slight velocity gradient to 270 km and a larger, constant, velocity gradient to 840 km. The velocity model was fixed below 870 km to an earth model which satisfies the Jeffreys-Bullen travel times. The thin, high velocity lid proposed by Grand and Helmberger (1983), as discussed earlier, is not expected to substantially affect the seismograms at 15° and so was omitted. The upper 200 km of the starting model are derived to approximate the travel times of model TNA between 15° and 18°.

The waveform data are shown in Figure 4.6 and include observations of the strong later phases between 15° and 17° and between 24° and 29°. The synthetics and data were aligned in time during each iteration such that the cross-correlation between them is maximized. The travel times are shown, referred to model TNA. It is obvious from Figure 4.6 that the starting model predicts none of data. We apply our inversion procedure to see how we might perturb the model to fit the waveform data. Because of the nonlinearity of the problem and the poor fit of the initial model, it is necessary to perform many iterations to achieve a satisfactory fit to the observed seismograms. We use a damped least square inversion procedure (Wiggins, 1972) and decrease the damping as the model converges to one that predicts the observations. Final convergence is achieved when decreasing the damping further caused only short wavelength perturbations to the model that do not significantly improve the fit to the observed waveforms. No particular effort is made to hasten convergence; we simply perform several iterations, check the convergence as indicated by the model perturbations, modify the damping, and iterate again. In this example, 25 iterations are performed before convergence results.

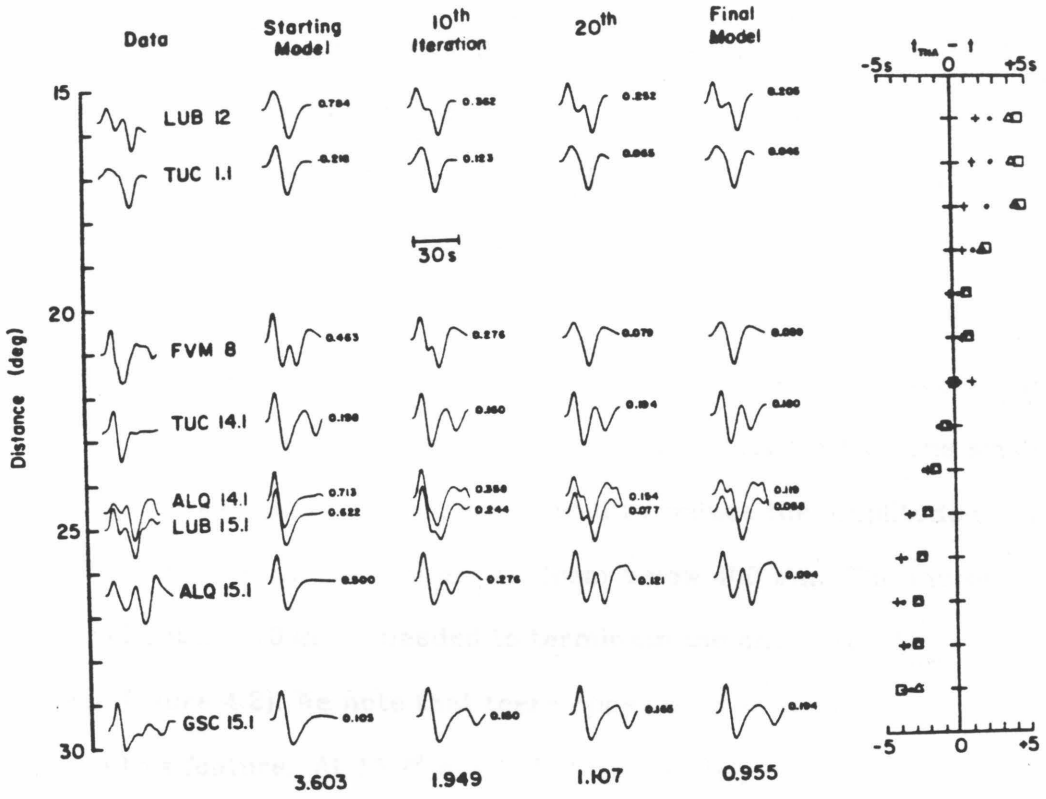

Figure 4.6 Data used in test inversion of waveform data alone compared to the synthetics at several stages of the inversion procedure. The models are shown in Fig. 4.5. Travel times predicted by the models are compared to model TNA. (+) indicates the starting model, (.) indicates the 10-th iteration, squares the 20-th, and triangles indicate the final model. The number accompanying each seismogram is proportional to the squared difference between observed and synthetic seismograms.

The resulting models after 10, 20 and 25 iterations are shown in Figure 4.5. The corresponding seismograms are shown in Figure 4.6. After 20 iterations most of the significant features in the waveforms have been fit. The final steps only slightly modify the waveforms beyond 24°. Although this model does not fit any reasonable estimates of the travel times, we can expect that the general features of the model will be reproduced in any acceptable final model. These features include a small average velocity gradient above 200 km, two region of large velocity gradients near 400 km and between 600 km and 700 km; and moderate velocity gradients from 200 to 300 km and from 400 to 600 km.

It is important to recognize those features in the data that are constraining the models. The discontinuity at 400 km is responsible for the second arrival at 15.7° and 17° consistent with the interpretation in Figure 4.2. The small overall velocity increase above 250 km is required to reduce the amplitude of the initial arrival relative to the second arrival from below 400 km. The increase in velocity gradient at 270 km is needed to terminate the end of the AB branch around 21° (see Figure 4.2). We note that there appears to be some inconsistency in the data on this feature. At 15.7° and 17° the wave shapes are predicted fairly well. However, it appears to be difficult to keep the gradient in the uppermost mantle low enough to satisfy the waveform data at the near distances, and yet terminate the AB branch soon enough to satisfy the data at 23°. This will be a recurring problem in subsequent inversion attempts. The reduced velocity gradient below the 400 km discontinuity is constrained by the relative timing of the arrivals at 15.7° and 17°. Finally the 600 km discontinuity is required by the strong later phase observed between 24° and 29°.

From the previous experiment we find that, from an adequate set of waveform data alone, we are able to resolve the gross features of the velocity structure in the upper mantle. Now we will refine our models given various travel time constraints. In our second experiment we will assume that the S-wave travel times predicted by model TNA are appropriate. Travel times are included in the inversion by assuming that the onset of the S-wave in the data occurs at the time predicted by model TNA. In addition, the data set is supplemented by travel time information. The starting model is the same as that used in the previous experiment.

Convergence to a reasonable final model is achieved in 15 iterations. The resulting model, designated MP2', is shown in Figure 4.7 and the seismograms are shown in Figure 4.8. In the process of the inversion, some features in the velocity structure have been introduced that are probably not resolvable by the data. For example the travel time curve for MP2' predicts an arrival from the AB branch to 26°, shown in Figure 4.9. The amplitude of this arrival is expected to be small because it is the result of small, very localized, heterogeneities in the velocity structure between 210 and 270 km. These features are artifacts of the inversion technique. Relaxing the stabilization (decreasing the damping) to fit the data between 24° and 30° causes the solution to become slightly unstable in the the upper 300 km. These instabilities can be reduced by weighting the model parameters differently (i.e. using a different model norm, Jordan, 1973). Another artifact occurs between 810 and 840 km because the velocity structure is fixed below 840 km.

We, therefore, smooth the velocity structure in the upper 300 km and below 810 km, and iterate the inversion procedure once more. The resulting model is

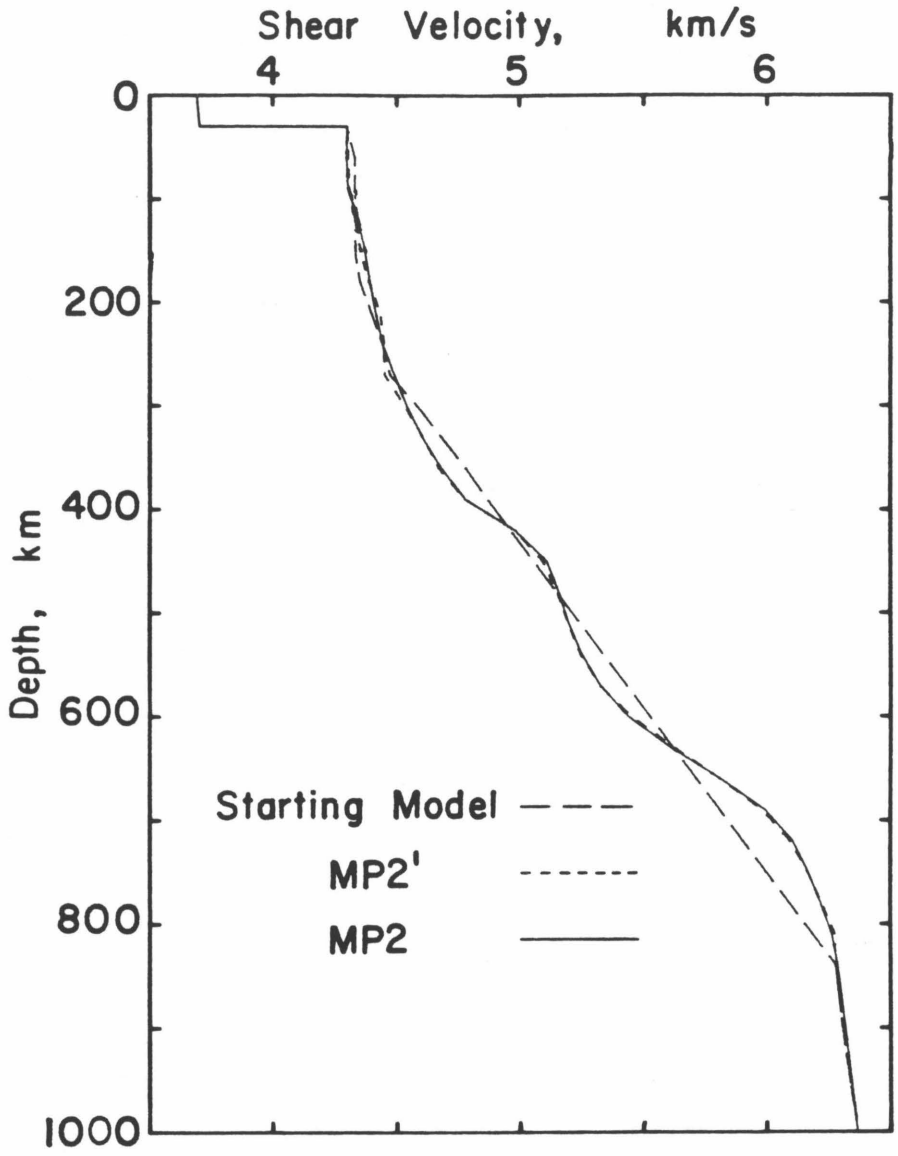

Figure 4.7 Starting model and models MP2' and MP2 resulting from inversion of waveform data and travel times appropriate for model TNA.

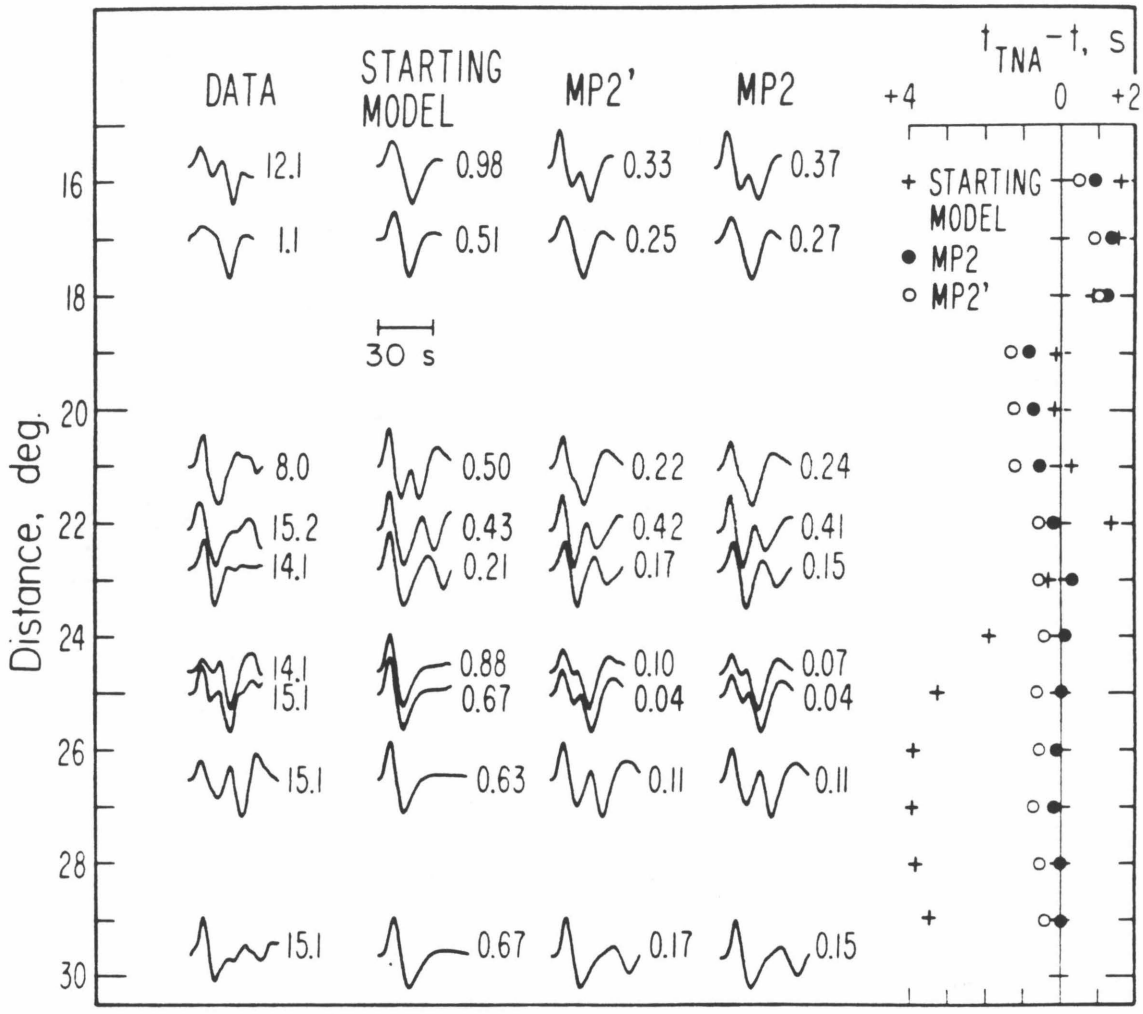

Figure 4.8 Comparison of the observed seismograms and travel times for model TNA with the synthetic seismograms and computed travel times for models MP2' and MP2. The number accompanying each seismogram is proportional to the squared difference between the observed and synthetic seismograms..

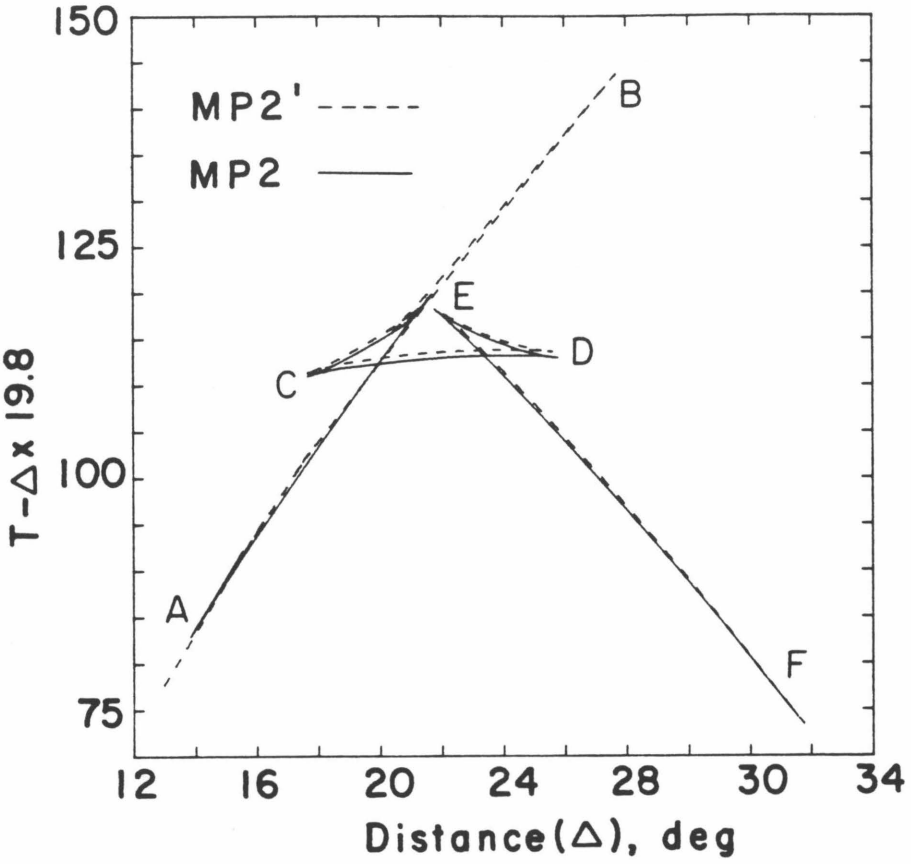

Figure 4.9 Travel time curve for models MP2' and MP2. The prolonged AB branch in MP2' is not well constrained by the data. Model MP2 was obtained by smoothing the structure above 360 km thereby eliminating this branch with little effect on the agreement between observed and synthetic waveforms.

MP2 shown in Figures 4.7, 4.8, and 4.9. Model MP2 is not quite as good a fit as MP2' to the waveform data, however, the differences are probably not important judging, subjectively, from the waveforms in Figure 4.2. The travel times agree well with those for TNA beyond 23°. From 19° to 23°, our model is about .6 s slow and, at nearer distances, model MP2 is about 1 s faster than TNA. These differences are negligible considering the observational errors in travel time and considering the known variations in the uppermost mantle structure.

As discussed above, there are large differences between the observed shear wave travel times observed in the western U.S. and the travel times predicted by TNA based on SS-S differential times. We will now investigate how this discrepancy will affect our velocity models. We now assume that the travel times are 4.5 s faster than those predicted by TNA between 15° and 18°, 3 sec faster at 19° decreasing to 2 sec faster at 23°, and 1 sec fast beyond 23°. Using these travel times and a modification of the starting model used previously, we repeat the inversion procedure. After 15 iterations, we obtain model MP3' shown in Figure 4.10. A summary of the resulting waveforms and travel times are shown in Figure 4.11.

MP3' is similar to MP2 below 450 km but the discontinuity around 400 km appears to be shallower in MP3'. To test whether these differences in fine structure around 400 km are resolvable, we modify MP3' between 360 and 450 km to be the same as MP2, smooth the upper 300 km of MP3', and repeat the inversion. The result, model MP3.1, is also shown in Figures 4.10 and 4.11. The only modification after 3 iterations is an incease in the velocity between 420 and 480 km. This feature is introduced solely in order to fit the travel times from 19° to 23°. We reinvert the data once more, relaxing the travel time constraints and

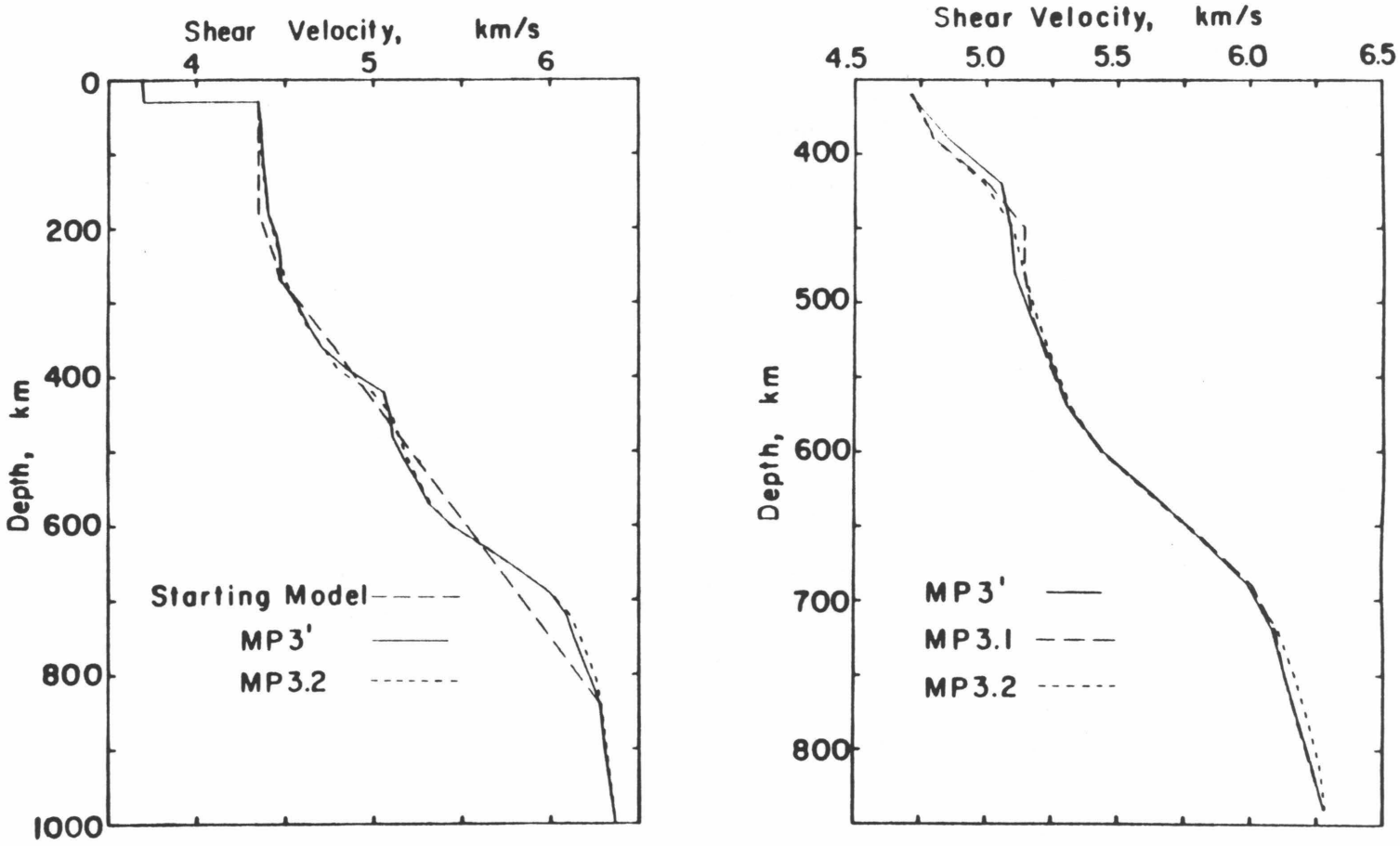

Figure 4.10 a) Comparison of starting model, model MP3' and model MP3.2. b) Comparison of models MP3', MP3.1 and MP3.2.

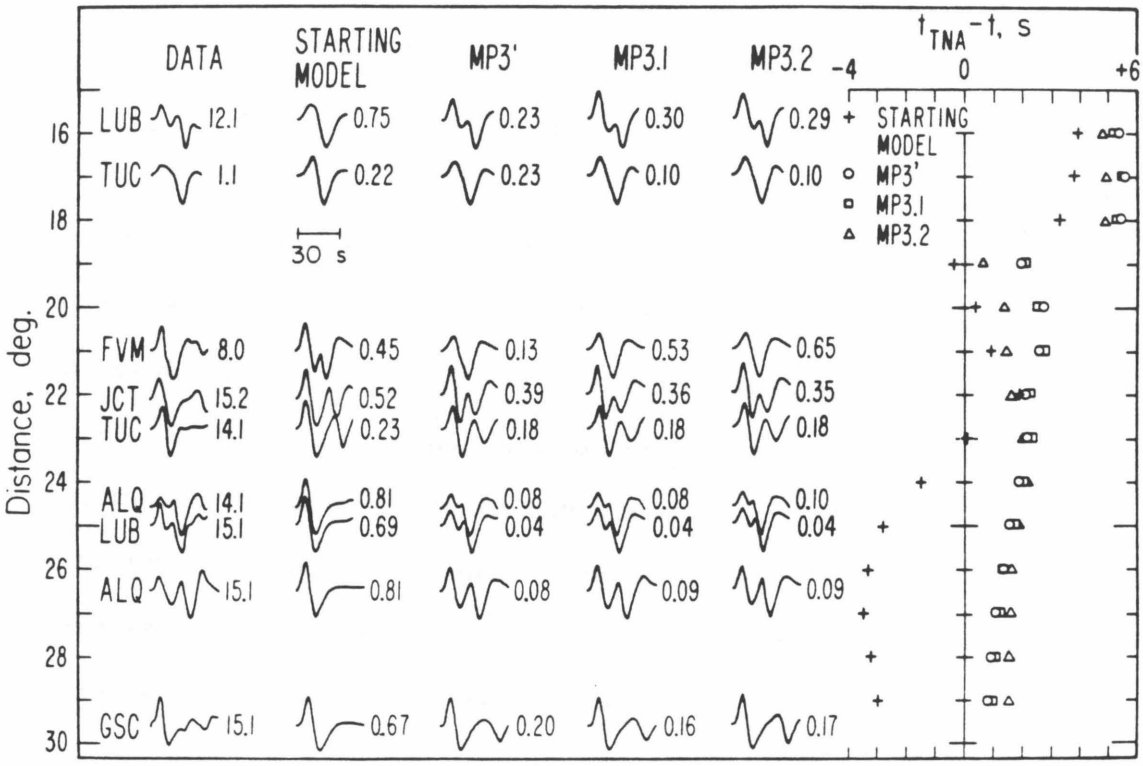

Figure 4.11 Comparison of data and synthetics for models MP3', MP3.1 and MP3.2.

completely replacing the structure in MP3' by that of MP2 below 390 km depth. The resulting model MP3.2 is summarized in Figures 4.10 and 4.11. In all these models the fit of the observed waveforms to the synthetics is similar. The major differences are in the predicted travel times between 19° and 22° and, as discussed earlier, the travel times in Figure 4.4 are not very reliable beyond 20°.

The WKBJ approximation used in the inversion algorithm has been tested extensively against more accurate methods: generalized ray theory and reflectivity, (Fuchs and Muller, 1971) and, therefore, we know that artifacts are present in the synthetics that need to be checked before finally concluding that our models are appropriate. A calculation of synthetic seismograms by the reflectivity method (Fuchs and Muller, 1971) for model MP2 shows generally excellent agreement with the seismograms generated using the WKBJ assumptions except at distances off the ends of cusps in the travel time curve (triplications).

Figure 4.12 shows a profile of synthetics from 23° to 30° computed by the two methods for model MP2 along with the relevent data. The second arrival at distances beyond about 25° is larger in the WKBJ profile than in the reflectivity profile for model MP2. The travel time for the CD and EF branches for MP2 is shown in Figure 4.13. The D cusp occurs at about 25°. For distances less than 25° the WKBJ approximation is expected to be accurate; at further distances the diffracted arrival is not well modeled. In the WKBJ seismograms, the amplitude of the second arrival does not decay with distance as quickly as it should as indicated by the reflectivity seismograms. Because we are using records at 26.5° and 29.6°, an inversion procedure converges to a point where these observations were fit equally well. The second arrivals are somewhat too large at 29.6° and

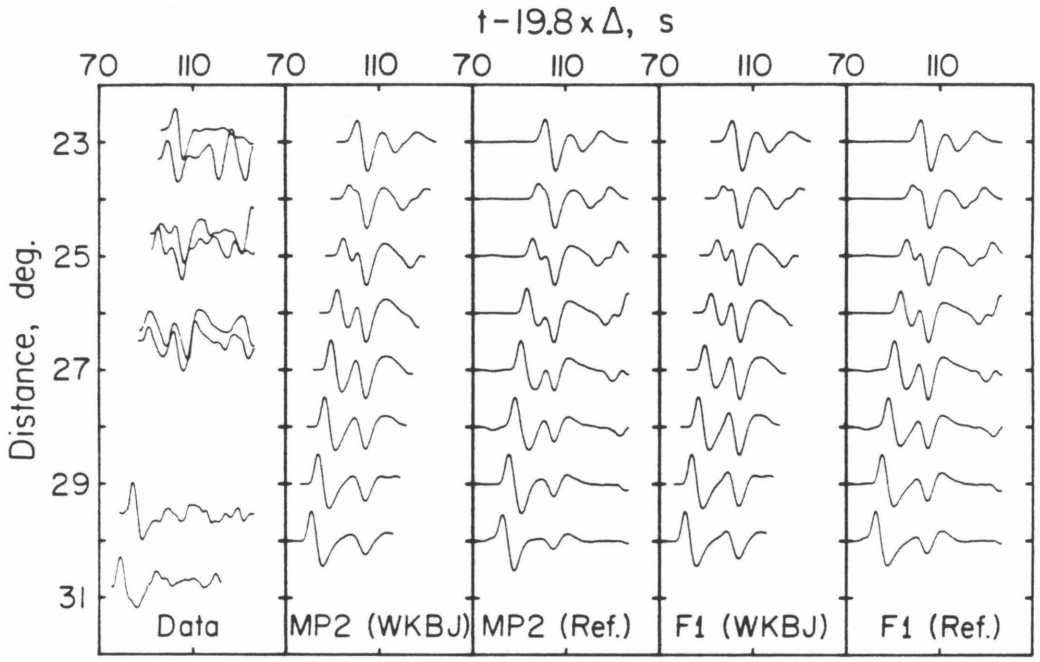

Figure 4.12 Comparison of data between 22° and 30° and synthetic profiles for models MP2 and F1 generated by the WKBJ and reflectivity method. The decay in amplitude of the latter arrival relative to the first arrival is fit better with model F1 as judged by inspecting the profiles computed using reflectivity.

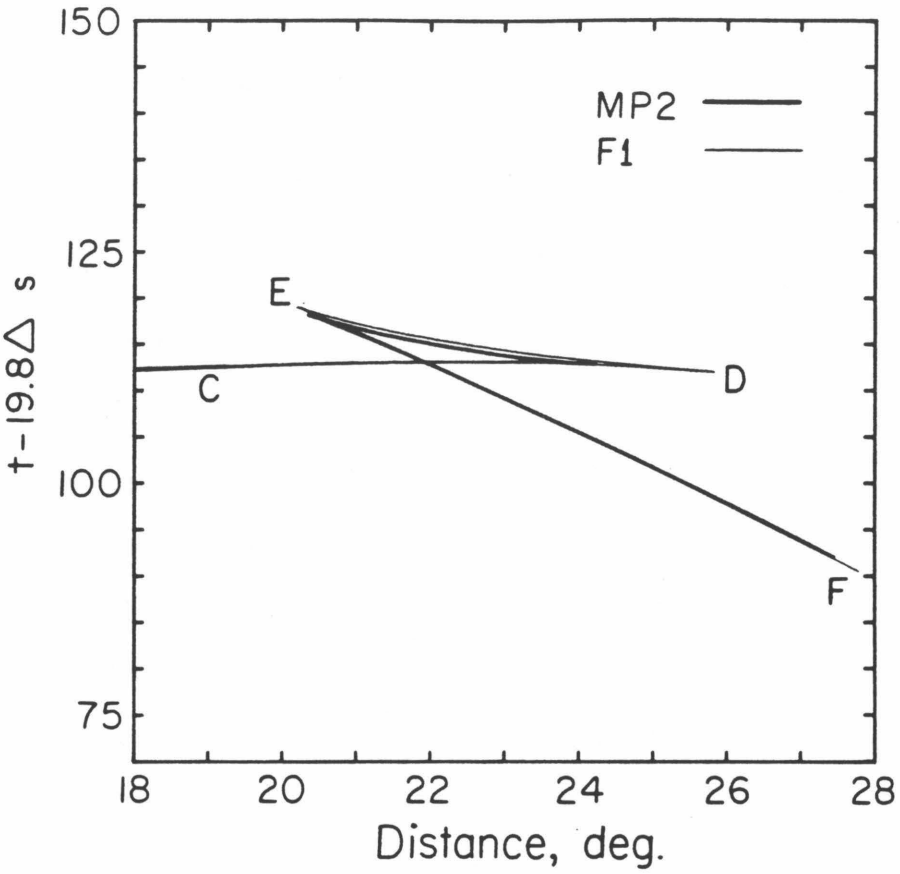

Figure 4.13 Travel time curves showing only the CD and EF branches for models MP2 and F1. Modifying the structure between 570 and 750 km causes the CD branch to extend to greater distances.

slightly too small at 26.5°.

To correct the model MP2 for this artifact in the modelling technique we remove from consideration the GSC record at 29.6°, fix the velocity above 540 km; and invert the data between 22.1° and 24.6° using MP2 as the starting model. The resulting model F1 (Figure 4.14) produces some improvement in the agreement between data and synthetics, particularly at the distance of 26.5°.

The velocity model F1 shows that the large increase in velocity from 600 to 750 km is sharper than in model MP2. The effect of this difference is to push the position of the D cusp to 26° (see Figure 4.13). Our subjective assessment of the fit between the data and synthetics is that F1 is a better estimate of the velocity structure than MP2 although obviously from Figure 4.14 the differences are slight. The velocity model F1 is given in Table 4.2, another model F2, Table 4.3 was derived in a similar way from model MP3.2.

The 400 km discontinuity in models MP3.2 and MP2 is modeled as a high velocity gradient between 390 km and 420 km. Although, using long-period body waves, we do not expect to be able to resolve any discontinuities sharper than this, we investigate whether the model proposed by Grand and Helmberger (1983) can be modified to fit the data in a resolvably better way. We also estimate the effect of a shallow high velocity lid on the inversion.

Starting with model TNA, we find that perturbing the model slightly can indeed increase the amplitude of the arrival from below 400 km relative to the first arrival at 15.7° (Figure 4.15). The new model is designated TNA.M and is shown in Figure 4.16. We note that there is again some tradeoff between how well we can match the observations at less than 17° and still fit the data beyond 22°. Removing the lid in TNA results in synthetics that fit only slightly better than

Table 4.2 Velocity Model F1

Velocity	Depth
3.690	0.0
3.690	6.0
3.700	30.0
4.350	30.0
4.350	33.0
4.358	60.0
4.363	90.0
4.374	120.0
4.390	150.0
4.405	180.0
4.440	210.0
4.474	240.0
4.501	270.0
4.559	300.0
4.621	330.0
4.714	360.0
4.799	390.0
4.991	420.0
5.108	450.0
5.156	480.0
5.196	510.0
5.249	540.0
5.292	570.0
5.413	600.0
5.595	630.0
5.802	660.0
6.003	690.0
6.122	720.0
6.180	750.0
6.228	780.0
6.270	810.0
6.289	840.0
6.320	870.0
6.315	900.0
6.365	1000.0

Table 4.3 Velocity Model F2

Velocity	Depth
3.690	6.0
3.700	30.0
4.300	30.0
4.300	33.0
4.297	60.0
4.302	90.0
4.337	120.0
4.370	150.0
4.389	180.0
4.414	210.0
4.441	240.0
4.488	270.0
4.540	300.0
4.601	330.0
4.677	360.0
4.775	390.0
4.978	420.0
5.108	450.0
5.156	480.0
5.196	510.0
5.249	540.0
5.292	570.0
5.413	600.0
5.595	630.0
5.802	660.0
6.003	690.0
6.122	720.0
6.180	750.0
6.228	780.0
6.270	810.0
6.289	840.0
6.302	870.0
6.315	900.0
6.365	1000.0

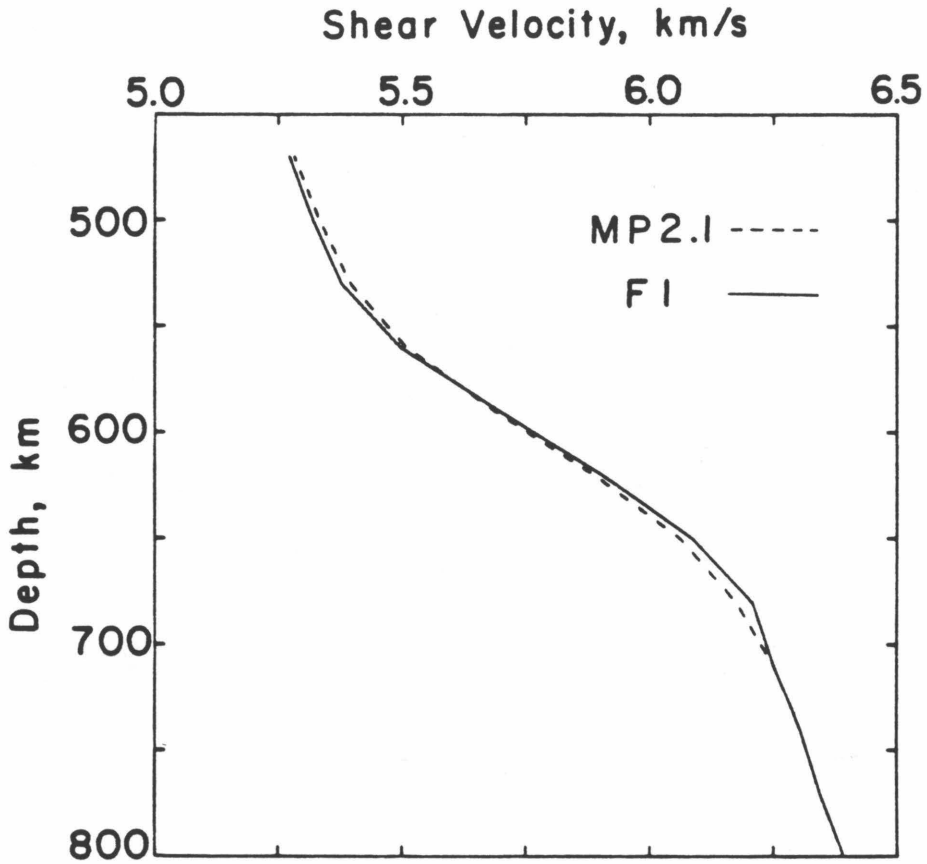

Figure 4.14 A comparison of differences between model MP2 and F1. The models are identical above 540 km. The differences are slight but produce significant changes in the waveforms in Fig. 4.12.

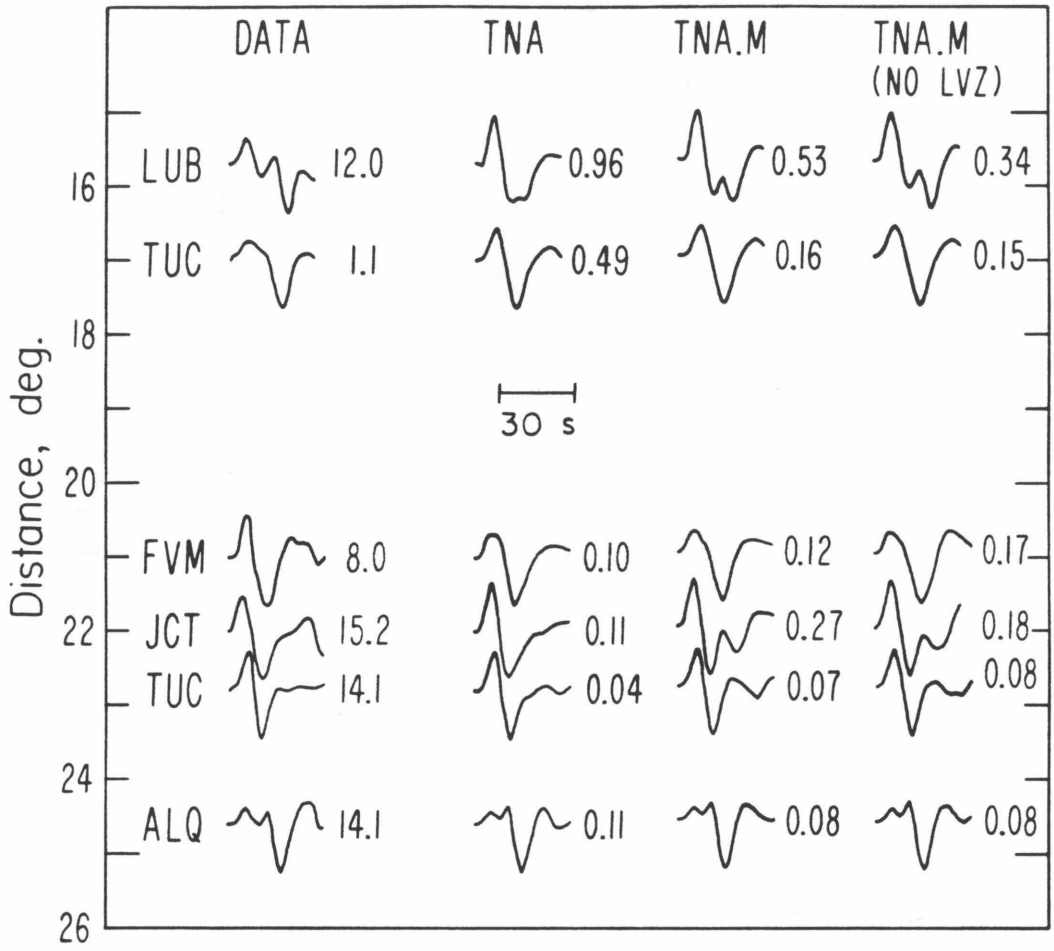

Figure 4.15 Comparison of synthetics from models TNA.M and TNA.M(no LVZ) derived by perturbing TNA to better fit the data between 15° and 22°.

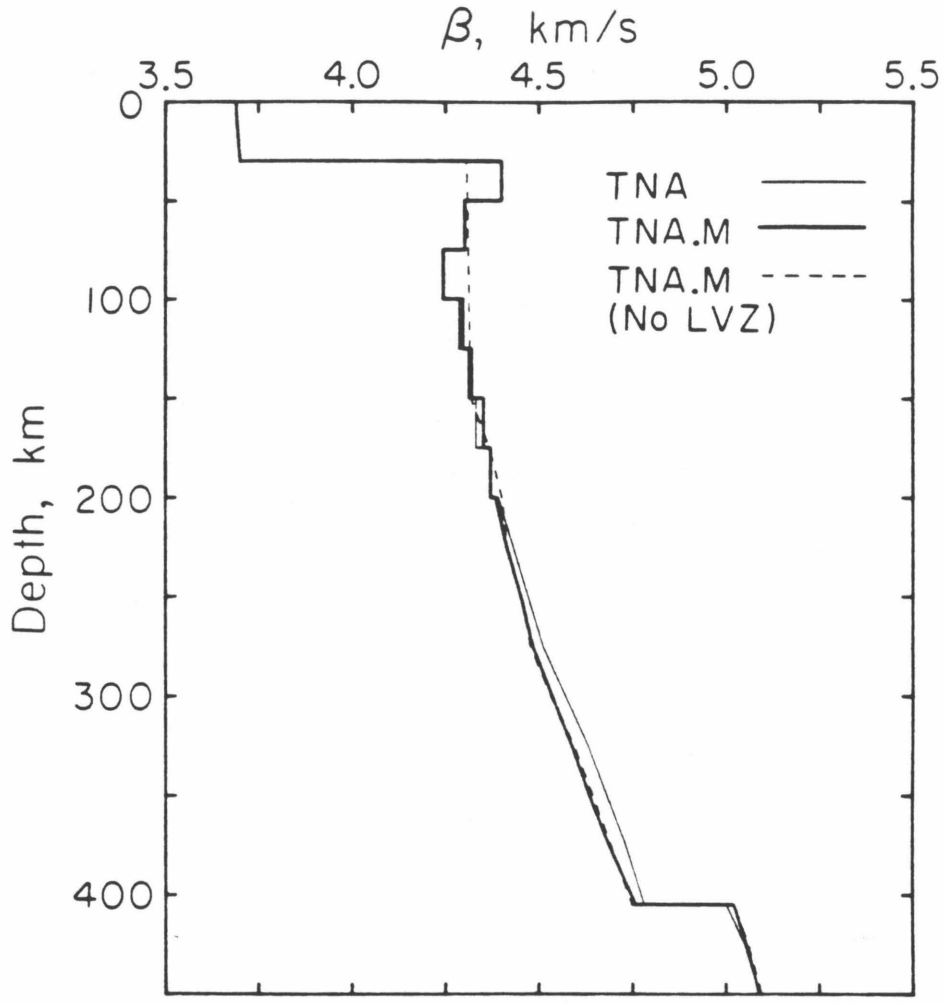

Figure 4.16 Models TNA, TNA.M and TNA.M (no LVZ) derived from inversion result shown in Figure 4.15.

model TNA.M indicating that the presence of the lid and the low velocity zone is not resolvable from our data and has little effect on resulting velocity models.

4-6 Discussion

The experiments with an iterative inversion scheme for body-wave seismograms that we have conducted should give some indication of the usefulness of this data for constraining the velocity structure. In our first three experiments we derive velocity models from starting models that are obviously not accurate even as initial guesses. The reasoning behind this is to try to find the simplest upper mantle model which could satisfy the data. The resulting models are quite similar in general features: a small overall velocity gradient from 50 to 250 km; an increase in gradient below 250 km resulting in about a 4% velocity by 360 km depth; a large velocity gradient between 360 km and 420 km with cumulative velocity increase of around 8½%; a 5 % increase in velocity from 420 km to 600 km; and a 14 % increase in velocity between 600 and 750 km.

The depths to regions of high velocity gradients, the 400 km and 600 km "discontinuities", are constrained by the travel times used in the inversion. In our initial test, the travel times are essentially those of the starting model and are about 4 s faster than TNA at 16° and 4 s slower than TNA at 30°. In deriving MP2 we use TNA travel times, and in deriving MP3', MP3.1 and MP3.2 we fit travel times which are systematically faster than TNA as suggested (but not demanded) by the travel time data. A review of Figures 4.5 and 4.10 reveals that there is about a 20 km difference in the depth to the major discontinuities resulting from these different travel time assumptions. Of course the absolute depth to these discontinuities is also very dependent on the structure assumed

for the uppermost mantle.

In Figure 4.17 we summarize these velocity models that fit the waveform data. Figure 4.18 shows the travel time curves for the three models. We note that TNA.M is slightly later than F1 (about 1 s) as a result of the low velocity zone. F1 and F2 were constructed to be essentially the same below 390 km. Recalling the waveform data used in the inversion, inspection of the travel time curve in Figure 4.18 is enlightening as to how the automated inversion procedure converges. The velocity gradient between 360 km and 450 km was modified by the amount needed to introduce the second arrival at 15.7°. Including clear observations of a second arrival at closer distances would increase the resolution of structure in this depth range. Note that if the velocity increase was truly discontinuous at 405 km, a second arrival should be observable to at 13°. Data at these distances are difficult to interpret due to the arrival of the Love wave. Our modeling procedure assumes that we can explain all the feature in the waveforms by direct arrivals of bodywaves.

The final comparison between synthetic and observed profiles is shown in Figure 4.19. Here we have taken data from both source regions for distances less than 21°. Beyond 21° the sources are located on the East Pacific Rise. The combined data set gives some idea of the variability in the waveforms and the quality of the overall fit. Synthetics are computed for model F1 by both the reflectivity and WKBJ techniques. The WKBJ method yields excellent results except at distances greater than 27° as noted earlier.

The inability to better fit the data at the distances of 15° to 17° is puzzling. Better agreement between data and synthetic seismograms is possible as in, for example, the experiment described in Figures 4.5 and 4.6, but at the expense of

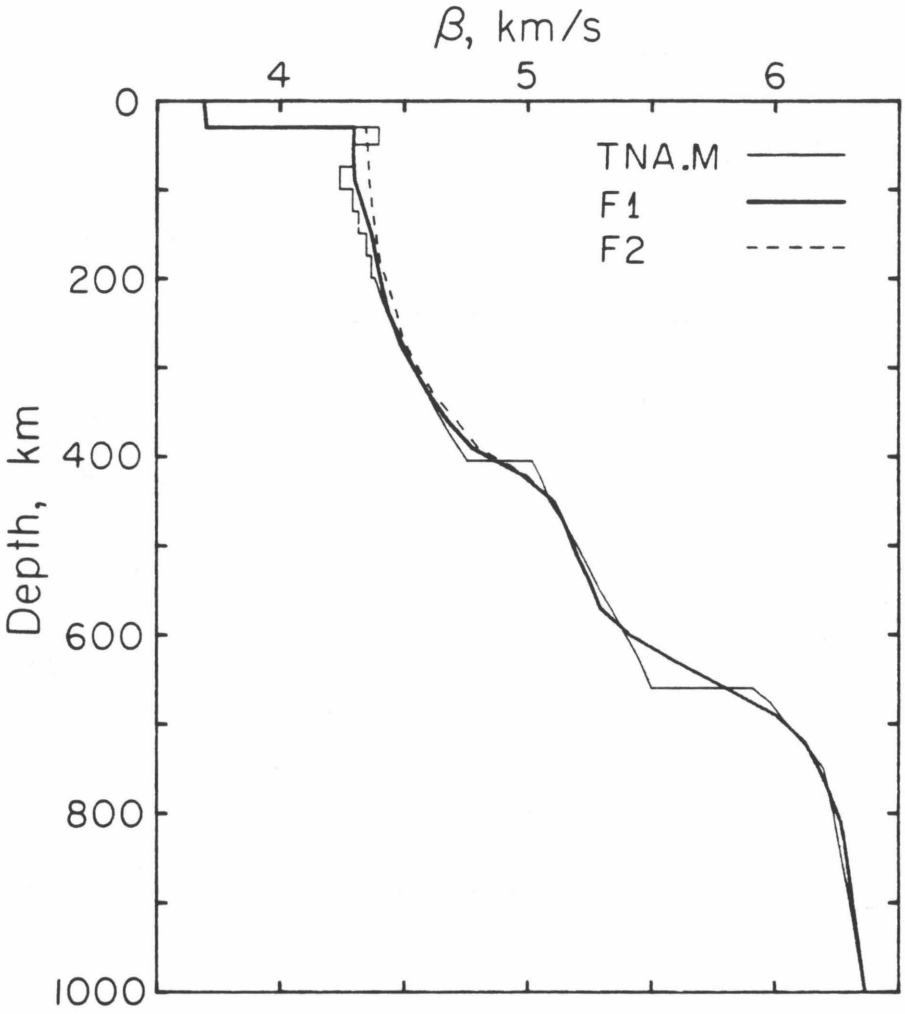

Figure 4.17 Comparison of models TNA.M, F1 and F2.

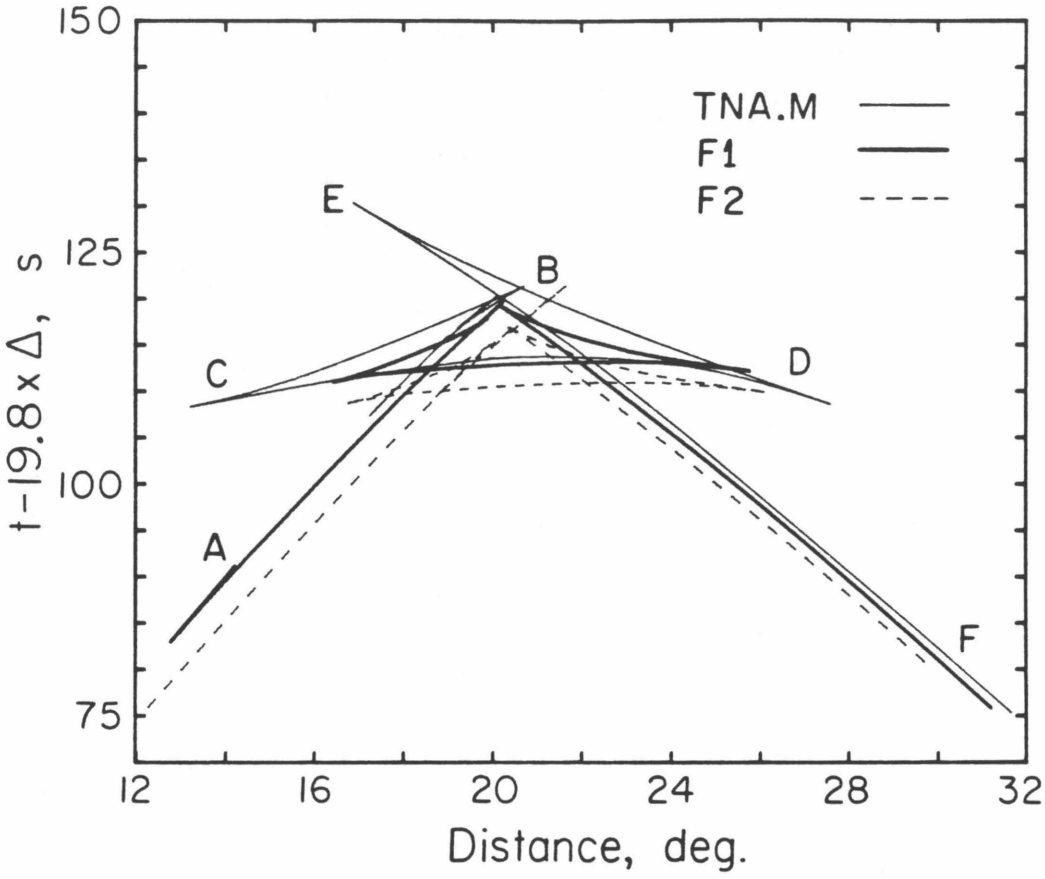

Figure 4.18 Comparison of travel times for models TNA.M, F1 and F2.

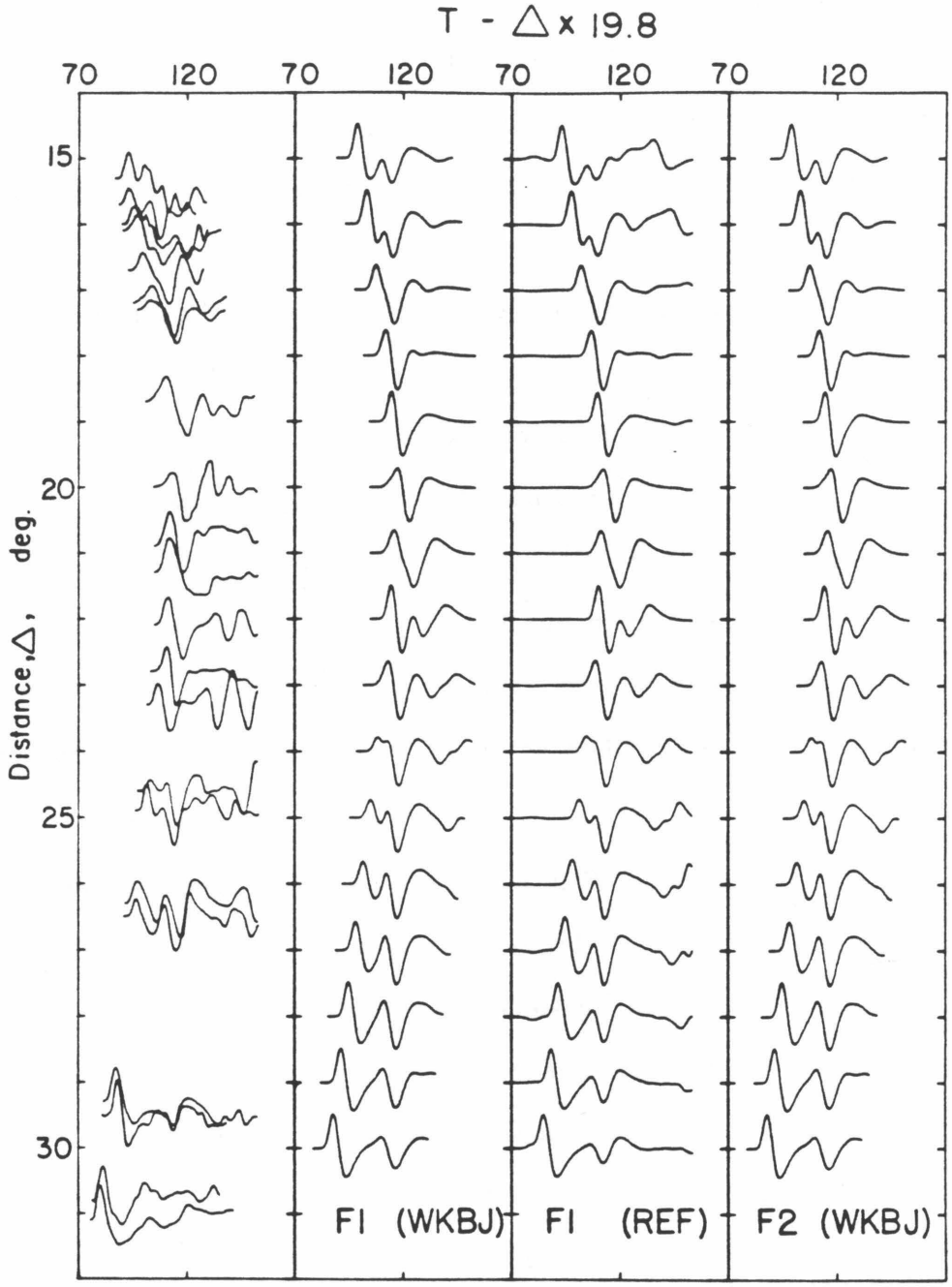

Figure 4.19 Profile of selected data from Figure 4.2 compared with synthetics for models F1 and F2. Data from both profiles in Figure 4.2 are included for at distances less than 21°. Synthetics for model F1 are shown computed using both the reflectivity method and the WKBJ method to illustrate the accuracy of the WKBJ technique for computing synthetic seismograms.

the fit beyond 22°. This observation may indicate that our velocity models or wave propagation calculations are too simple. Grand and Helmberger (1983) note that multiple reflections from the surface such as SS, SSS, etc. follow the S phase closely at distances of less than 20° and, in some cases interfere with the arrival from below the 400 km discontinuity. The arrival that we interpret as coming from below 400 km is observable and quite consistent in Figure 2.2. and moves forward in the record suggesting that contamination by multiple phases is minimal. Another possibility is that attenuation may be more important than we have assumed. Considering the extent of the lateral heterogeneity that may be present in the upper 200 km of the mantle, we consider the agreement between the synthetics at these distances to be reasonable. Another useful feature of an inversion algorithm is the ability to easily detect inconsistencies such as these.

We also note that the data shown in Figures 4.2 and 4.19 are qualitatively similar to the P-wave seismograms recorded in southern California from events in Mexico and on the East Pacific Rise investigated by Walck (1983). A similar AB branch is observed in the P waves and ends at about 20° suggesting an increase in the compressional wave velocity gradient around 250 km. Walck (1983) has excellent observations of the triplication arising from the 660 km discontinuity and suggests that the large velocity increase occurs between 620 and 680 km with a sharp discontinuity at 660 km. The data we present do not place much constraint on the sharpness of the discontinuity; the models in Figure 4.18 fit the data equally well. We do feel that both discontinuities must be at least as sharp as they are in our models F1 or F2.

The results of this study are in disagreement with the conclusions of some previous investigators. Cara (1978) presented a shear velocity model based on measurements of the dispersion of fundamental and higher-mode Rayleigh waves in the western U.S. His data suggested high velocities (4.43 km/s) below the Moho decreasing to very low velocities (4.05 km/s) at 100 km. Wielandt and Knopoff (1982) derived a similar model for the East Pacific Rise based on very long-period observations of fundamental mode Rayleigh waves propagating between the South Pole and California. The low velocity zone that these authors have proposed would almost certainly affect our observations. Travel times predicted by these models are at least 15 s slower at distances less than 20° which would be evident, even with our poor quality travel time data. The resolution of this discrepancy requires futher study. Anderson and Dziewonski (1982) proposed that the upper 200 km of the mantle is transversely anisotropic worldwide based on the inability to fit both Love (SH) and Rayleigh (SV) data with a single isotropic model. They emphasized that models derived assuming isotropy (such as in the present study as well as in Cara (1978)) could be substantially in error. The discrepancy between our results (SH) and those of Cara (1978) (SV) may be a manifestation of this phenomenon. The best way to investigate the possibility of anisotropy is to analyze SV waves in a manner similar to the way that we have treated SH waves.

The resolving power of the data set used in the body wave inversion can be estimated from Figure 4.20. A correction to any model parameter is actually a weighted average of the corrections to all of the model parameters. The details of the averaging at each depth be represented by "averaging kernels" shown in Figure 4.20. The shape of the averaging kernels is controlled through the

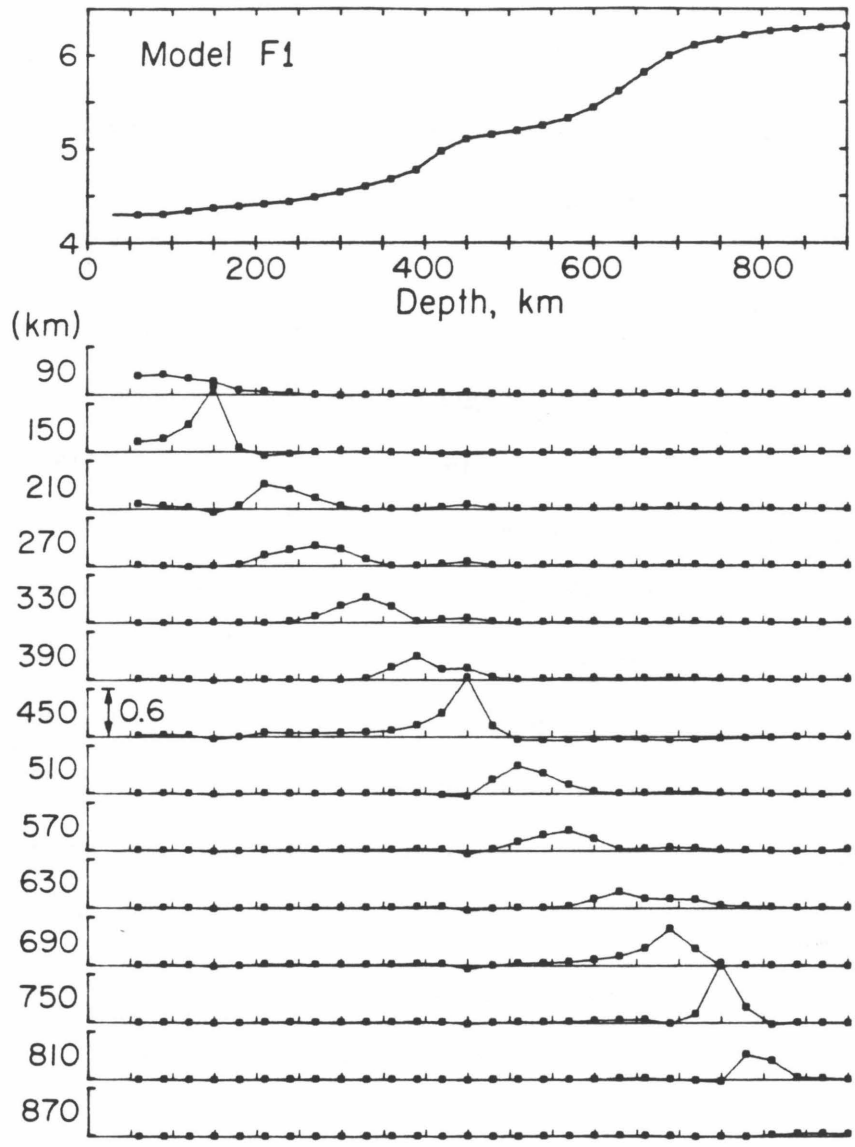

Figure 4.20 Averaging kernels computed for model F1. The horizontal axis for each depth is the same as the velocity axis at the top.

stabilization (see Wiggins, 1972) by both the errors assigned to the data and by the desired accuracy for the corrections to the parameters. We heavily stabilize (damp) the inverse in the initial stage of an inversion and relax the damping as we approach convergence. Figure 4.20 is computed for the damping used in the final iteration for model F1. The details for the other models vary slightly.

The inversion technique is very nonlinear so Figure 4.20 is, in no way, meant to represent the resolving power throughout the iterative process. However we can use Figure 4.20 to estimate the lengths over which the various features of the model are resolvable. For example the data appear to be providing detailed information about the velocity structure around 150 km, 420-500 km and 700-800 km. Details concerning the sharpness of the discontinuities are not obtainable as seen in the averaging kernels for depths between 570 and 700 km and around 390 km. These conclusions are intuitively reasonable since we lack the detailed waveform data necessary to accurately locate the cusps of the travel time curve, information that is needed to resolve these features better.

The primary purpose of the study is to interpret S-waves observed in the western U.S in terms of the radial variation in velocity. In addition we test a scheme for inverting the observed seismograms directly, using travel time constraints. We feel that this method holds promise for further structural studies in which detailed waveform analysis is required. For much of the world this type of data is the only source of information relevant to the fine structure of the upper mantle. The procedure of trial and error fitting of theoretical seismograms to observations is much too time consuming to be practical in many situations. An inversion scheme can relieve much of the tedium and frustration by quickly identifying those observations which are inconsistent and by

performing the final perturbations necessary to explain the data, although an inversion algorithm is no substitute for lack of a detailed understanding of the wave propagation phenomena under observation.

4.7 Conclusions

S-wave body phases recorded in the Western U.S. from events in Oregon, California, the Gulf of California, and the East Pacific Rise show good evidence for two major triplications between 15° and 30°. Direct inversion of the seismograms with travel time constraints indicate that there are two major regions of high velocity gradient in the upper mantle. One is an 8½% increase in velocity between 360 km and 420 km depth, and the other, a 14% increase between 600 and 750 km. The overall velocity increase in the uppermost 200 km appears to be small with an increase in the gradient at around 270 km. The cumulative velocity increase between 270 and 360 km is about 4%. The velocity gradient between 420 and 600 km results in a velocity increase of 6% over these depths. The data cannot resolve discontinuities sharper than these; models with true discontinuous increases in velocity, such as TNA (Grand and Helmberger, 1983), are acceptable fits to the data.

S-wave travel times in the western U.S. differ from those predicted on the basis of SS-S differential times (Grand and Helmberger, 1983) by as much as 5 s at distances of less than 19°. The resolvable discrepancy in the data sets can be satisfied by velocity differences in the upper 120 km of about 1% and by differences in velocity of about ½% down to 390 km. These data can both be satisfied by the same velocity structure below 390 km.

Our results are very consistent with the shear-wave model, TNA, proposed by Grand and Helmberger (1983) and with the P-wave model of Walck (1983). There appear to be large discrepancies between models derived from Rayleigh wave data and models derived from observations of SH body waves.

4.8 References

Anderson, D. L. and A. M. Dziewonski, 1982, Upper mantle anisotropy: evidence from free oscillations, *Geophy. J. R. Astr. Soc.*, *69* , 383-404.

Backus, G. E. and J. E. Gilbert, 1967, Numerical application of a formalism for geophysical inverse problems, *Geophys J. R. Astr. Soc.*, *13* , 247-276.

Backus, G. E. and J. E. Gilbert, 1968, The resolving power of gross earth data, *Geophys. J. R. Astr.*, *16*, 169-205.

Backus, G. E. and J. F. Gilbert, 1970, Uniqueness in the inversion of inaccurate gross earth data, *Phil. Trans. Roy. Soc. London, Sec A, 266* , 123-192.

Burdick, L.J. and C.A. Langston, 1977, Modelling crustal structure through the use of converted phases in teleseismic body waveforms, *Bull. Seis. Soc. Am.*, *66*, 677-691.

Burdick, L.J., and D.V. Helmberger, 1978, The upper mantle P-velocity structure of the western United States, *J. Geophys. Res.*, *83*, 1699-1712.

Cara, M., (1979), Lateral variations of S velocity in the upper mantle from higher Rayleigh modes, *Geophys. J. R. astr. Soc. 57*, 649-670.

Chandra, U., 1974, Seismicity, earthquake mechanisms, and tectonics along the western coast of North America, *Bull. Seism. Soc. Am.*, *64* , 1529-1549.

Chapman, C. H., 1978, A new method for computing synthetic seismograms, *Geophys. J. R. Astr. Soc.*, *54* , 481-518.

Dean, B. W. and C. L. Drake, 1978, Focal mechanism solutions and tectonics of the middle America arc, *Jour. Geol.*, *86* , 111-128.

Dziewonski, A. M. and D. L. Anderson, 1981, Preliminary reference earth model, *Phys. Earth Planet. Int.*, *25* , 297-356.

Dziewonski, A.M., B.H. Hager, and R.J. O'Connell, 1977 Large-scale heterogeneities in the lower mantle, *J. Geophys. Res.*, *82* 239-255.

Dziewonski, A.M., and J.M. Steim, 1982, Dispersion and attenuation of mantle waves through waveform inversion, *Geophys. J. R. astr. Soc. 70*, 503-527.

Fuchs, K. and G. Muller, 1971, Computation of synthetic seismograms with the reflectivity method and composition with observation, *Geophy. J. R. Astr. Soc.*, *23*, 417-433.

Futterman, W. I., 1962, Dispersive body waves, *J. Geophys. Res.*, *67*, , 5279-5291.

Grand, S. P. and D. V. Helmberger, 1983, Upper mantle shear structure of North America, *Geophys. J. R. Astr. Soc.* (in press).

Helmberger, D. V., 1968, The crust mantle transition in the Bering Sea, *Bull. Seis. Soc. Am.*, *58*, 179-214.

Helmberger, D. V. and G. R. Engen, 1974, Upper mantle shear structure, *J. Geophys. Res.*, *19*, 4017-4028.

Ibrahim, A. K. and O. W. Nuttli, 1967, Travel time curves and upper mantle structure from long period S waves, *Bull. Seis. Soc. Am.*, *57*, 1063-1092.

Jordan, T. H., 1973, Estimation of the radial variation of seismic velocities and density in the Earth., *Ph.D. Thesis, California Institute of Technology.*

Kovach, R. L. and R. Robinson, 1969, Upper mantle structure in the basin and range province, western North America, from apparent velocities of S-waves, *Bull. Seis. Soc. Am.*, *59* , 1653-1665.

Langston, C.A., 1977 The effect of planar dipping structure on source and receiver for constant ray parameter, *Bull. Seis. Soc. Am.*, *67*,1029-1050.

Lay T., 1983, Localized velocity anomalies in the lower mantle, *Geophys. J. R. Astr. Soc.*, *72* , 483-516.

Lay, T., and D.V. Helmberger, 1983, A lower mantle S-wave triplication and the shear velocity of D'', *Geophys. J. R. astr. Soc.*, submitted

Lernar-Lam, A. L. and T. H. Jordan, 1983, Earth structure from fundamental and higher mode wavefrom analysis, *Geopyhs J. R. Astr. Soc*, (in press).

Mellman, G. R. (1980), A method of body-wave waveform inversion for the determination of earth structure, *Geophys. J. R. Astr. Soc.*, *62*, 481-504.

Molnar, P. and L. R. Sykes, 1969, Tectonics of the Caribbean and Middle America regions from focal mechanisms and seismicity, *Bull. Geol. Soc. Am.*, *80*, 1639-1684.

Nakanishi, I., 1981, Shear velocity and shear attenuation models inverted from world-wide and pure-path average data of mantle Rayleigh waves (${}_0S_{25}$ to ${}_0S_{80}$) and fundamental spheroidal modes (${}_0S_2$ to ${}_0S_{24}$), *Geophys. J. R. astr. Soc.*, *66*, 83-130.

Nuttli, O. W., 1969, Travel times and amplitudes from nuclear explosions in Nevada, *Bull. Seis. Soc. Am.*, *59*, 385-398.

Robinson, R. and R. L. Kovach, 1972, Shear wave velocities in the Earth's mantle, *Phys. Earth Planet. Int.*, *5* , 30-44.

Walck, M. C., 1983, The P-wave upper mantle structure beneath an active spreading center: the Gulf of California, *Geophys. J. R. Astr. Soc.*, (submitted).

Wallace T. C., 1983, Long period regional body waves, Ph.D. Thesis California Institute of Technology.

Weilandt, E. and L. Knopoff, 1982, Dispersion of very long-period Rayleigh waves along the East Pacific Rise: evidence for S-wave velocities anomalies to 450 km depth, *J. Geophys. Res.*, *87*, 8631-8641.

Wiggins, R. A., 1972, The general linear inverse problem: implication of surface waves and free oscillations for earth structure, *Reviews of Geophys. and Space Phys.*, *10*, 251-285

Wiggins, R. A. and D. V. Helmberger, 1974, Synthetic seismogram computation by expansion in generalized rays., *Geophys. J. R. Astr. Soc.*, *37*, 73-90.

Woodhouse, J. H., 1983, The joint inversion of seismic waveforms for lateral variations in earth structure and earthquake source.,

Proceedings of the International School of Physics, " Enrico Fermi ", Vol LXXXV, H. Kanamori and E. Boschi, eds, North Holland, Amsterdam (in press).

Appendix

A-1 Computation of $\partial u^{WKB}(\omega)/\partial v_j$

From eq. (3.22) we have

$$\frac{\partial u^{WKB}}{\partial v_j} = -\omega^2 S_o(\omega)\sqrt{\frac{\pi}{\omega}}e^{-i\pi/4} \tag{A.1}$$

$$\left\{\int_{p_1}^{p_2} F_{RS}(p)\frac{\partial R(p)}{\partial v_j}e^{-i\omega(pr+\tau(p))}dp\right.$$

$$\left.-i\omega\int_{p_1}^{p_2} F_{RS}(p)R(p)\frac{\partial \tau(p)}{\partial v_j}e^{-i\omega(pr+\tau(p))}dp\right.$$

Here we will be concerned with the details of the evaluation of the function of p, $\partial R(p)/\partial v_j$ and $\partial \tau(p)/\partial v_j$.

The function $\partial R(p)/\partial v_j$ depends on the transmission coefficients required by discontinuities in the velocity structure. These transmission coefficients have the same form as the transmission coefficients in generalized ray theory and we will defer their derivation until later.

Before proceeding we will consider a particular velocity parameterization. We will sample the velocity structure at discrete intervals and assume that the velocity varies linearly with depth between the sampled points. The parameterization is sufficiently general for the application of modeling the upper mantle

and yet is simple enough to permit easy evaluation of the function $\tau(p)$.

The function $\tau(p)$ is given by

$$\tau(p) = \int_0^{z_s} \eta dz + 2\int_{z_s}^{z_0} \eta dz + 2\int_{z_0}^{z_1} \eta dz + \cdots 2\int_{z_k}^{z_p} \eta dz. \tag{A.2}$$

where $\eta=(1/v^2(z)-p^2)^{1/2}$, z_s is the source depth and z_p is the depth at which $1/v(z_p)=p$. z_p lies between z_k and z_{k+1} ($z_k<z_p<z_{k+1}$). Using our parameterization, each integral in (A.2) can be evaluated directly. For example the contribution to τ from the integral from z_n and z_{n+1}, $n+1\leq k$ is

$$J_n = 2\int_{z_n}^{z_{n+1}} \eta dz \tag{A.3}$$

$$= 2/b_n \left\{ \sqrt{1-p^2v_n^2} - \sqrt{1-p^2v_{n+1}^2} + \log\left[\frac{v_{n+1}}{v_n} \left[\frac{1-\sqrt{1-p^2v_n^2}}{1-\sqrt{1-p^2v_{n+1}^2}} \right] \right] \right\}$$

where

$$b_n = \frac{v_{n+1}-v_n}{z_{n+1}-z_n} \tag{A.4}$$

For the integral from z_k to z_p which includes the turning point we have:

$$J_k = \frac{2}{b_k} \left\{ \sqrt{1-p^2v_k^2} + \log\left[\frac{1}{p\sqrt{v}} \left(1-\sqrt{1-p^2v_k^2} \right) \right] \right\} \tag{A.5}$$

Therefore we can rewrite $\tau(p)$ as

$$\tau = \int_0^{z_s} \eta dz + 2\int_{z_s}^{z_0} \eta dz + J_0 + J_1 + J_2 + \cdots J_k \tag{A.6}$$

and

$$\frac{\partial \tau}{\partial v_i} = \frac{\partial J_{i-1}}{\partial v_i} + \frac{\partial J_i}{\partial v_i} \tag{A.7}$$

The explicit differentiation of (A.3) and (A.5) is straightforward. For $i \leq k$, define Q_i from (A.3) and (A.5) by

$$J_i = \frac{2}{b_i} Q_i \tag{A.8}$$

Then

$$\frac{\partial \tau}{\partial v_i} = \frac{-1}{b_{i-1}} \left(\frac{2}{v_i - v_{i-1}} \right) Q_{i-1} + \frac{1}{b_i} \frac{2}{v_{i+1} - v_i} Q_i \tag{A.9}$$

$$+ 2 \left(\frac{1}{v_i} - \frac{p^2 v_i}{\left(1 - \sqrt{1 - p^2 v_i^2}\right)} \right) \left(\frac{1}{b_i} - \frac{1}{b_{i-1}} \right)$$

and for $i = k+1$

$$\frac{\partial \tau}{\partial v_k} = \frac{-1}{b_k} \frac{1}{v_{k+1} - v_k} Q_k \tag{A.10}$$

A-2 Computation of $\partial u^{GR}(s) / \partial v_j$

From eq. (3.30) we have

$$\frac{\partial u^{GR}(s)}{\partial v_j} = s^2 S_0 \sqrt{\pi / s} \sum_{RAYS} \left\{ \mathrm{Im} \int_0^{i\infty} F_{RS}(p) \frac{\partial R(p)}{\partial v_j} e^{-s(pr+\tau)} dp \right. \tag{A.11}$$

$$\left. - s \, \mathrm{Im} \int_0^{i\infty} F_{RS}(p) R(p) \frac{\partial \tau(p)}{\partial v_j} e^{-s(pr+\tau)} dp \right.$$

Here we will treat v_j as the velocity in the j^{th} layer and investigate $\partial R(p)/\partial v_j$ and $\partial \tau(p)/\partial v_j$ for the SH case.

$R(p)$ is the product of all the transmission and reflection coefficients along the ray path, i.e.

$$R = \prod_{RAY} C_{l\,l+1} \tag{A.12}$$

where C_{l+1} is the appropriate reflection or transmission coefficient describing the interaction between the l and $l+1$ layer. Therefore we need only investigate the derivatives of the reflection and transmission coefficients. Define

$$E_i = \rho_i v_i^2 \eta_i \tag{A.13}$$

where ρ_i is the density of the i^{th} layer and $\eta_i = \sqrt{1/v_i^2 - p^2}$. Then

$$T_{ij} = \frac{2E_i}{E_i + E_j} \tag{A.14}$$

is the transmission coefficient between the i^{th} and j^{th} (an adjacent) layer. Similarly

$$R_{ij} = \frac{E_i - E_j}{E_i + E_j} \tag{A.15}$$

is the reflection coefficient for the i^{th} and adjacent j^{th} layer. Differentiating with respect to v_i and v_j we have

$$\frac{\partial T_{ij}}{\partial v_i} = \frac{2E_j}{(E_i + E_j)^2} \rho_i \left[2v_i \eta_i - \frac{1}{v_i \eta_i} \right] \tag{A.16}$$

$$\frac{\partial T_{ij}}{\partial v_j} = \frac{-2E_i}{(E_i + E_j)^2} \rho_j \left[2v_j \eta_j - \frac{1}{v_j \eta_j} \right] \tag{A.17}$$

$$\frac{\partial R_{ij}}{\partial v_i} = \frac{\partial T_{ij}}{\partial v_i} \tag{A.18}$$

$$\frac{\partial R_{ij}}{\partial v_j} = \frac{\partial T_{ij}}{\partial v_j} \tag{A.19}$$

The quantity $\tau(p)$ is given by

$$\tau(p) = \sum_{Ray\ Path} \eta_j Th_j \tag{A.20}$$

where Th_j is the layer thickness. By straightforward differentiation, we have

$$\frac{\partial \tau(p)}{\partial v_j} = \frac{-2Th_j}{v_j^3 \eta_j} \tag{A.21}$$

assuming the ray propagates through the j^{th} layer twice (i.e. down and up).